POLITECNICO DI TORINO
Master's Degree in Mechanical Engineering

Evaluation of Loss Models Predictions in One-Dimensional Analysis of Centrifugal Compressors

Supervisors:
Prof. Mirko Baratta
Prof. Simone Salvadori
Prof. Daniela Anna Misul
PhD Nicola Talia

Candidate:
Alessio Rakipi
Matricola: 320019

ACADEMIC YEAR 2024/2025

Ringraziamenti

Arrivato alla fine di questo percorso — reso ancora più lungo dalla mia irrefrenabile volontà di ridare gli esami più e più volte — ci tengo a ringraziare in primis i professori Mirko Baratta, Simone Salvadori e Daniela Anna Misul per la possibilità che mi è stata data di lavorare a questa tesi e per la disponibilità mostrata, non solo durante questo periodo di collaborazione, ma anche lungo tutto il percorso di studi.

Un grosso ringraziamento lo devo a Nicola, che in questi mesi mi ha seguito, supportato (e sopportato) e aiutato più come un amico che come un dottorando: è stato davvero un piacere lavorare con te.

Ringrazio di cuore mio papà, mia mamma e soprattutto mia sorella per il sostegno e per la pazienza dimostrata di fronte ai miei eterni rifiuti ai voti.

Infine, ma non per ultimi, ringrazio i miei amici di sempre — in particolare la buon'anima di Pollo, che più di tutti mi ha sOpportato — e le nuove amicizie che questo percorso mi ha regalato.

Ultimo, non grazie a me stesso.

Abstract

Compressed Air Energy Storage (CAES) systems are emerging as a promising large scale energy storage technology, where the efficiency of the compression process has a direct impact on the overall cycle performance. Centrifugal compressors represent a critical component, and the availability of reliable prediction tools is essential to support their design, optimization, and integration into such systems. While three dimensional CFD simulations can provide highly accurate results, they are computationally intensive and not always suitable for preliminary design phases, where faster evaluation methods are required.

This thesis focuses on the study of the performance of a one-dimensional model for centrifugal compressor performance prediction, implemented in MATLAB. The model computes key parameters such as pressure ratio and isentropic efficiency directly from the compressor geometry and boundary conditions. A central feature of the work is the implementation of multiple sets of loss correlations from the literature, each describing different mechanisms including incidence, skin friction, clearance, slip, mixing, and diffuser-related effects. A detailed discussion of these correlations is provided, emphasizing their assumptions, validity ranges, and impact on the predicted performance.

To assess the predictive capability of the model, the code was applied to centrifugal compressor geometries and datasets reported in the literature, which include experimental measurements of pressure ratio and efficiency. The comparison revealed that the model is able to reproduce performance trends, while also highlighting the discrepancies associated with different sets of correlations. In particular, certain models provided good agreement in terms of pressure ratio prediction, whereas others were more effective in estimating efficiency trends. These results underscore the importance of selecting appropriate loss models depending on the specific performance feature of interest.

Overall, the thesis provides a critical review of existing loss modeling approaches. Within the broader framework of CAES applications, the study demonstrates how one-dimensional modelling can effectively balance computational efficiency and predictive accuracy, making it suitable for preliminary design and comparative studies. The modular structure of the code also opens the way for future extensions, including the integration of new correlations and its application to alternative compressor configurations or other turbomachinery components.

Contents

List of Figures

List of Tables

List of Symbols

Symbols

Symbol	**Description**	**Unit**
$\dot{m}$	Mass flow rate	kg/s
p	Static pressure	Pa
p_0	Total pressure	Pa
T	Static temperature	K
T_0	Total temperature	K
v	Specific volume	m^3
U	Peripheral (tangential) velocity	m/s
V	Absolute velocity	m/s
W	Relative velocity	m/s
R_1, R_2	Inlet and outlet impeller radii	m
b_1, b_2	Blade height at inlet and outlet	m
n	Rotational speed	rpm
ω	Angular velocity	rad/s
h, h_0, h_{0s}	Static, total and isentropic enthalpy	J/kg
S	Entropy	J/K
η_{is}	Isentropic efficiency	–
η_{RT}	Round-trip efficiency	–
π	Pressure ratio (p_{02}/p_{01})	–
ϕ	Flow coefficient	–
ψ	Head coefficient	–
σ	Slip factor	–
τ	Torque	N·m
Q	Heat	J/kg
L_i	Work	J
L_w	Mechanical work losses	J
P	Power	W
$E_{el,in}$	Electrical energy input	J
E_{fuel}	Fuel combustion energy	J
E_k	Kinetic energy	J
E_g	Gravitational energy	J

Continued on next page...

Symbol	**Description**	**Unit**
E_w	Centrifugal force field potential energy	J
λ	Work coefficient	–
M	Mach number	–
Re	Reynolds number	–
R_g	Gas constant	J/kgK
c_p	Specific heat at constant pressure	J/kgK
μ	Dynamic viscosity	Pa·s
ν	Kinematic viscosity	m^2/s
δ	Clearance height	m
N_s	Specific speed	–
N_D	Specific diameter	–
ζ	Loss coefficient	–
DR	Diffusion ratio	–
C_P	Pressure recovery coefficient	–
A	Flow area	m^2
Z	Number of blades	–
L	Length	m
L_b	Impeller flow length	m
L_m	Impeller meridional length	m
e	Roughness	μm

Greek Letters

Symbol	**Description**	**Unit**
α	Absolute flow angle	°
α_c	Streamline angle	°
β	Relative (blade) angle	°
γ	Specific heat ratio	–
θ	Angular coordinate	° or rad
η	Efficiency	–
ϵ	Clearance gap	m
ω	Angular velocity	rad/s
ρ	Density	$\mathrm{kg/m}^3$
τ	Torque	N·m
ϕ	Flow coefficient	–
ψ	Head coefficient	–
σ	Slip factor	–

Subscripts and Superscripts

Notation	**Meaning**
1, 2	Inlet and outlet of impeller or stage
h	Hub parameter
s	Shroud parameter
m	Meridional parameter
u	Tangential parameter
in, out	Inlet and outlet conditions
is	Isentropic condition
tt	Total-to-total condition
ts	Total-to-static condition
el	Electric variable
th	Throat parameter
cl	Clearance parameter
bl	Blade loading parameter
max, min	Maximum and minimum value
poly	polytropic
is	isoentropic
ref	Reference condition
opt	Optimal or design point
exp	Experimental data
calc	Calculated value
igv	Inlet guide vanes parameter
inc	Incidence parameter
mean	Mean parameter
h	Hub
shr	Shroud
hyd	Hydraulic parameter
mix	Mixing
sf	Skin friction
ch	choke
s	shock
re	recirculation
df	disk friction
leak	leakage

Introduction

The global energy demand is continuously increasing, driven by industrial development and population growth. According to the International Energy Agency (IEA), in 2024 global demand rose by approximately 2.2%, a rate significantly higher than the average growth of the past decade, which was around 1.3%. Although fossil fuels still represent the dominant energy source, renewable technologies are rapidly gaining ground.

In terms of electricity production, recent data show that renewable sources have reached nearly 30% of global electricity generation, marking a substantial milestone in the ongoing energy transition.

This evolution is critical for several reasons:

- the growing electrification of industrial processes and transport increases the need for flexibility within the power system;
- renewable energy sources, such as wind and solar, are inherently intermittent and variable over time;
- to ensure grid stability and system efficiency, energy "buffering" or storage solutions are required when the power supply exceeds demand.

For these reasons, the development of energy storage technologies is essential to sustain the continuous expansion of renewable energy. Without efficient storage, the large-scale integration of renewables could be significantly limited. Various storage solutions are available today — including electrochemical batteries, pumped hydro, thermal storage, and *Compressed Air Energy Storage* (CAES) systems — each offering specific advantages depending on the required scale, duration, and operational flexibility.

To better frame the role of CAES within the broader landscape of energy storage technologies, a brief overview of the main storage principles is necessary. Energy storage solutions can be categorised according to the form in which energy is accumulated: electrochemical systems (such as lithium-ion and flow batteries) store energy through reversible chemical reactions; mechanical systems, including pumped hydro and flywheels, rely on gravitational or rotational potential; thermal storage technologies retain energy as sensible or latent heat; and thermomechanical systems, such as CAES, store energy by compressing and later expanding a working fluid. Each technology offers different advantages in terms of storage duration, response time, scalability, and cost. In particular, mechanical and thermomechanical storage solutions are considered highly suitable for medium-and large-scale applications due to their robustness, long lifetime, and comparatively low degradation. Within this framework, CAES emerges as a promising option for large-scale, medium–long duration storage, bridging the gap between short-term battery-based solutions and long-term bulk storage.

CAES represents one of the most promising large-scale energy storage technologies. Its working principle is based on compressing ambient air using surplus electrical energy during periods of low demand, storing it in high-pressure vessels or underground caverns, and then expanding it through turbines to generate electricity during peak demand periods. This configuration allows the decoupling of electricity generation and consumption, contributing to the stability and flexibility of the electrical grid. Recent advancements, such as adiabatic and isothermal CAES concepts, aim to improve round-trip efficiency by recovering or managing the thermal energy produced during compression. Consequently, CAES systems are gaining increasing attention as viable, large-scale, and environmentally sustainable alternatives to electrochemical storage, particularly for medium- and long-duration energy storage applications.

A critical component of CAES systems is the compressor train, responsible for converting electrical energy into potential energy stored as compressed air. Among the various compressor typologies, *centrifugal compressors* are particularly attractive due to their compactness, reliability, and capability to operate over a wide range of flow conditions. Their aerodynamic design, however, involves complex flow phenomena that strongly affect the overall performance — including incidence effects, boundary-layer development, tip-clearance losses, and mixing in the diffuser.

Accurate performance prediction of these machines requires robust physical modeling and the implementation of reliable loss correlations. While three-dimensional CFD simulations can provide detailed insights into the flow behavior, they are computationally expensive and not ideal for system-level design or parametric studies. In this context, *one-dimensional (1D) performance models* offer a valuable compromise between accuracy and computational efficiency, allowing the prediction of global quantities such as pressure ratio, efficiency, and mass flow rate with reduced computational cost.

The present thesis focuses on the development and validation of a one-dimensional performance model for centrifugal compressors, intended for use in CAES applications. The model, implemented in MATLAB, integrates multiple aerodynamic loss correlations — covering incidence, skin friction, tip leakage, mixing, and diffuser losses — to capture the main physical mechanisms that determine compressor performance. The predictive capability of the model is evaluated through a detailed comparison with experimental data from several reference cases available in the literature, including well-documented NASA and Eckardt compressors, as well as eight additional rotors presented by Zhang et al. (2019).

Ultimately, the goal of this work is to provide a flexible, physically consistent, and computationally efficient tool capable of predicting the performance of centrifugal compressors across a wide operating range. Such a model can serve both as a standalone design and analysis tool and as a foundation for future system-level simulations and optimization studies within the framework of energy storage technologies.

Chapter 1

CAES - Compressed Air Energy Storage

CAES — Compressed Air Energy Storage — is a well-established mechanical energy storage technology suitable for large-scale commercial applications, alongside PHES (Pumped Hydroelectric Energy Storage).

The concept was first proposed in the 1940s, but practical implementations did not appear until the 1960s. During that period, the energy sector faced several challenges: increasing power demand during peak hours placed considerable stress on existing power plants, which were often unable to supply the required energy. Another important issue was the significant amount of off-peak energy that was routinely wasted [1].

CAES technology emerged as a promising solution to mitigate these fluctuations. Beginning in the 1970s, CAES attracted growing interest thanks to its large storage capacity, environmentally friendly operation (particularly when no fossil fuels are used for reheating), long lifetime, low self-discharge, and relatively low cost per unit of stored energy [2]. CAES systems can also be easily integrated with intermittent renewable energy sources, such as wind and solar, contributing to smoothing power output [1].
Despite its advantages, CAES also presents several drawbacks: high upfront capital investment, the need to reheat the air before expansion, lower round-trip efficiency (RTE) compared to other storage technologies, siting and permitting challenges, difficulties in identifying and preparing suitable geological caverns, limited depth of discharge, and longer response times [2]. Furthermore, the requirement to raise the temperature of the stored air prior to expansion highlights another major limitation: the frequent reliance on fossil fuels during the discharge phase [1].

1.1 Working principle

A CAES system stores electrical energy in the form of pressurised air, which can later be expanded to generate electricity on demand. It is based on the same thermodynamic principles as a conventional gas turbine, with the key distinction that CAES decouples the compression and expansion processes. Energy is stored as elastic potential energy in a dedicated storage vessel, as illustrated in Figure 1.1.

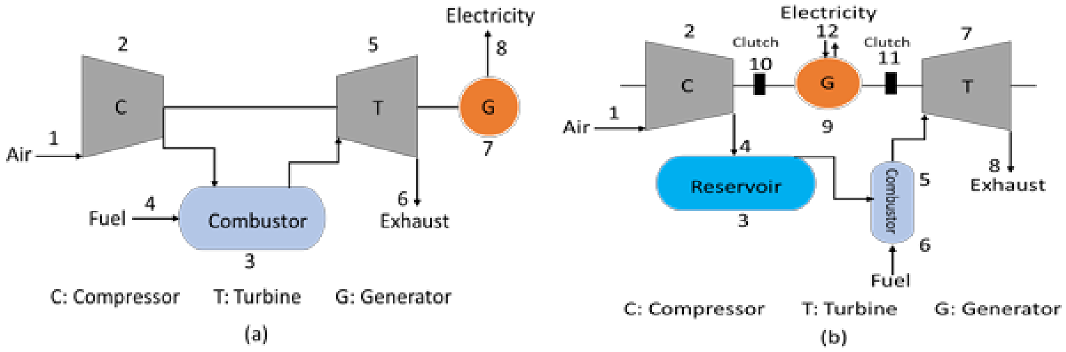

Figure 1.1: Structure of: (**a**) a conventional gas turbine system; (**b**) a gas turbine system adapted for energy storage [1].

The CAES process consists of three fundamental stages:

- **Charging phase**;
- **Storage phase**;
- **Discharge phase**.

The compression and expansion of air are commonly approximated as *polytropic* processes:

$$pv^n = \text{const}, \qquad L_{\text{i,poly}} = \frac{n}{n-1} R T_1 \left[\left(\frac{p_2}{p_1} \right)^{\frac{n-1}{n}} - 1 \right], \tag{1.1}$$

where n is the polytropic index ($n = 1$ for isothermal processes, $n = \gamma$ for isentropic processes). The ideal isentropic efficiency of each stage is defined as:

$$\eta_s = \frac{L_{\text{isentropic}}}{L_{\text{actual}}}. \tag{1.2}$$

Losses due to friction, heat transfer, and flow non-uniformities typically result in η_s values between 0.8 and 0.9 for modern turbocompressors.

1.1.1 Charging phase

During off-peak periods, or when renewable generation exceeds demand, the charging phase takes place. The surplus energy powers a multi-stage compressor unit that compresses ambient air. The discharge temperature at the outlet of the compressor can be very high; therefore, intercoolers are installed between stages to reduce the temperature and limit the work input. The compressed air is then stored in a dedicated volume — usually an underground cavern, a lined rock cavern, or a bank of above-ground tanks — where it remains at high pressure until energy is required.

The compression process is energy-intensive and releases a significant amount of heat:

$$Q_{\text{comp}} = \int \dot{m}\, c_p \left(T_{\text{out}} - T_{\text{in}}\right)\, dt. \tag{1.3}$$

In conventional CAES plants, this heat is rejected to the environment through intercoolers and aftercoolers. In more advanced concepts, it is captured and stored for later use.

1.1.2 Storage phase

The compressed air is stored in a sealed volume between a minimum and maximum allowable pressure. The difference between these two pressure levels defines the usable energy capacity.

For an isothermal storage process, the theoretical stored energy is given by:

$$E_{\text{cav}} = \int_{p_{\min}}^{p_{\max}} V\, dp = V\left(p_{\max} - p_{\min}\right), \tag{1.4}$$

while for a general polytropic evolution:

$$E_{\text{cav}} = \frac{p_{\max} V}{n-1}\left[1 - \left(\frac{p_{\min}}{p_{\max}}\right)^{\frac{n-1}{n}}\right], \tag{1.5}$$

where n is the polytropic index ($1 < n < \gamma$).

1.1.3 Discharging phase

When electricity is required — either during peak demand or when renewable production is insufficient — the stored air is released and expanded through one or more turbine stages coupled to an electrical generator. Depending on the plant configuration, the air may be preheated before expansion using:

- external fuel combustion (DIABATIC SYSTEMS);
- stored heat recovered from the compression phase (ADIABATIC SYSTEMS);
- heat exchangers or liquid heat carriers (ISOTHERMAL SYSTEMS).

The expansion process generates mechanical work, which is converted back into electricity:

$$L_{\exp} = \int \dot{m}\, \left(h_{\text{out}} - h_{\text{in}}\right)\, dt. \tag{1.6}$$

The *round-trip efficiency* is defined as:

$$\eta_{\text{RT}} = \frac{E_{\text{el,out}}}{E_{\text{el,in}} + E_{\text{fuel}}}, \tag{1.7}$$

typically ranging from 40–55% for diabatic CAES and reaching up to 70% or higher for advanced adiabatic configurations.

1.2 CAES components

A CAES plant stores and dispatches energy by combining mechanical equipment with suitable geological formations. The overall system relies on six key components:

- **Motor/Generator**: equipped with clutches that allow alternating engagement with the compressor or the turbine, depending on the operating mode (charging or discharging);
- **Compressor**: stores energy by compressing ambient air. It typically consists of two or more stages with intercoolers and aftercoolers to improve compression efficiency;
- **Turbine**: converts the stored energy back into electrical power when demand exceeds supply. Turbine trains usually include both high-pressure (HP) and low-pressure (LP) expansion stages;
- **Controllers**: manage the combustion turbine (in diabatic plants), the compressor train, the auxiliary systems, and the transition between charging and discharging modes;
- **Auxiliary equipment**: includes fuel storage (if applicable), cooling systems, piping networks, and heat exchangers;
- **Underground storage**: the geological cavity (typically a salt cavern) that houses the compressed air.

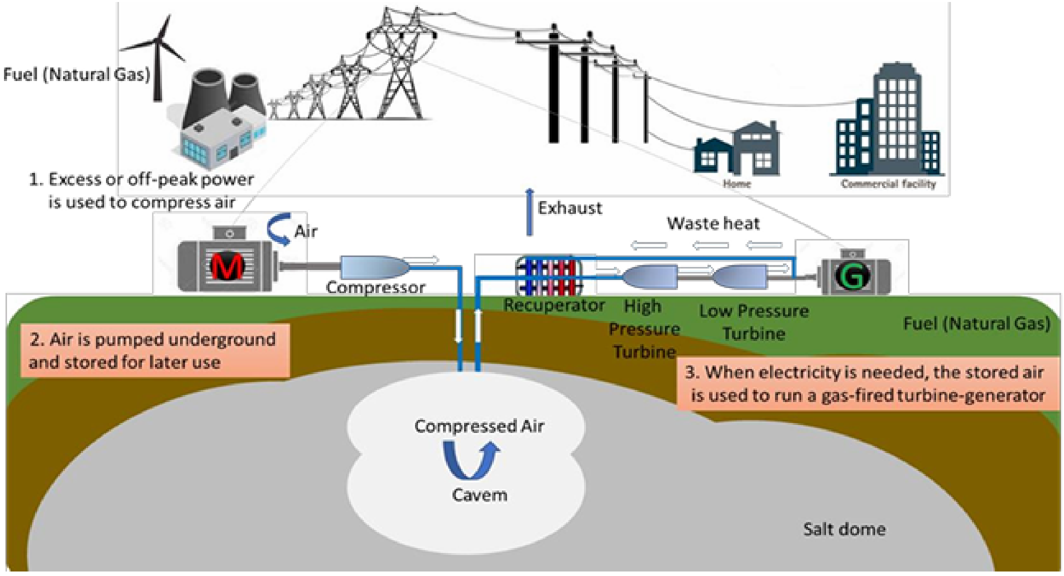

Figure 1.2: Main components of a CAES system [1].

CAES installations generally require specific geographic conditions, as compressed air is traditionally stored in natural or artificially created caverns.

Modern developments aim to overcome this limitation by using man-made above-ground or underground tanks, while more recent studies explore offshore and underwater storage configurations [1].

1.3 Storage media and system configuration

The most common storage method is the use of underground **salt caverns**, which provide large volumes, excellent sealing characteristics, and a self-healing rock structure. Alternative options include **lined rock caverns**, **porous geological formations**, and **above-ground pressure vessels**.

Key design parameters for storage include the total volume, allowable pressure range, and temperature regulation strategy (isothermal vs. adiabatic behaviour).

Air storage vessels can be classified as:

- **Constant-volume storage**: the chamber has fixed boundaries and accommodates different pressures depending on the charge state. Because CAES turbines cannot operate below a minimum inlet pressure, the usable pressure range must be limited. Examples include salt caverns formed through solution mining and abandoned mining cavities.
- **Constant-pressure storage**: the gas is kept at an approximately constant pressure within a variable-volume vessel. This requires a liquid displacement system to maintain isobaric conditions. A notable variant exploits the hydrostatic head of water to maintain pressure.

Constant-pressure storage generally offers superior performance compared to constant-volume systems. Advantages include:

- higher usable energy density, since the turbine inlet pressure remains constant;
- no throttling losses before expansion;
- reduced mixing losses associated with temperature variation;
- improved turbo-machinery performance thanks to stable operating conditions;
- wider siting flexibility.

However, constant-pressure systems are significantly more expensive to construct due to the complexity and cost of the variable-volume containment structure.

1.4 CAES classification

A central challenge in CAES systems concerns the management of the heat produced during compression and the energy required to raise the air temperature prior to expansion. Improving round-trip efficiency relies heavily on recovering this waste heat.

Research in recent decades has led to several CAES concepts, classified according to how compression heat is handled. As introduced in the discharge phase, three major categories can be identified:

- **Diabatic CAES**;
- **Adiabatic CAES**;
- **Isothermal CAES**.

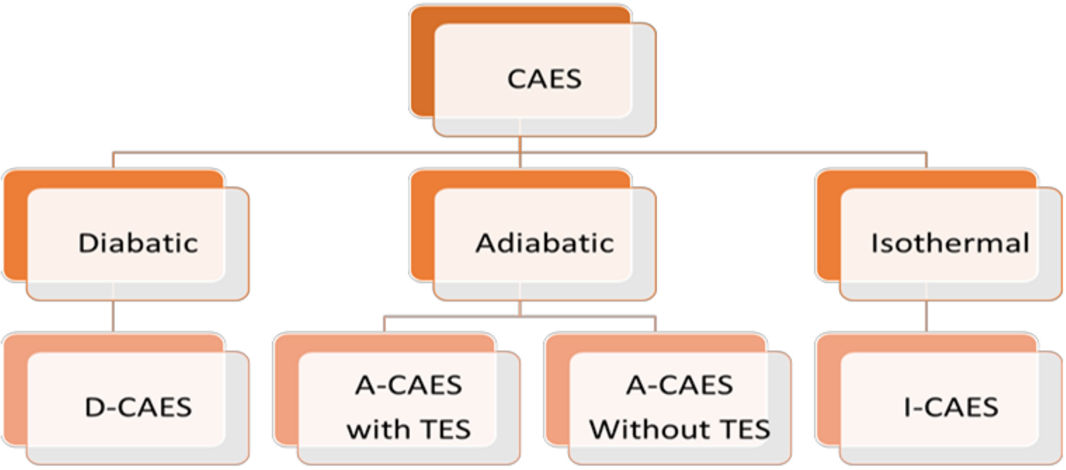

Figure 1.3: Classification of CAES systems [1].

1.4.1 Diabatic CAES Systems (D-CAES)

Diabatic CAES systems dissipate the heat of compression to the environment. They represent the earliest generation of CAES technologies, developed during the second half of the twentieth century. Because the stored air cools down significantly, an external heat source is required prior to expansion to avoid excessively low turbine inlet temperatures and the associated risk of icing. This external heat is typically provided by fossil fuel combustion. Typical round-trip efficiencies range from 40% to 55%, depending on the degree of recuperation. Despite their limitations, D-CAES plants have demonstrated long-term reliability and have provided grid stability services for decades.

Two large-scale D-CAES plants are currently in operation: the **Huntorf plant** in Germany and the **McIntosh plant** in the United States. Both use natural gas as the primary heat source and store high-pressure air in salt caverns.

The **Huntorf plant** (1978) is widely recognised as the first commercial CAES installation. It employs two 60 MW compressors and a 321 MW expander train, operating between 46 and 72 bar, with an efficiency of approximately 42%. Due to the absence of a thermal storage system, about 25% of the compression energy is dissipated as waste heat.

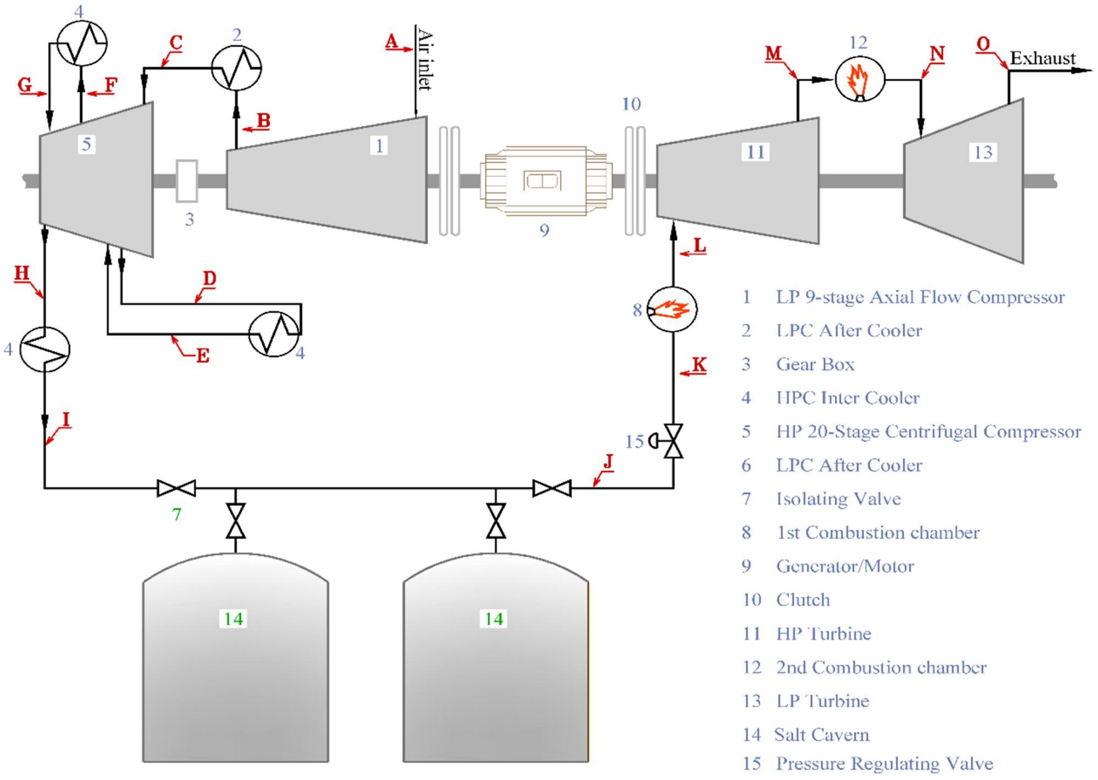

Figure 1.4: Huntorf CAES plant [3].

The second major facility, the **McIntosh plant** (1991) in Alabama (USA), includes three compressors and two expanders, operating between 46 and 75 bar. While based on the Huntorf layout, it incorporates improved components and a recuperator to preheat the combustion air, raising the overall efficiency to approximately 53% [1].

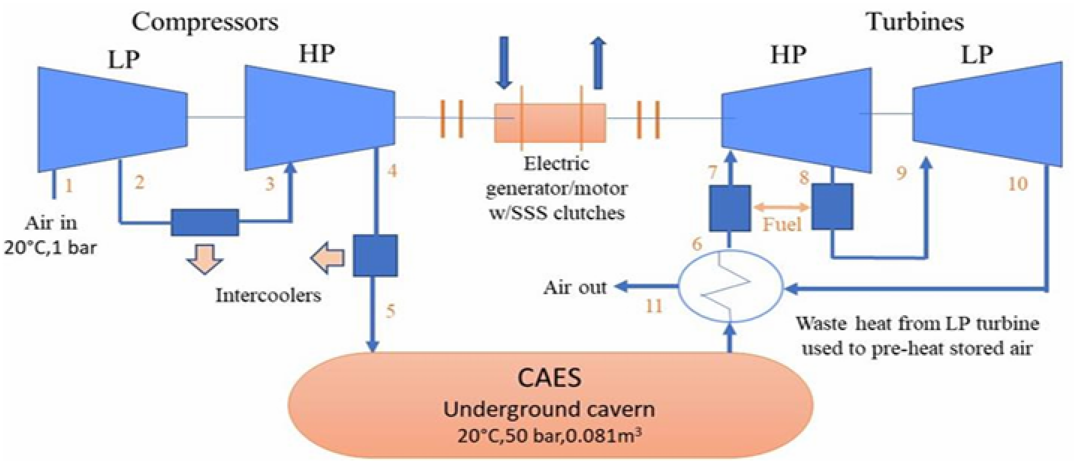

Figure 1.5: McIntosh plant: heat and energy flows [1].

1.4.2 Adiabatic CAES Systems (A-CAES)

Adiabatic CAES systems aim to overcome the limitations of D-CAES by significantly improving efficiency. As previously noted, the heat released during compression is critical for defining overall plant performance. In A-CAES designs, this heat is captured during the charging phase and reused for reheating the air during expansion, eliminating the need for fossil fuels. Depending on the thermal storage strategy adopted, A-CAES systems are classified into two categories: those *without* TES and those *with* TES.

A-CAES without TES

In A-CAES systems without dedicated thermal storage, both compressed air and heat are contained within a single storage volume. This imposes significant technical constraints: the high temperature at the compressor outlet requires storage vessels capable of withstanding elevated temperatures, and the achievable pressure ratio is limited to prevent excessive temperature rise.

Consequently, these systems generally operate at relatively low storage pressures and, therefore, low energy densities. In addition, substantial material requirements and the need to protect large surfaces from heat loss lead to high capital costs. For these reasons, A-CAES without TES is not expected to become commercially viable in the near future [4].

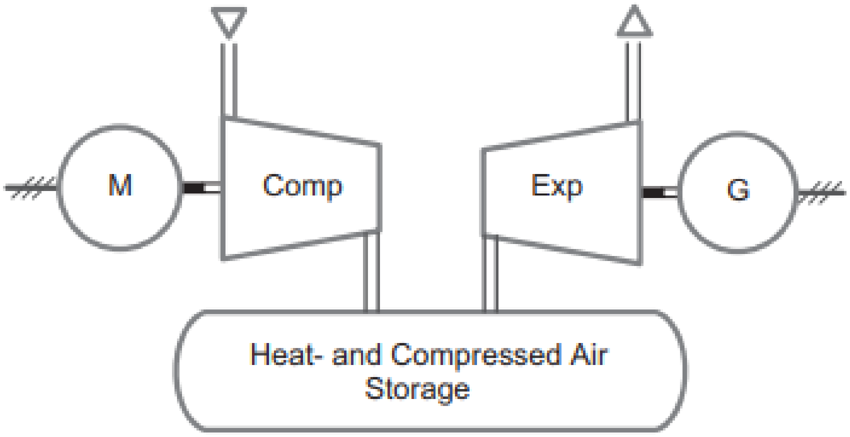

Figure 1.6: A-CAES without TES [4].

A-CAES with TES

A-CAES systems equipped with thermal energy storage collect the heat produced during compression in a dedicated TES unit. This substantially increases overall efficiency while reducing system constraints, enabling:

- faster start-up times,
- greater operational flexibility and part-load capability,

- reduced limitations on air storage conditions,
- higher storage pressures and energy densities.

Expected round-trip efficiencies range between 70% and 75%. Compared to D-CAES systems, A-CAES operation relies solely on off-peak or renewable electricity [1].

The selected storage temperature strongly influences system design and overall plant behaviour, although its effect on thermodynamic efficiency is less pronounced. Three process classes can be distinguished depending on the storage temperature:

- **High-temperature TES** (above 400°C): typically implemented using packed-bed sensible heat storage. Outlet temperatures can reach almost 600°C, enabling high turbine inlet temperatures. This concept is commonly referred to as **AA-CAES** (Advanced Adiabatic CAES).
- **Medium-temperature TES** (200–400°C): molten salts, thermal oils, or phase-change materials (PCM-filled packed beds) are used. These technologies benefit from synergies with established thermal storage applications.
- **Low-temperature TES** (below 200°C): based on liquid heat-transfer media, enabling the use of standard heat exchangers and reducing start-up time to a few minutes.

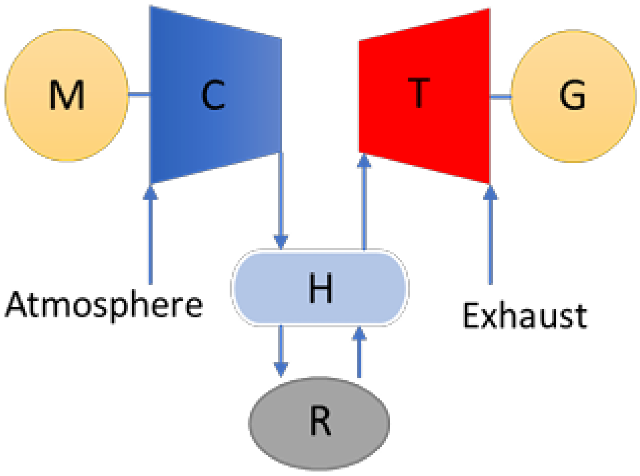

Figure 1.7: A-CAES with TES [1].

Several A-CAES plants are currently under development and approaching commercial deployment. In Germany, RWE Power is developing the “ADELE” project, targeting a capacity of 200 MW with an estimated round-trip efficiency of approximately 70% and 1 GWh of storage. In China, the Institute of Engineering Thermophysics of the Chinese Academy of Sciences has constructed a 1.5

MW A-CAES pilot plant and is developing a 10 MW demonstration facility [1].

Although promising, A-CAES technology is still in an early stage of development, and continued research and investment will be essential to reach widespread commercial deployment.

1.4.3 Isothermal CAES Systems (I-CAES)

To further improve round-trip efficiency and reduce plant costs, modern concepts propose the use of isothermal or near-isothermal compression and expansion. Achieving such conditions requires continuous heat removal (during compression) or heat addition (during expansion), typically through advanced heat-exchanger configurations.

Because heat transfer requires time, isothermal CAES concepts generally rely on piston-based machinery, which offers slower compression and expansion rates and larger heat-exchange surfaces [4]. Liquid-piston compressors — resembling reciprocating machines — have been developed as promising candidates for achieving near-isothermal behaviour. The injection of fine water droplets into the airflow has also proven effective in enhancing heat transfer.

Isothermal compression minimises work input from a thermodynamic standpoint, but its practical implementation requires efficient large-area heat transfer under dynamic conditions. As a result, I-CAES systems are typically modular, making them suitable for small- to medium-scale installations, with achievable efficiencies comparable to adiabatic systems at lower pressure ratios.

A Pumped Hydro Compressed Air Energy Storage (PH-CAES) configuration was proposed by Chen et al., achieving a near-isothermal compression and expansion with polytropic exponents of 1.07 and 1.03, respectively. The measured round-trip efficiency was 51%, with potential for improvement using higher-efficiency hydro turbines [5].

Droplet-based I-CAES

In droplet-based systems, heat transfer surface area is greatly increased by spraying fine liquid droplets into the airflow during compression. The droplets are later separated, stored, and reinjected during expansion [1]. A schematic representation is shown in Figure 1.8.

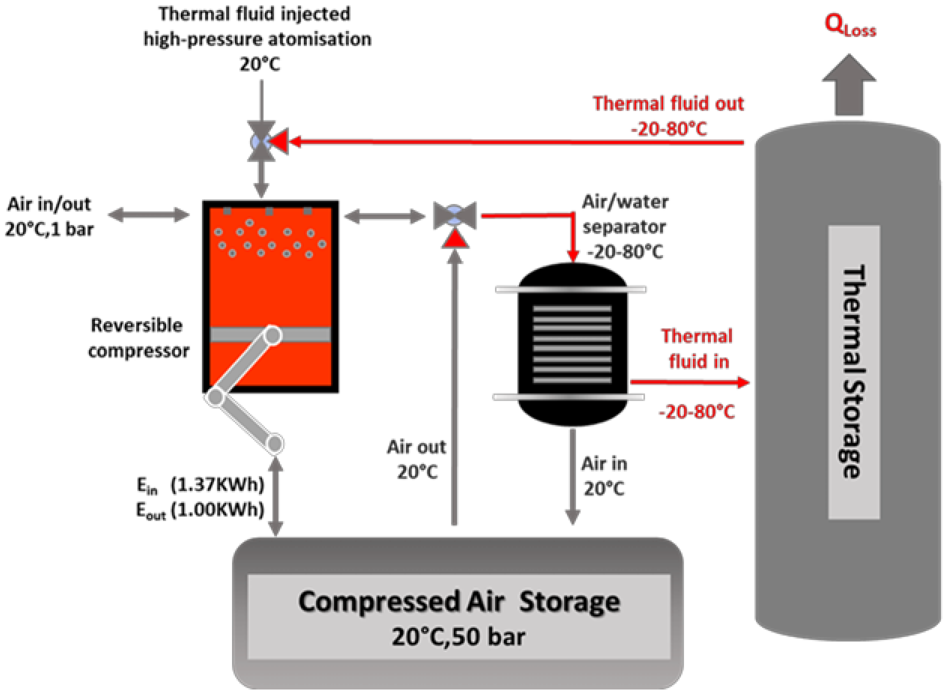

Figure 1.8: Droplet-based I-CAES [1].

Liquid Piston CAES (LP-CAES)

In liquid-piston CAES systems, a vertical water column is used to compress the air. Because heat is continuously exchanged between the liquid and the gas, both compression and expansion are nearly isothermal. The liquid piston offers several advantages:

- reduced leakage;
- improved heat transfer due to water–air contact;
- stable and quasi-isothermal compression behaviour.

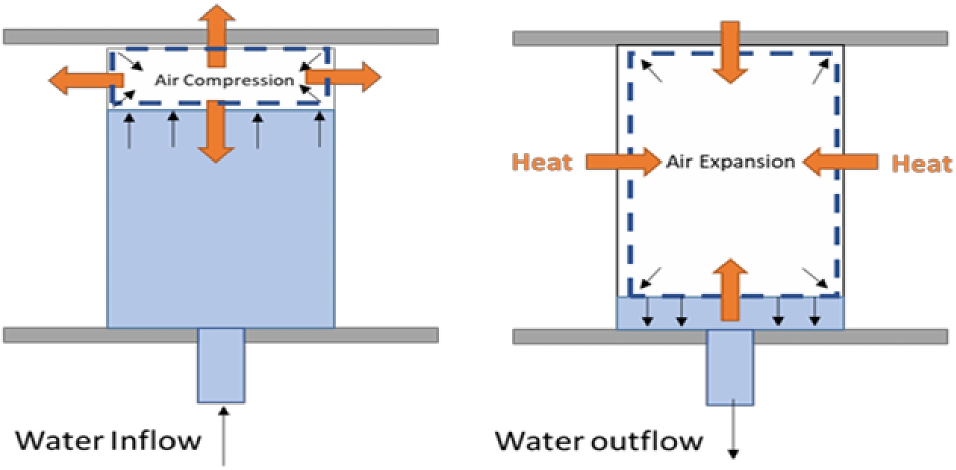

Figure 1.9: Liquid piston compressor/expander [1].

1.4.4 Ocean CAES Systems (O-CAES)

Ocean-based CAES systems exploit hydrostatic pressure to maintain constant pressure within the storage vessel. Because the storage temperature remains relatively constant and the system operates isobarically, O-CAES requires less compression work and generates more expansion work, improving overall plant efficiency.

In this configuration, the compressor is located onshore, while the storage vessel is placed underwater. O-CAES offers several advantages:

- naturally constant pressure behaviour,
- higher exergy efficiency,
- reduced throttling and mixing losses.

As with land-based systems, ocean CAES may be diabatic, adiabatic, or isothermal. Efficiency values range from approximately 55% (diabatic) to 70% (isothermal). Lower pressure ratios further improve efficiency [1].

1.4.5 Hybrid CAES

Hybrid CAES concepts combine elements of diabatic, adiabatic, and isothermal operation. Part of the compression heat may be stored in a TES, while additional heat can be supplied externally to compensate for losses during expansion. Alternatively, hybrid systems may integrate CAES with waste-heat recovery units, solar thermal systems, or geothermal heat sources, improving flexibility and site adaptability.

Although hybrid configurations increase design complexity, they enable a wider range of operational strategies and often yield improved overall performance.

1.5 Performance and efficiency considerations

The overall efficiency of a CAES system depends on:

1. the thermodynamic efficiency of compressors and turbines;
2. TES effectiveness and heat exchanger performance;
3. mechanical and electrical conversion efficiencies;
4. piping, throttling, and storage-related losses.

Typical values include:

- $\eta_{\mathrm{RT}} \approx 0.45$ for diabatic systems;
- $\eta_{\mathrm{RT}} \approx 0.70$ for adiabatic systems;
- theoretical values exceeding 0.80 for isothermal designs.

1.6 Role of the compressor

The compressor is the cornerstone of the charging phase and one of the most critical components of the entire CAES cycle. Its performance determines:

- the **electrical energy input** required per unit of stored energy;
- the **thermal energy available** for recovery in adiabatic configurations;
- the **operational flexibility** during part-load and transient operation.

High efficiency, a wide operating range, and robust mechanical characteristics are essential to ensure stable operation and high round-trip efficiency. Accurate compressor modelling — including aerodynamic losses, leakage, mixing, and tip-clearance effects — is therefore critical for reliable CAES performance prediction and system optimisation.

The next chapters focus on the thermodynamic modelling and loss analysis of the compressor, forming the technical core of this thesis.

Chapter 2

Centrifugal Compressors

Compressors are operating machines designed to increase the pressure of a gas by reducing its volume and supplying energy to the fluid. They are essential components in a wide range of industrial applications such as gas turbines, refrigeration systems, chemical plants, and energy storage technologies like CAES (Compressed Air Energy Storage). The fundamental role of a compressor is to raise the total pressure of the working fluid from an initial state (p_1, T_1) to a higher one (p_2, T_2), enabling the gas to be used for further energy conversion or storage purposes.

A brief discussion is proposed to highlight the main components of the centrifugal compressor and the basic laws allowing to described the physics governing the device.

2.1 Centrifugal Compressor Stage

In the following figures, the typical configuration of a single stage compressor is shown: the stage is composed by a rotating impeller, aiming to energize the fluid, and diffuser, to recover some of the fluid kinetic energy before leaving the compressor through the volute, which collect the flow from the stator to the discharge pipe. If the fluid exiting from the diffuser should feed a following stage, a crossover system and a return channel is developed (not our case study). Above the impeller, an inlet guide vane vane (IGV) can be introduced to properly guide the fluid at the inlet of the impeller.
The diffuser can be of two types: 'vaneless', when it's a simple annular passage, or 'vaned', when stationary vanes are integrated to the system and assist the diffusion process [6].

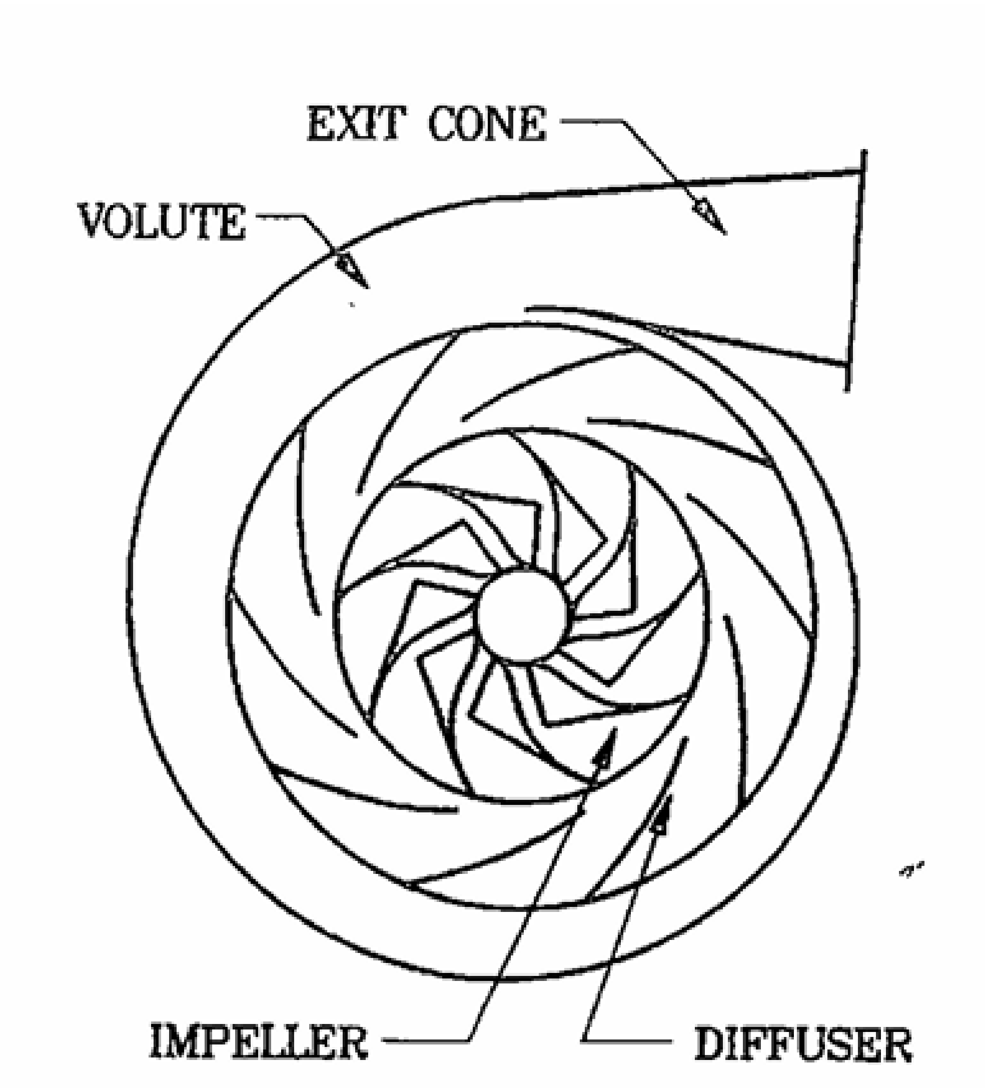

Figure 2.1: Front view of a centrifugal compressor [6]

A brief description of the main components is provided.

2.1.1 Inlet Guide Vane

Variable Inlet Guide Vanes (VIGV) are an adjustable row of stator blades installed upstream of the compressor inlet. Their main purpose is to regulate the incidence angle of the incoming flow and to introduce a controlled amount of swirl, allowing the compressor to operate efficiently over a wide range of conditions.
VIGVs are used to:

- control the incoming mass flow rate;
- adjust the incidence angle on the impeller blades, reducing off–design losses;
- delay surge and widen the operating range of the compressor;

- regulate the power absorbed by the machine, improving part–load efficiency.

By rotating the guide vanes, the tangential component of the inlet velocity is modified, directly affecting the inlet velocity triangle and the specific work input to the compressor.

A VIGV system typically consists of a circumferential row of short and robust stator blade connected to an external ring mechanism that allows to rotate all the the vanes simultaneously. The vanes have an aerodynamic profile similar to a stator blade, generally with a rounded leading edge to accommodate large incidence variations, a tapered trailing edge, a relatively short chord length for mechanical stiffness and an allowable turning angle typically between ±30° and 60°.

When the vanes rotate:

- positive vane angles introduce a swirl component in the direction of wheel rotation, increasing the specific work and the achievable pressure ratio;
- negative angles reduce swirl, lowering the work input and shifting the compressor characteristic to avoid surge;
- in the design condition, the VIGVs are often in a nearly neutral position.

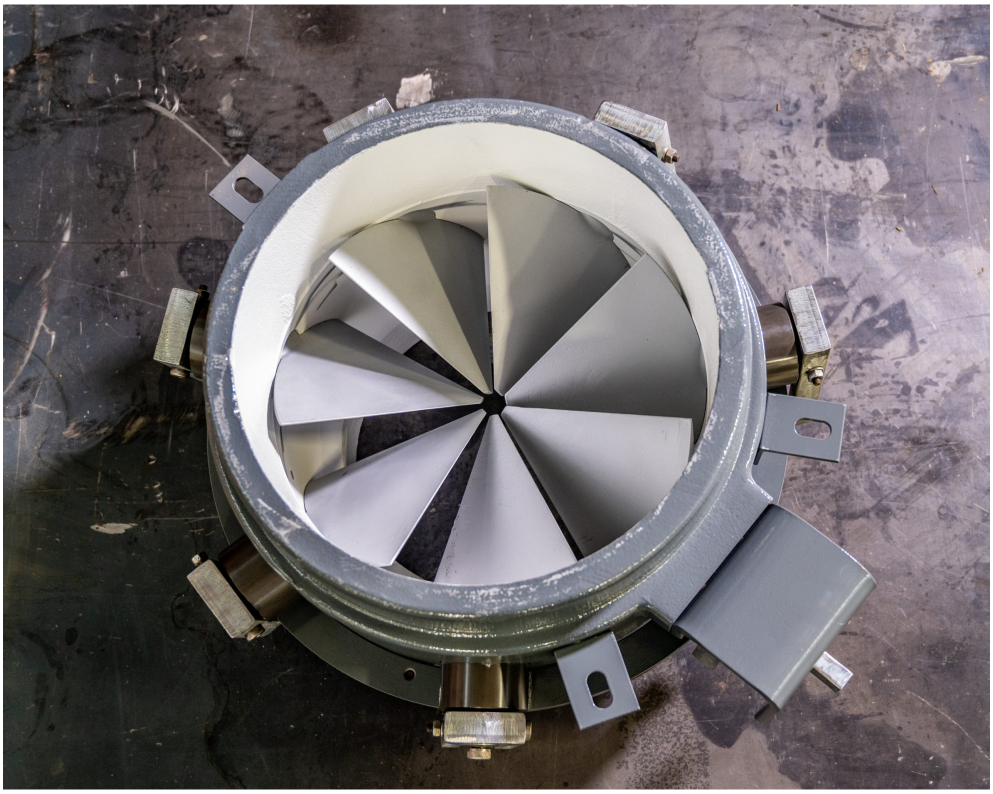

Figure 2.2: Example of IGV component [7]

2.1.2 Impeller

The impeller is the rotating component of the compressor aimed in accelerating and compressing the fluid, which enters the impeller axially and leaves radially. It consists in a series of blades mounted on a central hub, design to impart kinetic energy, converted from mechanical energy, to the airflow. The blades are typically made from aluminium alloys, titanium or stainless steel to provide the proper resistance and durability against high rotational stresses.
Two groups of blades can be distinguished in full length blades, which are as long as the impeller, and the splitter blades: they are shorter and don't occupy the entire impeller. They are developed in the regions where the flow curvature becomes higher to better guide the fluid exiting from the impeller.

The impeller can have two different configurations: it can be open (or unshrouded) or shrouded. The impeller is said to be open when the outer or shroud wall of the impeller is stationary; if a cover or a shroud is attached to the blades at the outer wall that rotates with the rotor, the impeller is called shrouded.
Usually, covered impellers are used in multistage industrial compressors: an eye seal is included to reduce the flow leakage through the gap created between the cover and the casing.

Figure 2.3: Open impeller [8]

Figure 2.4: Shrouded Impeller [9]

The shape and orientation of the blades strongly influence performance and operating range. Depending on the outlet blade angle β_2, three configurations can be defined:

- *Radial blades* ($\beta_2 = 90°$);
- *Backward-curved blades* ($\beta_2 < 90°$);
- *Forward-curved blades* ($\beta_2 > 90°$).

Backward-curved blades are most common in modern designs due to their higher efficiency and stable operating characteristics.

2.1.3 Diffuser

The diffuser transforms the kinetic energy of the flow leaving the impeller into static pressure. Depending on design requirements, two main configurations exist:

- *Vaneless diffuser*: simple design, suitable for wide operating ranges but less efficient;
- *Vaned diffuser*: provides better pressure recovery but has a narrower stable range.

In case of a vaned diffuser, between the impeller and the stator there is an annular passage, corresponding to a vaneless diffuser: this is necessary to mix the flow leaving the impeller and to standardize it before entering the following channel.

Vaneless diffusers can be divided into parallel wall-types, convergent types and expansion types, according to the different ratios of the diffuser outlet width to the impeller outlet width: expansion types are rarely used due to reverse pressure gradients that can be generated, alongside secondary flows [10].

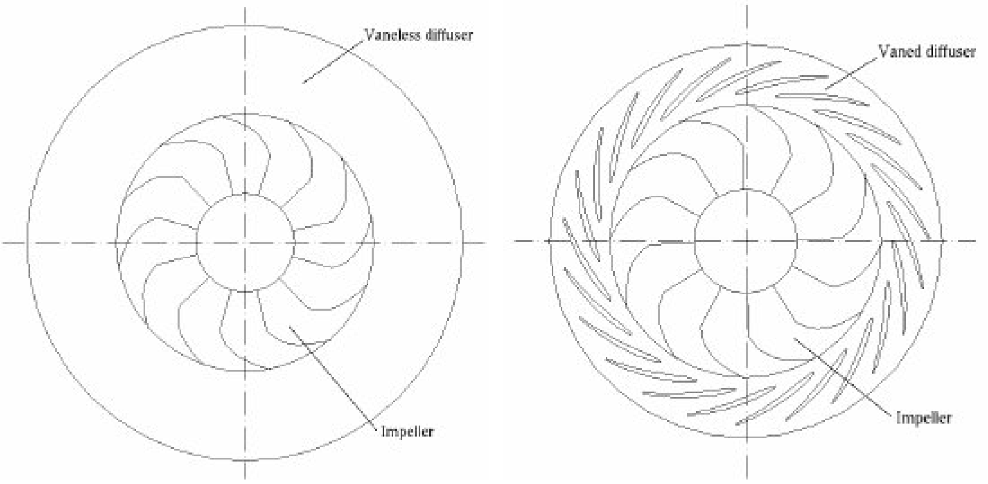

Figure 2.5: Types of diffuser [11]

Vaned diffusers are provided with blades used to remove the swirl of the fluid at a higher rate than is possible by a simple increase in radius, thereby reducing the length of flow path and diameter [12].

2.1.4 Volute

If the flow has to be brought out of the casing, either to be intercooled, merged with an external side stream or at the final compressor discharge, the diffuser is followed by a volute or scroll. The latter is a flow-collecting duct whose throughflow area increases around the circumference as more mass fractions are added. The alternative to the volute is the collector. The difference is the cross-sectional area: in the collector is constant.

Several cross-sectional shapes are available for the scroll: circular, elliptical, quadratic or rectangular. These can be symmetrical, inclined or one.sided offset with respect to the radial direction of the diffuser exit.
Depending on the type of volute selected, the flow can be accelerated, obtaining a reduction of the static pressure and a lower efficiency (internal volute), an increase in the static pressure through a lower velocity level (external volute) or neither acceleration or deceleration, working as a pure collector (central volute).

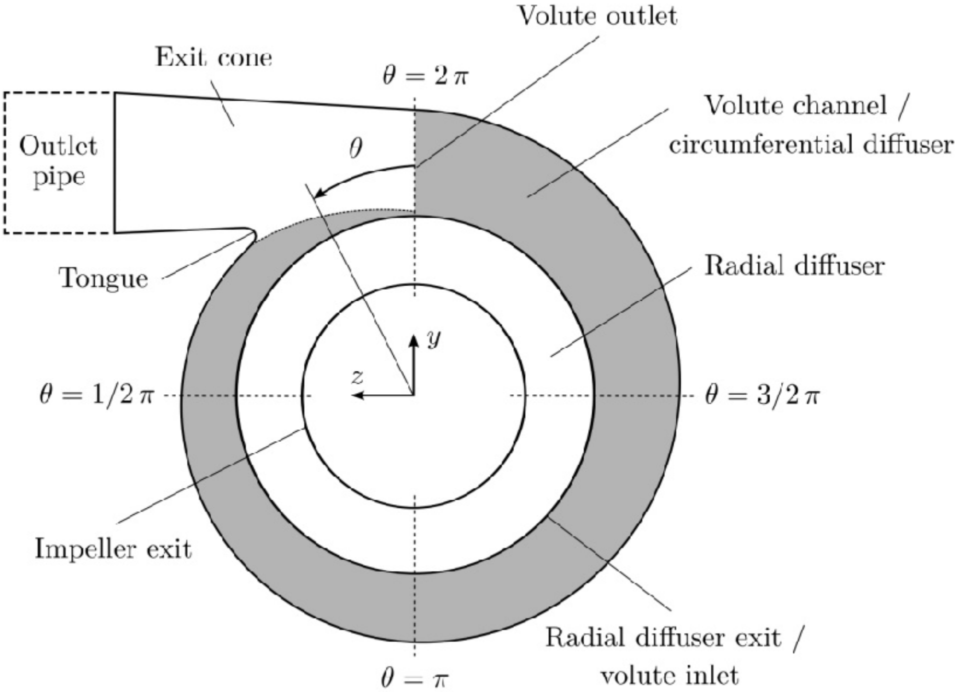

Figure 2.6: Volute geometry [13]

Although it plays a minor role in energy conversion, the volute has a strong influence on flow uniformity and machine stability, particularly near surge conditions.

2.2 Thermodynamic Principles of Compression

The working principles of gas compressors can be understood by applying some basics law of physics to define the thermodynamic properties of the fluid in different points. The thermodynamic state is determined by the knowledge of the temperature and the pressure
To this task, four main equations are used:

- *Mass continuity equation*
- *Momentum equation*
- *First law of Thermodynamic*
- *Second law of thermodynamic*

All the formulations are referred to one dimensional problem in steady state conditions (so the properties of the system remains constant over time despite the ongoing process).

2.2.1 Mass Continuity Equation

Considering a control volume V, the mass continuity equation states that the mass flow rate of the fluid entering V is conserved and is equal to the rate of fluid leaving the control volume.

$$\dot{m} = \rho V A = \text{constant} \tag{2.1}$$

where ρ represents the density of the fluid, V represents the velocity and A is the cross section normal to V. This equation will be used considering the inlet and the outlet of the different components, allowing to compute the unknown parameters:

$$\rho_1 V_{m1} A_1 = \rho_2 V_{m2} A_2 \tag{2.2}$$

2.2.2 Momentum Equation

The momentum equation expresses the relationship between the forces acting on a control volume and the rate of change of momentum of the fluid passing through it. For a steady, one-dimensional flow through a turbo-machine, it can be written as:

$$\vec{R} = \dot{m}\,(\vec{V_2} - \vec{V_1}) \tag{2.3}$$

$\vec{R}$ is the resultant force acting on the fluid [N].

Considering the specific case of centrifugal compressors, it can be applied to a control volume identified by the impeller: the external work is applied to the hub of the rotor on which the blades are placed to accelerate the fluid.
The equation can be rearranged to compute the torque of the shaft:

$$T = \dot{m}\,(R_2 V_{u2} - R_1 V_{u1}) \tag{2.4}$$

where V_u identifies the tangential component of the velocity V.

2.2.3 First Law Of Thermodynamic

The first law of thermodynamic states that energy cannot be created or destroyed, but only transformed from one to another.
For a control volume, it's defined as the balance between heat, work and energy variation of the fluid:

$$\dot{Q} + \dot{L} = \frac{dE_{\text{system}}}{dt} \tag{2.5}$$

Heat $\dot{Q}$ and work $\dot{L}$ are considered as powers [W]. The internal energy takes into account different contributions: internal energy (U), kinetic energy (E_k), gravitational potential energy (E_g) and centrifugal force field potential energy (E_w). Net work per unit time is composed by two terms: $\dot{L}_e$, the displacement work, associated with fluid pressure and $\dot{L}_i$, the shaft work, associated with the interaction between the fluid and the moving elements.

The first law of thermodynamic can be rewritten by combining the expression of the external work with the internal energy, the definition of enthalpy is obtained:

$$h = U + pv \tag{2.6}$$

If a 1-D system in steady state conditions is considered, the first law can be described as (written considering the specific quantities, so dividing by the mass flow rate $\dot{m}$):

$$Q + L_i = \Delta h + \Delta E_k + \Delta E_g + \Delta E_w \tag{2.7}$$

Q is neglected: the phenomena taking place is considered adiabatic since the time scale is too short to have thermal exchanges; a fixed frame of reference is used, allowing to neglect the contribution of the centrifugal forces. Finally, the potential energy is negligible.

The resulting equation considered for the compressor is:

$$L_i = (h_2 - h_1) + \frac{1}{2}(V_2 - V_1)^2 \tag{2.8}$$

Stagnation Quantities

The definition of the first law applied to the compressor allows to introduce the concept of stagnation or total quantities: they refers to the value that a flow property would assume if the fluid were brought to rest isentropically (without losses or heat transfer). They are related to the static quantities by means of the velocity:

$$h_0 = h + \frac{V^2}{2} \tag{2.9}$$

The total temperature can be obtained considering the relationship between temperature and enthalpy valid for an ideal (or perfect) gas:

$$h = c_p T \tag{2.10}$$

$$T_0 = T + \frac{V^2}{2c_p} \tag{2.11}$$

The shaft specific work defined by equation 2.8 can be also written as the difference in total enthalpies between inlet and outlet of the impeller:

$$L_i = \Delta h_0 = h_{02} - h_{01} = (h_2 + \frac{V_2^2}{2}) - (h_1 + \frac{V_1^2}{2}) \tag{2.12}$$

Considering that the passage from static to total quanities means assuming an isentropic phenomena, the total pressure can be computed:

$$p_0 = p(\frac{T_0}{T})^{\frac{\gamma}{\gamma-1}} \tag{2.13}$$

The ratio between total and static temperature can be defined as:

$$\frac{T_0}{T} = 1 + \frac{\gamma - 1}{2} M^2 \tag{2.14}$$

M represents the Mach number, a non dimensional parameter that measures the ratio between the flow velocity and the speed of sound a:

$$a = \sqrt{\gamma R T} \tag{2.15}$$

$$M = \frac{V}{a} \tag{2.16}$$

Alongside the stagnation quantities, also total relative parameters can be obtained: instead of using the absolute velocity V, the relative velocity is used W. In this context, rothalpy I is the quantity conserved in a rotating reference frame:

$$I = h + \frac{W^2}{2} - \frac{U^2}{2} \tag{2.17}$$

Relative temperature and relative Mach number are obtained by using equations 2.11 and 2.15 by just substituting V with W.

2.2.4 Second law of thermodynamic

The second law of thermodynamic explains that the total amount of heat cannot be converted into work: this happens due to some irreversible phenomena taking place in the system. To analyse the systems, a new parameter is introduced: the entropy. On a differential basis, the second law can be described by:

$$dS = \frac{\delta Q}{T} + \frac{\delta L_w}{T} \tag{2.18}$$

The second term, describing the entropy production caused by internal irreversibility, is null only in case of a reversible process. By performing the integration, the entropy gain (which is always positive) can be computed. Very useful in the computation of the thermodynamic properties is to consider isentropic process: it is assumed to have no entropy generation. The final pressure can be computed: both isentropic and 'real' compression line arrived to the pressure value.

2.3 Velocity Triangles

The flow through the compressor can be described using velocity triangles: they relate the absolute velocity V with the relative velocity W and the tangential speed U.

$$\vec{V} = \vec{U} + \vec{W} \tag{2.19}$$

A plane defined by the meridional and the tangential direction is consider to represent the velocities. Excluded U, which is purely tangential, V and W can be divided into the two components: V_m, V_u, W_m and W_u. Generally, the velocities' vectors are characterised by an angle, defined with respect to the tangential component: α for the absolute velocity and β for the relative velocity.

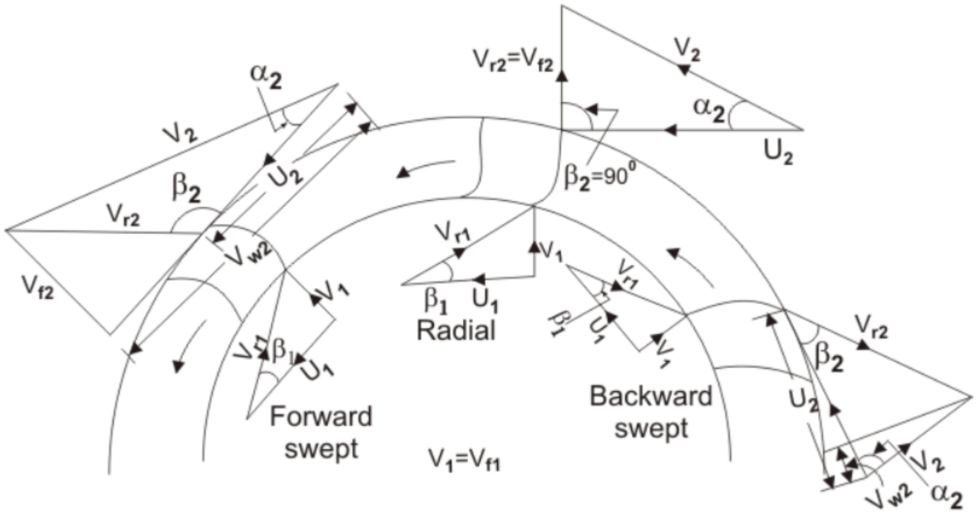

Figure 2.7: Impeller velocity triangles in case of Radial, Forward-curved and Backward-curved blades.

The inlet triangles are not affected by the type of blade used in the impeller: generally, the inlet flow is purely axial, having the absolute velocity oriented in the meridional direction. The tangential speed U_1 can be computed from the angular speed; the relative velocity W_1 (in the figure V_{r1} is automatically obtained (basing on the vectorial link highlighted in 2.19.
The outlet state depends on the shape of the blade: the relative velocity follows the outlet blade angle and is directed in the same direction. U_2 can be computed as U_1: the absolute velocity is obtained. W_2 is oriented in the radial direction.

At the inlet, the flow may have a small tangential component V_{u1} due to preswirl, while at the outlet, V_{u2} is generally positive and larger, resulting in a net increase in angular momentum.

The theoretical energy exchange in a turbomachine, corresponding to the work required by the compressor, is described by the **Euler turbomachinery equation**:

$$\Delta h_t = L_i = U_2 V_{u2} - U_1 V_{u1} \tag{2.20}$$

where Δh_t is the total enthalpy rise per unit mass, and U_i, V_{ui} are the peripheral and tangential velocity components at station i.

2.4 Stage Evolution

The evolution of the thermodynamic properties of a centrifugal compressor stage can be represented in a Mollier diagram, showing the enthalpy of the system as a function of the entropy generated. The figure 2.8 shows the compression taking place in the impeller (from 1 to 2) and in the diffuser (from 2 to 3).

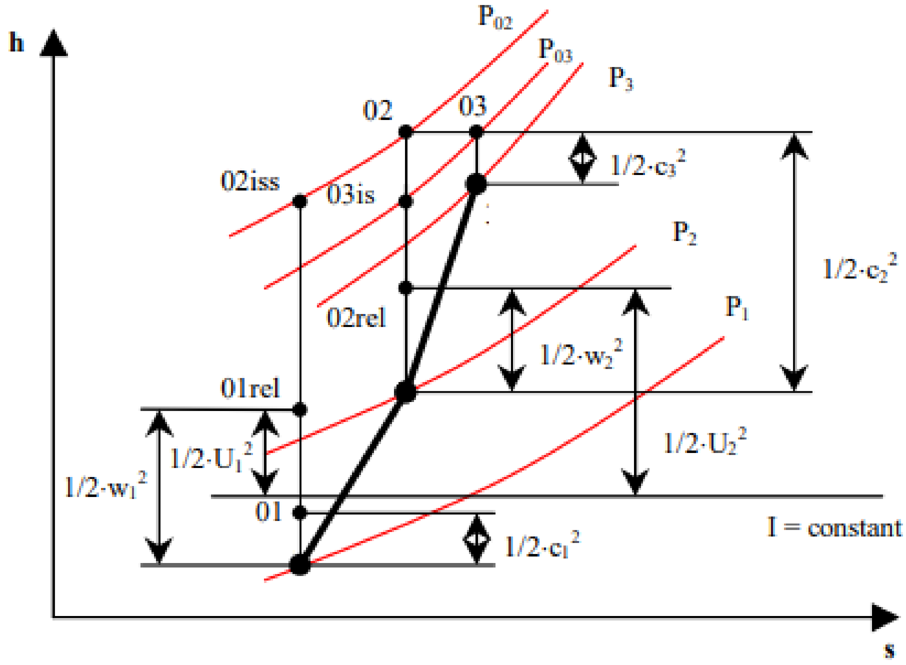

Figure 2.8: Stage evolution [14]

Fluid enters the impeller eye through an accelerating nozzle: the velocity increases alongside a pressure drop between nozzle exit and impeller inlet. For this reason, to be more precise, an expansion should be considered to reach point 1: a small amount of entropy is generated and an enthalpy reduction is observed. The starting point will be called 00. According to the first law of thermodynamic, the total enthalpy is conserved:

$$\Delta h = h_{01} - h_{00} = 0 \quad \Rightarrow \quad h_{00} = h_{01} \tag{2.21}$$

1 - 2
The process taking place in this range correspond to the compression in the impeller: 1 is the inlet, 2 is the outlet. Considerable amount of entropy is generated and the fluid is accelerated; using the first law, the work required to perform the compression can be calculated:

$$L_i = \Delta h + \Delta E_k = (h_2 - h_1) + \frac{1}{2}(V_2^2 - V_1^2) = h_{02} - h_{01} \tag{2.22}$$

2 - 3
This section refers to the diffusion process taking place in the diffuser: the large kinetic energy of the flow exiting from the impeller is transformed in static pressure, further increasing from p_2 to p_3. The stagnation enthalpy remains unchanged in this phase.

Finally, a further compression of the fluid takes place in the scroll following the diffuser: then, the fluid is delivered to the outlet.

2.4.1 Efficiency and Pressure Ratio

When a centrifugal compressor is analysed, two different efficiencies can be computed:

- *Isentropic efficiency*: it's the ratio between the isentropic work, which is the ideal work to compress the gas isentropically, and the real work required.

  $$\eta_{is} = \frac{L_{is}}{L_i} = \frac{L_i - L_w - RHE}{L_i} \tag{2.23}$$

  L_{is} is obtained from the actual work, to which is subtracted the contribution of the losses L_w and the re-heating effect (RHE, caused by viscous dissipation.

- *Polytropic efficiency*: it's the ratio between polytropic work and the real work. Polytropic work incorporates the RHE, providing this formulation:

  $$\eta_{pol} = \frac{L_{pol}}{L_i} = \frac{L_i - L_w}{L_i} \tag{2.24}$$

2.5 One-Dimensional (1-D) model

Over the past several decades, many researches have been dedicated to centrifugal compressors and their design activity. To develop high performance compressors, it is necessary to develop detailed performance of the individual elements of a centrifugal compressor stage.
Nowadays, Computational Fluid Dynamics represents the most advanced method used to design and estimate the performances of centrifugal compressors: the flow properties are obtained by numerically solving variations of Navier-Stokes equations, relying on complex 2D/3D geometry. Despite CFD provides highly accurate

results, three-dimensional simulations are computationally intensive and not always suitable for preliminary design phases, where faster evaluation methods are required.

One-dimensional (1-D) performance prediction models represent the most traditional and widely used approach for the preliminary design and analysis of centrifugal compressors: they offer extremely fast execution, clear physical interpretation, and the ability to perform parametric studies with minimal computational effort. For these reasons, they are widely adopted in the early design phase and for generating complete performance maps. The formulation of the 1-D problem is a reduction of the actual flow and originates mainly from empirical correlations coming from the experiments.

One-dimensional models can be categorised basing on the number of flow zones considered; three main groups have been identified:

- Zero-zone models: only the overall characteristics of the stage are considered (no need to divide the compressor in its different components). New design specifications are met by simple, direct, scaling of existing stages: this concepts follows the principles of similitude. This first level of modelling is appropriate whenever a stage can be modified by scaling to a different size; however, a similar stage must already exist. For this reason, more detailed models can be evaluated;

- Single-zone models: they provide the design and performance estimation of the centrifugal compressor by solving the governing equations at the mean streamline and at the main stations of the compressor components (like impeller throat, impeller outlet, ecc...) [15]. In this models, the losses assume a key role: they are originated from experimental correlation and are calculated to acquire the real flow conditions. It's a more complex model compared to the Zero-zone, providing increase accuracy and freedom of analysis;

- Two-zone models: the flow is divided in two parts, identified by 'jet-wake' approach. It assumes that the flow at the exit of the impeller is composed by an isentropic region with high velocities, jet, and a low momentum zone, the wake. Jet and wake combine through the mixing [16], [17].

This thesis uses a 1-D model obtained following the single zone approach to evaluate the performance of a centrifugal compressor depending on the losses considered. Because loss correlations strongly influence the accuracy of the 1-D model - and because each correlation comes with assumptions, calibration constants, and geometric dependencies — it is essential to:

- explain the physical origin of each loss mechanism;

- show the different correlations used to compute each loss mechanism.

The following chapter (3 is dedicated to the loss mechanisms and to the different formulations obtained from experimental activities to evaluate them.

Chapter 3

Loss Modelling in Centrifugal Compressors

The loss mechanism has a significant impact on performance prediction for a centrifugal compressor: understanding the influence of the various losses is a key aspect to improve the performance of the machine.
In the literature is plenty of studies concentrated in defining the different loss mechanism: the most important include the work of Jansen, Whitfield & Baines and Aungier. for each loss mechanism, several loss correlations are defined. Selecting a reliable set of loss correlations becomes crucial in computing the performances of a centrifugal compressor. Oh et al., in this context, performed a detailed study comparing the different loss models presented in open literature and suggested a set of loss models accurately predicting the performance of several different impeller configurations [18].
Meroni et al. proposed a different set in their mean-line design model of a centrifugal compressor for heat pump systems [15].
More recently, Zhang et al identified new sets of loss correlations based on the inlet tip relative Mach number and specific speed: for each condition, a set is selected [19].

In the following paragraphs, the loss correlations developed in the MATLAB code will be presented and the effects of each of them discussed. The correlations are divided into the main components of a centrifugal compressor stage: in our case, the losses have been implemented for the inlet guide vane, the impeller and the vaneless diffuser.

3.1 Inlet guide vane loss

In the literature, two main correlation are available:

- **Galvas**: he states that the loss related to inlet guide vane for centrifugal compressor is similar to the loss computed in the axial turbine (associated with the fluid kinetic energy, boundary layer thickness and blade geometrical structure of the device). The IGV loss is defined as a fraction of the ideal kinetic energy, depending on the exit flow angle of the inlet guide vane ($\alpha_{\mathrm{IGV,outlet}}$) [19]:

Kinetic Energy Fraction

$$e_{s,\mathrm{IGV}} = \frac{0.0076}{\cos\alpha_{\mathrm{IGV,outlet}} - 0.025}\left[1 + \frac{\cos\left(\alpha_{\mathrm{IGV,outlet}}/2\right)}{0.7}\right] \tag{3.1}$$

Ideal Kinetic Energy

$$(KE)_{id,\mathrm{IGV,outlet}} = \frac{V^2_{\mathrm{IGV,outlet}}}{2\left(1 - e_{s,\mathrm{IGV}}\right)} \tag{3.2}$$

Inlet Guide Vane Loss

$$\Delta h_{\mathrm{IGV}} = e_{s,\mathrm{IGV}}\,(KE)_{id,\mathrm{IGV,outlet}} \tag{3.3}$$

- **Aungier**: does not provide an explicit loss correlation for inlet guide vanes. IGVs are treated as aerodynamic stator elements, and their losses are evaluated using classical axial-compressor correlations (Howell, Ainley–Mathieson), applied to the geometry transformed onto the meridional plane.

  The IGV geometry is described by the inlet flow angle $\bar{\beta}_{-1}$, the exit flow angle $\bar{\beta}_0$, and the mid-passage angle $\bar{\beta}$. To apply axial-compressor correlations, all these angles are converted into the coordinate system of the cascade deviation models [6].

However, a recent study has demonstrated that these correlations underestimate the losses at low incidence angles when compared to the experimental results obtained by Coppinger in his studies.
Dario Valsesia, in his master thesis [20], described an 'original' empirical correlation obtained from interpolation of the experimental loss value obtained by Coppinger [21]. The pressure loss coefficient, having the following formula, has been extrapolated by using a third-degree polynomial to interpolate the experimental results:

$$\Delta p_{\mathrm{tot,IGV}} = \left(3\times10^{-5}\left|\alpha_{0b,\mathrm{deg}}\right|^3 - 0.001\left|\alpha_{0b,\mathrm{deg}}\right|^2 + 0.0248\left|\alpha_{0b,\mathrm{deg}}\right| + 0.2618\right)\left(p_{\mathrm{tot,0a}} - p_{0a}\right) \tag{3.4}$$

where $\alpha_{0b,deg}$ represents the outlet swirl angle (in degrees). This formulation allows to consider a minimal amount of loss due to IGV in design conditions, so where the angle is equal to zero. The result obtained defines a total pressure drop; this value is converted to a total specific enthalpy change thanks to a function depending on the thermodynamic properties of the fluid and the IGV outlet conditions [20].

$$\Delta h_{\mathrm{tot,IGV}} = c_p\left(1 - \frac{1}{\left(1 + \dfrac{\Delta p_{\mathrm{tot,IGV}}}{p_{\mathrm{tot,0b}}}\right)^{\vartheta}}\right)T_{\mathrm{tot,0b}} \tag{3.5}$$

3.2 Impeller Losses

The loss mechanism taking place in the impeller which negatively affects the efficiency of the device is composed by several contributions, each describing a different phenomena. Depending on the model followed, the type and amount of losses considered changes (Aungier defines a total of 14 loss mechanism, more than the amount considered by Oh et al., 8, or by Zhang, 11). However, they can be universally divided in two main groups:

- **INTERNAL LOSS MECHANISMS:** internal losses are those generated by the main flow through the compressor, compromising both the efficiency and the compression ratio. These include:
  - *INCIDENCE LOSS*
  - *BLADE LOADING LOSS*
  - *SKIN FRICTION LOSS*
  - *TIP CLEARANCE LOSS*
  - *MIXING LOSS*
  - *ENTRANCE DIFFUSION LOSS*
  - *CHOKE LOSS*
  - *SHOCK LOSS*
  - *HUB TO SHROUD LOSS*
  - *NORMAL SHOCK WAVE LOSS*
  - *SUPERCRITICAL MACH NUMBER LOSS*
- **PARASITIC LOSS MECHANISMS:** they refers to loss mechanisms generated from minor flow leaking away from the main flow through the compressor. They increase the impeller discharge stagnation enthalpy without any corresponding change in pressure: only the efficiency is affected by these losses. Are part of this category:
  - *DISC FRICTION LOSS*
  - *LEAKAGE LOSS*
  - *RECIRCULATION LOSS*

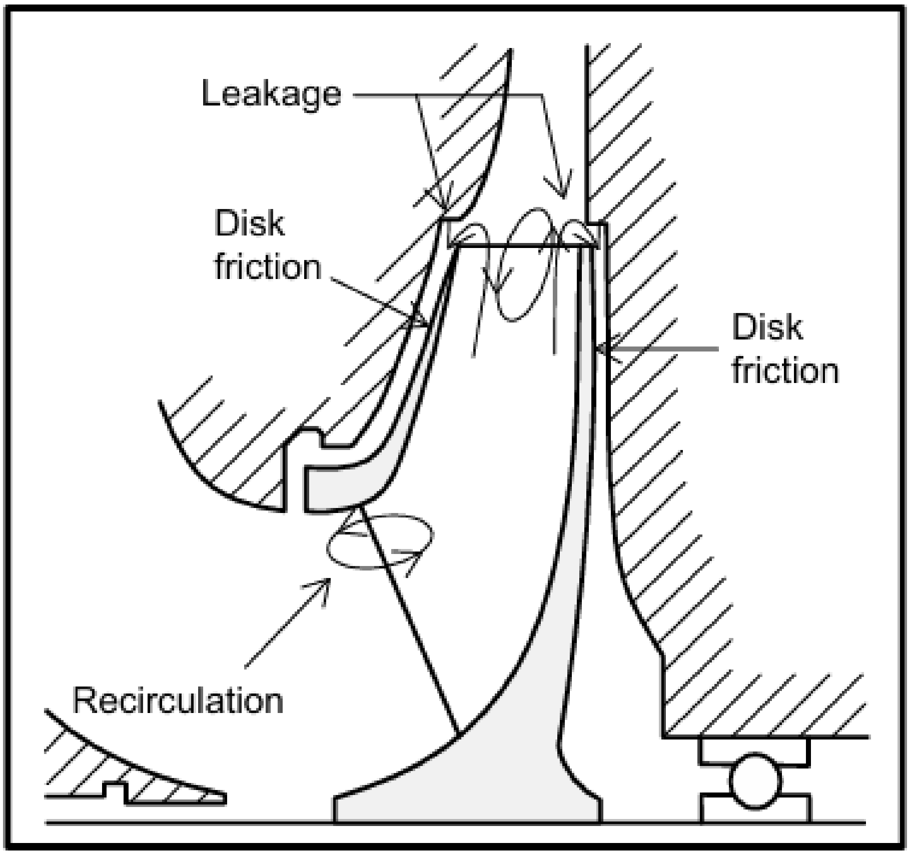

Figure 3.1: Schematic representation of parasitic losses occurring in the compressor system (adapted from Japikse and Baines) [18].

Each loss will be described in the following sections: for many of those, different correlations have been considered and the main formulations will be reported. Some losses, instead, have a lower impact on the performance of the compressor: for this reason, they have not been deeply analysed (up to now).

3.2.1 Incidence Loss

The incidence loss occurs when the inlet relative fluid flow angle (β_1) deviates from the actual blade inlet angle (β_{1b}). The fluid has to change direction immediately to adapt to the blade, resulting in a flow separation that causes significant loss in energy.
Lower is the incidence angle, so the difference between the blade direction and the relative flow, lower will be the energy loss. In the design process, incidence can be handled by acting on the 'inducer' (the initial part of the impeller), to improve stage performance.

Different correlation have been identified:

- *CONRAD*: found that the incidence loss is proportional to the squared of the tangential component of the relative velocity at the outlet.

$$\Delta h_{\text{inc}} = f_{\text{inc}} \frac{W_{u1}^2}{2} \tag{3.6}$$

f_{inc} is the incident coefficient, ranging from 0.5 to 0.7 (a good approximation is the mean value, 0.6) [19].

- *AUNGIER*: proposes another loss correlation assuming the flow direction to be axial at the impeller inlet. It is obtained from the difference experienced by the actual and the ideal relative velocity.

  $$\Delta h_{\text{inc}} = 0.4 \left(W_1 - \frac{V_{m1}}{\cos \beta_{1b}} \right)^2 \tag{3.7}$$

  This equation is applied to hub, shroud and mean surfaces: then, the incidence loss is obtained from the weighted average [22].

  $$\Delta h_{\text{inc,tot}} = \frac{10\, \Delta h_{inc,mean} + \Delta h_{\text{inc,hub}} + \Delta h_{\text{inc,shr}}}{12} \tag{3.8}$$

  Aungier provides also an improvement of this formulation, introducing an additional term taking into accounts the effect of the abrupt flow area contraction at the blade leading edge due to the latter's thickness:

  $$\Delta h_{\text{inc}} = 0.8 \left(1 - \frac{V_{m1}}{W_1 \cos \beta_1} \right)^2 + \left(\frac{Z_{\text{FB}}\, t_1}{2\pi r_1 \cos \beta_1} \right)^2 \tag{3.9}$$

  where Z_{FB} indicates the number of full-length blades and t_1 is the thickness of the blade at the inlet. As done before, the incidence loss is calculated for hub, shroud and mean surfaces; then, the equation (3.8) is applied. Anyway, the second contribution provided in equation (3.9) is negligible [6].

- *GRAVDAHL*: this formulation is derived using velocity triangles considerations; the results are similar to the other loss models [23].

  $$\Delta h_{\text{inc}} = \frac{1}{2} \left(U_1 - \frac{\cot(\beta_1)\, \dot{m}}{\rho_{01} A_1} \right)^2 \tag{3.10}$$

- *GALVAS*: suggests that the incidence loss is given by the difference between the actual flow angle and the optimum flow angle at impeller inlet. The optimum flow angle is obtained from the inlet velocity diagram characteristics and blade blockage B_1 at RMS diameter [19]:

  $$B_1 = 1 - \frac{Z_1\, t_1}{\pi\, D_1 \sin \beta_{1b}} \tag{3.11}$$

  $$\tan \varepsilon_1 = \frac{(1 - B_1)\, \tan \beta_1}{1 + B_1 \tan^2 \beta_1} \tag{3.12}$$

$$\beta_{\text{opt}} = \beta_{1b} - \varepsilon_1 \tag{3.13}$$

A velocity is computed from the relative inlet velocity and the difference of between the angles previously described: this quantity allows to compute the incidence loss.

$$W_L = W_{m1}\ \cos|\,\beta_{\text{opt}} - \beta_1| \tag{3.14}$$

$$\Delta h_{\text{inc}} = \frac{W_L^2}{2C_p} \tag{3.15}$$

3.2.2 Blade Loading Loss

This loss is associated to the momentum loss due to boundary-layer-build-up on the blade surfaces: a negative velocity gradient is detected near the blade surface, leading to the boundary layer growth. The increasing thickness of the boundary layer generates flow separation.

The most important formulations are provided by:

- *COPPAGE*: accordingly to his studies, the boundary layer growth is mainly influenced by the flow diffusion. The diffusion factor provides a quantitative measure of the total diffusion (deceleration of the flow) in the impeller and is calculated [19]:

  $$D_f = 1 - \frac{W_2}{W_{1s}} + \frac{0.75\,\Delta h_{\text{Euler}}\,W_2}{\left[\frac{Z}{\pi}\left(1 - \frac{D_{1s}}{D_2}\right) + \frac{2D_{1s}}{D_2}\right] 2\pi\,U_2^2} \tag{3.16}$$

  The first contribution is related to the diffusion of the flow passage in the form of a decrease in average velocity through the passage while the second part is related to the loading distribution on the blade: so, the diffusion factor is a function of the one-dimensional deceleration and turning of the flow [18].
  The theoretical head enthalpy is given by:

  $$\Delta h_{\text{Euler}} = U_2 V_{u2} - U_1 V_{u1} \tag{3.17}$$

  Computed the diffusion factor, the loss is obtained:

  $$\Delta h_{bl} = 0.05\,D_f^2\,U_2^2 \tag{3.18}$$

- *AUNGIER*: the blade loading loss is computed as the mixing loss derived from the relative velocity difference between the suction and pressure side [19]:

$$\Delta W = \frac{2\pi\, D_2\, V_{u2}}{Z\, L_b} \tag{3.19}$$

$$\Delta h_{bl} = \frac{\Delta W^2}{48} \tag{3.20}$$

3.2.3 Skin Friction Loss

The skin friction loss is caused by the adhesive forces between the channel surfaces (surfaces created by the hub, blades and shroud) and the fluid.
This loss is calculated by considering the equivalent hydraulic diameter, defined by Jansen [24]:

$$D_{hyd} = \frac{D_2, \cos(\beta_2)}{\frac{Z}{\pi} + \frac{D_2 \cos(\beta_2 b)}{b_2}} + \frac{\frac{1}{2}\left(\frac{D_{1s}}{D_2} + \frac{D_{1h}}{D_2}\right)\left(\frac{\cos(\beta_{1s})+\cos(\beta_{1h})}{2}\right)}{\frac{Z}{\pi} + \left(\frac{D_{1s}+D_{1h}}{D_{1s}-D_{1h}}\right)\left(\frac{\cos(\beta_{1s})+\cos(\beta_{1h})}{2}\right)} \tag{3.21}$$

Other two essential parameters needed to compute this loss are the skin friction coefficient (depending on Reynolds number, the hydraulic diameter and the kinematic viscosity), C_f, and the impeller flow length, L_b [19]:

$$\mathrm{Re} = \frac{U_2\, D_{\text{hyd}}}{\nu_{01}} \tag{3.22}$$

$$C_f = 0.0412\, \mathrm{Re}^{-0.1925} \tag{3.23}$$

$$L_b = \frac{\pi}{8}\left(D_1 - \frac{D_{1s} + D_{1h}}{2} - b_2 + 2L_z\right)\left(\frac{2}{\frac{\cos\beta_{1s} + \cos\beta_{1h}}{2} + \cos\beta_2}\right) \tag{3.24}$$

These parameters are applied by implementing the loss equations generally used in pipes.

- *COPPAGE*: stated that using the pipe friction correlation is suitable. It depends on the squared average relative velocity [24]:

  $$\overline{\left(\frac{W}{U_2}\right)}^2 = \frac{1}{2}\left[\frac{V_{m1}^2}{U_2^2} + \frac{D_1^2}{D_2^2} + \frac{W_2}{W_1}\left(\frac{V_{m1}^2}{U_2^2} + \frac{D_1^2}{D_2^2}\right)\right] \tag{3.25}$$

  The loss is then computed:

  $$\Delta h_{sf} = 5.6\, C_f\, \frac{L_b}{D_{\text{hyd}}}\, \overline{\left(\frac{W}{U_2}\right)}^2\, U_2^2 \tag{3.26}$$

  C_f is the friction coefficient and L_b is the length of the blade.

- *JANSEN*: improved the model of Coppage by applying the relations for a fully developed flow in a pipe of circular cross-section. The pipe is approximated imposing a diameter equal to the hydraulic diameter and the length simulated by the impeller flow passage length. Moreover, Jansen excluded the effects of non-uniform velocity distribution.

  A new definition of the average relative velocity is computed to obtain the skin friction loss [24]:

  $$\overline{W} = \frac{2W_2 + W_{1s} - W_{1h}}{4} \tag{3.27}$$

  $$\Delta h_{sf} = 2\, C_f \, \frac{L_b}{D_{\text{hyd}}} \, \overline{W}^2 \tag{3.28}$$

- *AUNGIER*: Aungier follows the same approach of Coppage and Jansen. As already highlighted in other case, the difference is given by small changes applied in the equations.
  The hydraulic diameter is proportional to the ratio between the cross section and the wetted parameter: the author suggests to compute it as the average of the throat and tip/shroud values [6], [25].

  $$D_{hyd,th} = \frac{4A_{th}}{2(\, b_1 + s\cos\beta_1 \,)\, Z_{bl,\text{full}}} \tag{3.29}$$

  $$D_{hyd,2} = \frac{4\pi\, d_2\, b_2/Z_{bl}}{2\pi\, d_2/Z_{bl} + 2b_2} \tag{3.30}$$

  The average relative velocity is:

  $$\overline{W}^2 = \frac{W_1^2 + W_2^2}{2} \tag{3.31}$$

  A check should be done about this value: Aungier states that it should be higher to the same value computed using the throat [6]. This is needed to not underestimate the loss: skin friction phenomena is dominated by the zones at higher speed, which are closer to the throat area. If the value computed is lower than the limit established by the throat area, the average relative velocity assumes this value.

  $$\overline{W}^2 \geq \frac{W_{1th}^2 + W_2^2}{2} \tag{3.32}$$

  Finally, the skin friction loss can be computed [6]:

  $$\Delta h_{SF} = 2\, C_f \, \frac{L_B}{d_H} \, \overline{W}^2 \tag{3.33}$$

3.2.4 Clearance Loss

In unshrouded impellers, a small clearance between the blade tip and casing is designed: it is necessary to allow the free rotation of the impeller.
The clearance is another factor that affects the performances of centrifugal compressors: it produces losses caused by the flow that leaks through the gap. The fluid leaks through the tip clearance from the higher pressure on the pressure side of the blade to the lower pressure on the suction side of the blade: the mixing between the two flows generates the loss in the form of small vortexes on the suction side [18].

The loss is calculated only for unshrouded (or open) impellers: in the shrouded (or covered) impellers the gap is not present, having the blades and the cover as a unique piece.

- *RODGERS*: describes the influence of the tip clearance size. The loss results to be function of the ratio of the tip clearance size to the impeller exit width [19]:

$$\Delta h_{\text{cl}} = 0.1 \, \frac{\epsilon}{b_2} \, U_2^2 \tag{3.34}$$

- *KRYLOV AND SPUNDE*: they expand the correlation proposed by Rogers by taking into account also the ratio of inlet to outlet radius [19]. It is calculated with the following formulation:

$$\Delta h_{\text{cl}} = 2 \, \frac{\epsilon}{b_2} \left(\frac{R_{1h} + R_{1s}}{2R_2} - 0.275 \right) U_2^2 \tag{3.35}$$

- *JANSEN*: the fluid behaviour is described by Jansen. According to his studies, the fluid experiences a rapid contraction followed by an expansion process through the tip clearance. The ratio of inlet to outlet density should be added to consider that phenomena [19]:

$$\Delta h_{\text{cl}} = 0.6 \, \frac{\epsilon}{b_2} \, V_{u2} \left[\frac{\left(\frac{4\pi}{b_2 Z}\right) \left(\frac{R_{1s}^2 - R_{1h}^2}{R_2 - R_{1t}}\right) V_{u2} \, V_2}{\left(1 + \frac{\rho_2}{\rho_1}\right)} \right]^{1/2} \tag{3.36}$$

- *AUNGIER*: defines a formulation depending on the clearance mass flow and the average pressure difference [24].
  The clearance mass flow is estimated as:

$$\dot{m}_{\text{cl}} = \frac{(\rho_1 + \rho_2) \, Z \, \epsilon \, L_m \, U_{\text{cl}}}{2} \tag{3.37}$$

  The velocity of the clearance gap is computed from:

$$U_{\text{cl}} = 0.816 \sqrt{\frac{2 \, \Delta p_{\text{cl}}}{\rho_2}} \tag{3.38}$$

The average pressure difference across the gap is obtained from the change in fluid angular momentum through the impeller:

$$\Delta p_{\mathrm{cl}} = \frac{\dot{m}\,(D_2 V_{u2} - D_1 V_{u1})}{Z\,\bar{D}\,\bar{b}\,L_m} \tag{3.39}$$

$$\bar{D} = \frac{D_1 + D_2}{2} \tag{3.40}$$

$$\bar{b} = \frac{b_1 + b_2}{2} \tag{3.41}$$

The clearance loss is finally obtained, using the average density between inlet and outlet:

$$\Delta h_{\mathrm{cl}} = \frac{\dot{m}_{\mathrm{cl}}\,\Delta p_{\mathrm{cl}}}{\dot{m}\,\bar{\rho}} \tag{3.42}$$

3.2.5 Mixing Loss

The mixing loss is a complicated mechanism that takes place at the end of the impeller: the fluid exiting the rotor, it's no longer uniform, but it's divided in two circumferential directions, forming the jet and the wake. Jet is a high energy region while wake is a region with low momentum: these two streams will mix after the impeller outlet, creating an additional loss.

Dean and Senoo were the first to treat the flow as two-dimensional, introducing the concept of 'two-zone model', with the jet and the wake dividing the passage in the circumferential direction [18].

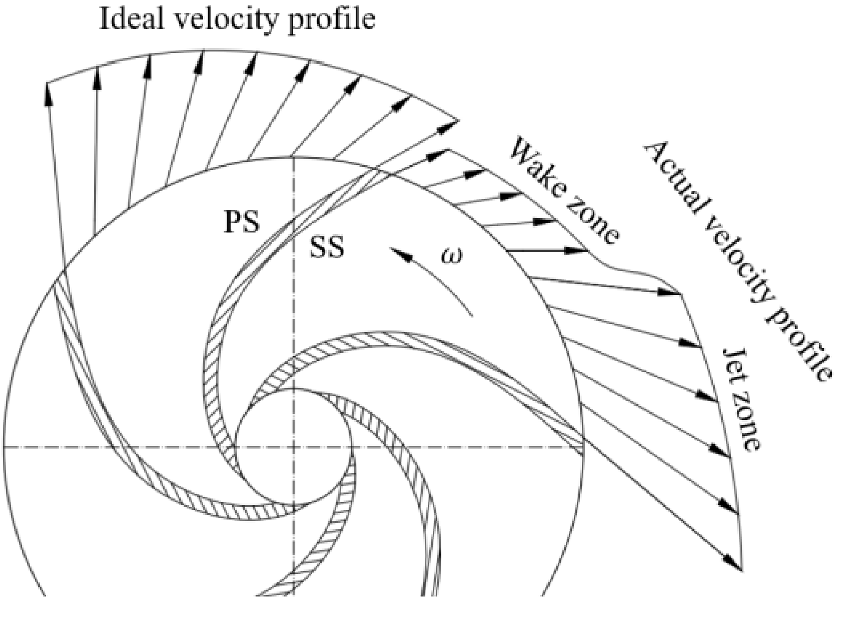

Figure 3.2: Jet-wake distribution at the impeller outlet) [26].

Ali discovered that the wake exists in the corner where the suction side and the shroud meet [19].

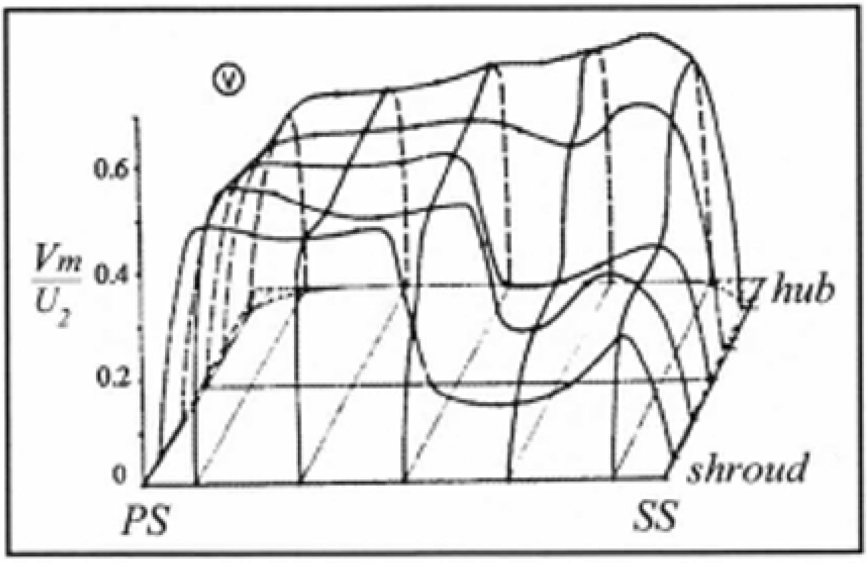

Figure 3.3: Velocity distribution at impeller exit) [26].

Two main loss correlations are generally used for the calculation of mixing:

- *AUNGIER*: stated that the wake flow mixes with jet at a velocity W_{sep}. The mixing loss can be evaluated by using the relative velocity difference between the separation point and the impeller outlet: the free stream velocity W_{sep} depends on the equivalent diffusion factor [19].

$$D_{\text{eq}} = \frac{W_{\max}}{W_2} \tag{3.43}$$

$$W_{\max} = \frac{W_1 + W_2 + \Delta W}{2} \tag{3.44}$$

ΔW represents the relative velocity difference between the suction and the pressure side: this value has been already introduced when talking about blade loading loss in equation 3.19.

$$W_{\text{sep}} = \begin{cases} W_2, & D_{\text{eq}} \leq 2 \\ W_2 \, \dfrac{D_{\text{eq}}}{2}, & D_{\text{eq}} > 2 \end{cases} \tag{3.45}$$

The relative velocity at the impeller outlet is given by.

$$W_{\text{out}} = \sqrt{\left[\frac{V_{m2}\, A_2}{\pi \, D_2 \, b_2}\right]^2 + W_{u1}^2} \tag{3.46}$$

The mixing loss is finally computed:

$$\Delta h_{\mathrm{mix}} = 0.5\,(W_{\mathrm{sep}} - W_{\mathrm{out}})^2 \tag{3.47}$$

- *JOHNSTON AND DEAN*: thanks to experimental analysis, stated that mixing phenomena is a rapid expansion process that ends very close to the impeller exit radius.
  They assumed a square-wave jet-wake relative velocity profile to exit from each blade passage and no variation of relative velocities across the passage depth. Moreover, they assumed the static pressure to be constant around the impeller rim, the number of blades to be large (Z $>$ 10) and no relative flow in the wake [18]. Thus, the resulting formulation is applicable for highly-loaded compressors with clear-cut 'jet and wake' structure [19].

  The equation describing the enthalpy loss due to mixing has been achieved starting from the conservation of mass, the moment of momentum and the linear momentum:

$$\Delta h_{\mathrm{mix}} = \frac{1}{1+\tan^2\alpha_2}\left(\frac{1-\varepsilon_{\mathrm{wake}}-b^*}{1-\varepsilon_{\mathrm{wake}}}\right)^2\frac{V_2^2}{2} \tag{3.48}$$

  where b^* is defined as the ratio between the vaneless diffuser width and the impeller exit width while $\varepsilon_{\mathrm{wake}}$ represents the wake width.
  For what it concern b^{1*}, a limitation is provided in the paper of Botha and Moolman [18]: according to them, the formulation is valid only for values of $b^{1*} \geq 1$. If this constrain is not respected, they suggest the need for an unknown contraction coefficient depending on the shape of the walls at impeller tip (in this cases, the value of b^{1*} has been set to 1).

  The wake width $\varepsilon_{\mathrm{wake}}$ usually ranges from 0.366 to 0.482. The mean value of the range can be used for a initial computation of the mixing loss.
  However, a procedure can be followed to determine the value of the wake width: an iterative solution, following the two-zone model approach, is performed until a proper convergence of the static pressure at impeller outlet is achieved, as suggested in the figure 3.4:

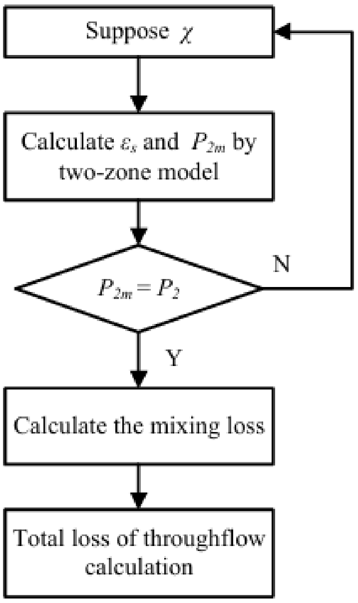

Figure 3.4: Iterative cycle to compute the width of the secondary flow [19].

> Two-zone model equations are described in Oh et Al. paper [27]: the author proposes three iterative procedures to obtain the thermodynamic parameters and velocities of the jet, wake and mixing zone. From this cycle, the width of the wake is computed and the mixing loss is evaluated.

3.2.6 Entrance Diffusion Loss

In many cases, the estimation of the incidence losses adopted before in section 3.2.1 underestimate the entrance loss at positive incidence angles: the flow adjustment taking place between the leading edge and the throat becomes the prevailing effect [19], [24]. To consider this phenomena, an entrance diffusion loss is calculated.

The model followed is provided by *AUNGIER*, followed by an important contribution given by *KOSUGE*: a key parameter is the relative velocity at the throat of the inducer.

$$\Delta h_{\mathrm{dif}} = 0.4\,(W_1 - W_{\mathrm{th}})^2 - \Delta h_{\mathrm{inc}} \tag{3.49}$$

If the incidence loss does not underestimate the entrance loss, it's possible to obtain a negative value of the entrance diffusion loss: in these cases, the entrance diffusion loss is set to zero [24].

Kosuge provided additional informations about this loss: he found out that the flow diffusion from inlet to throat is a primary indicator of inducer stall. In particular, when inducer stall occurs, a limitation should be applied to the entrance diffusion loss [19].
According to Aungier, stall occurs when:

$$\frac{W_{1s}}{W_{\mathrm{th}}} > 1.75 \tag{3.50}$$

When this condition is satisfied, the entrance diffusion is calculated as [24]:

$$\Delta h_{\mathrm{edf}} = \begin{cases} 0.4\,(W_1 - W_{\mathrm{th}})^2 - \Delta h_{\mathrm{inc}}, & \text{if } \Delta h_{\mathrm{edf}} > 0.5\,(W_{1s} - 1.75\,W_{\mathrm{th}})^2 - \Delta h_{\mathrm{lin}}, \\ 0.5\,(W_{1s} - 1.75\,W_{\mathrm{th}})^2 - \Delta h_{\mathrm{inc}}, & \text{otherwise.} \end{cases} \tag{3.51}$$

3.2.7 Hub-To-Shroud Loss

Hub-to-shroud loss is related to pressure gradients detected along the blade span (from hub to shroud) due to radial equilibrium issues (similar concept is already applied in blade loading loss, when the pressure gradient is considered among the blades).

AUNGIER defines the parameters needed to compute the loss: the first value is the streamline curvature, obtained from the difference in the streamline slope angles, as [22]:

$$\kappa = \frac{\alpha_{c2} - \alpha_{c1}}{L_m} \tag{3.52}$$

The loss is then computed:

$$\Delta h_{\mathrm{hs}} = \frac{(\kappa\,\bar{b}\,\overline{W})^2}{12} \tag{3.53}$$

$\bar{b}$ and $\bar{W}$ have been already computed respectively in equations 3.41 and 3.31.

3.2.8 Distortion Loss

According to *AUNGIER* [6], a loss is produced by the impeller tip meridional velocity profile distortion factor when the distorted flow mixes with the free stream flow, similarly to an abrupt expansion.
The tip distortion factor ζ is:

$$\lambda = 1/(1 - B_2) \tag{3.54}$$

B_2 is the tip blockage: initially, the empirical equation was derived from experimental work input curves. After defining the limit of that approach, Aungier was able to provide a new formulation of the tip blockage: the first equation, dated 1995 [22], was subsequently refined, in 2000 [6]. It's formulation is [28]:

$$B_2 = \begin{cases} \dfrac{2\Delta h_{sf}}{W_1^2}\dfrac{p_{01}-p_1}{p_{02}-p_2}\sqrt{\dfrac{W_1\,D_{hyd}}{W_2\,b_2}} + \left(0.3+\dfrac{b_2^2}{L_b^2}\right)\left(\dfrac{A_2\cos\beta_2}{A_1\cos\beta_{th}}\right)^2\dfrac{\rho_2\,b_2}{\rho_1\,L_b}, & \text{if shrouded,} \\ \dfrac{2\Delta h_{sf}}{W_1^2}\dfrac{p_{01}-p_1}{p_{02}-p_2}\sqrt{\dfrac{W_1\,D_{hyd}}{W_2\,b_2}} + \left(0.3+\dfrac{b_2^2}{L_b^2}\right)\left(\dfrac{A_2\cos\beta_2}{A_1\cos\beta_{th}}\right)^2\dfrac{\rho_2\,b_2}{\rho_1\,L_b} + \dfrac{\epsilon}{2b_2}, & \text{if open.} \end{cases} \tag{3.55}$$

B_2 depends on the skin friction loss (3.33.
Finally, the distortion loss is computed [22]:

$$\Delta h_\lambda = 0.5\,(\lambda-1)^2\,V_{m2}^2 \tag{3.56}$$

3.2.9 Choke Loss

Choke loss manifests when the choking condition is reached: the velocity of the fluid at throat is equal to the speed of sound. If the mass flow continues to increase, the compressor performance will drop rapidly: the losses are produce by a shock wave that appears in the throat at supersonic state.

The loss correlation is provided by *AUNGIER*: the choke loss has been related to the geometrical structure and aerodynamic blockage in the impeller throat. To consider the 'impeding' identified at the throat, a contraction ratio is introduced [19]:

$$C_r = \sqrt{\frac{A_1\,\cos\beta_{1b}}{A_{th}}} \tag{3.57}$$

The contraction ratio is limited:

$$C_r \le 1 - \left(\frac{A_1\,\cos\beta_{1b}}{A_{th}} - 1\right)^2 \tag{3.58}$$

The choke loss is computed basing on the value of a parameter X defined as:

$$X = 11 - 10\,\frac{C_r\,A_{th}}{A_{th}^*} \tag{3.59}$$

A_{th}^* is defined as the impeller throat area for which the assigned mass flow will yield a sonic velocity. It's formulation is provided by Dixon and Hall in [12]:

$$A_{\text{throat,crit}}^{\text{in}} = \frac{\dot m_{\text{ref}}}{\left(\frac{p_{0,\text{ref}}}{T_{0,\text{ref}}R_{\text{ref}}}\right)a_{0,\text{ref}}\left(\frac{2}{\gamma_{\text{ref}}+1}\right)^{\frac{\gamma_{\text{ref}}+1}{2(\gamma_{\text{ref}}-1)}}} \tag{3.60}$$

$$A_{\text{throat,crit}}^{\text{imp}} = \frac{\dot m_{\text{ref}}}{\left(\frac{p_{0,\text{ref}}}{T_{0,\text{ref}}R_{\text{ref}}}\right)a_{0,\text{ref}}\left(\frac{2+(\gamma_{\text{ref}}-1)\left(\frac{u_{1,\text{ref}}}{a_{0,\text{ref}}}\right)^2}{\gamma_{\text{ref}}+1}\right)^{\frac{\gamma_{\text{ref}}+1}{2(\gamma_{\text{ref}}-1)}}} \tag{3.61}$$

$$A_{\text{throat,crit}} = \max\left(A^{\text{imp}}_{\text{throat,crit}},\ A^{\text{in}}_{\text{throat,crit}}\right) \tag{3.62}$$

The throat area is found by considering the continuity equation: it is assumed that the speed reaches the speed of sound at some section. Two sections are considered: the first one computed refers to the inlet guide vane while the second one is referred to the impeller passage.
If the IGV is consider, the absolute speed reaches choking conditions; if the impeller is considered, the relative velocity reaches the speed of sound value.
From these sections, the maximum is considered.

Finally, the loss is calculated:

$$\Delta h_{\text{ch}} = \begin{cases} \frac{1}{2} W_1^2 \left(0.05\, X + X^7\right), & X > 0, \\ 0, & X \leq 0. \end{cases} \tag{3.63}$$

3.2.10 Supercritical Mach Number Loss

According to Aungier [6], supercritical Mach number loss is generated when a boundary layer separation occurs due to supersonic conditions at blade suction surface.

The loss i calculated as:

$$\Delta h_s = 0.2 \left[\left(M_{w1} - M_{w1cr}\right) W_{\max}\right]^2 \tag{3.64}$$

Where W_{max} has already been described in equation 3.44 and M_{w1cr} is:

$$M_{w1cr} = M_{w1} \frac{W^*}{W_{\max}} \tag{3.65}$$

W^* is the local sonic velocity.

3.2.11 Shock Loss

The shock loss is defined starting from the total pressure loss generated in an impeller due to fluid flowing through a shock wake, which is generated in the inlet suction side [19].
WHITFIELD AND BAINES provided the loss correlation, suggesting that the shock loss is caused by a normal shock wave at impeller inlet. In this case, the loss mainly depends on two ratios: the ratio of the throat to the inlet relative velocity and the ratio of the throat to the inlet static pressure [19]:

$$\Delta h_s = \frac{W_1^2}{2} \left\{1 - \left(\frac{W_{\text{th}}}{W_1}\right)^2 - \left(\frac{2}{(\gamma - 1)\, M_{w1}^2}\right)\right\} \left[\left(\frac{p_{\text{th}}}{p_1}\right)^{\frac{\gamma}{\gamma-1}} - 1\right] \tag{3.66}$$

AUNGIER also discussed about this loss mechanism: when the entrance velocity, calculated at hub, mean and shroud surfaces, exceeds sonic conditions, shock relations are used to reduce them to sonic conditions. This consideration suggest to assume a shock loss.
No clear formulation is provided in [22] or [6].

3.2.12 Recirculation Loss

The recirculation loss takes into account the flow that turns around after leaving the impeller and goes back to the impeller section. Higher is the absolute flow angle (from the meridional direction) of the flow exiting the impeller, easier will be the recirculation phenomena; also the diffusion factor has huge impact on the loss [18].

Different correlation has been proposed:

- *COPPAGE*:

  $$\Delta h_{\mathrm{re}} = 0.02\,\sqrt{\tan\alpha_2}\,D_f^2\,U_2^2 \tag{3.67}$$

  The diffusion factor equation is already been exploited (equation 3.16)

- *AUNGIER*: proposed a modify approach, using the equivalent diffusion factor D_{eq}. When the equivalent diffusion factor (equation 3.43) is higher than a certain number representing the stall of the impeller (according to Leiblein equal to 2, as already seen in 3.2.5), the loss is calculated as [24]:

  $$\Delta h_{\mathrm{rc}} = \begin{cases} \left(\dfrac{D_{\mathrm{eq}}}{2} - 1\right)\left(\dfrac{W_{u2}}{V_{m2}} - 2\tan\beta_2\right), & \text{if } D_{\mathrm{eq}} > 2, \\ 0, & \text{otherwise.} \end{cases} \tag{3.68}$$

- *OH*: created a new loss model by placing more emphasis on the flow angle distribution. A hyperbolical functional form has been developed to compute the loss [18]:

  $$\Delta h_{\mathrm{re}} = 8\times10^{-5}\,\sinh(3.5\,\alpha_2)\,D_f^2\,U_2^2 \tag{3.69}$$

  However, this loss mechanism shows some limits when applied to highly-loaded centrifugal compressors.

- *RODGERS*: came up with a recirculation loss formulation which is independent from the diffusion factor. The equation has been constructed with empirical constants [24]:

  $$\Delta h_{\mathrm{rc}} = 0.032\left(\frac{U_2^2}{C_{m1}}\right)^2 \tag{3.70}$$

3.2.13 Disk Friction Loss

Disk friction loss is generated by the frictional torque of shear forces between the rotating disk and and the housing: the geometry of the impeller and of the casing have a notable impact on the loss.

The man formulations are provided by:

- *DAILY & NECE*: conducted an experimental and theoretical study of the rotation of a smooth plane disk enclosed within a right-cylindrical chamber. They developed theoretical models for all the different flow regimes, coming up with the following loss correlation in which a disk friction factor is introduced (depending on the Reynolds number) [19]:

$$\mathrm{Re}_{df} = \frac{U_2 R_2}{\nu_2} \tag{3.71}$$

$$f_{df} = \begin{cases} \dfrac{2.67}{\sqrt{\mathrm{Re}_{df}}}, & \mathrm{Re}_{df} < 3 \times 10^5, \\ \dfrac{0.0622}{(\mathrm{Re}_{df})^{0.2}}, & \mathrm{Re}_{df} \geq 3 \times 10^5, \end{cases} \tag{3.72}$$

$$\Delta h_{df} = f_{df}\,(\rho_1 + \rho_2)\, R_2^2 U_2^3 \Big/ (8\,\dot{m}) \tag{3.73}$$

  Daily and Nece provided also a formulation in which a coefficient K_f is computed as a function of the clearance gap ϵ alongside the Reynolds number [24]:

$$K_f = \begin{cases} \dfrac{3.7\left(\dfrac{2\epsilon}{D_2}\right)^{0.1}}{\mathrm{Re}_2^{0.5}}, & \text{if } \mathrm{Re}_2 \leq 30{,}000, \\ \dfrac{0.102\left(\dfrac{2\epsilon}{D_2}\right)^{0.1}}{\mathrm{Re}_2^{0.2}}, & \text{otherwise.} \end{cases} \tag{3.74}$$

  The loss was defined as:

$$\Delta h_{df} = 0.25\, K_f\, \frac{\bar{\rho}\, D_2^2\, U_2^3}{4\,\dot{m}} \tag{3.75}$$

  $\bar{\rho}$ is the mean density value.

- *SHEPHERD*: proposed a model depending directly on Reynolds number rather then defining a disk friction factor. The Reynolds number is defined with respect to the stagnation quantities [19]:

$$\mathrm{Re} = \frac{U_2 D_2}{\nu_{02}} \tag{3.76}$$

$$\Delta h_{df} = 0.01356\, \rho_2 U_2^3 D_2^2 / \left(\dot{m}\, \mathrm{Re}^{0.2}\right) \tag{3.77}$$

- *BOYCE*: provided a disk friction based on the experimental work of Watabe [24]:

$$\Delta h_{df} = f_{df} \left(1 + \frac{p_2}{p_1}\right) \frac{\Delta h_{\mathrm{Euler}}}{2} \frac{V_1}{U_2} \frac{R_2^2}{R_{1s}} \left[1 - \left(\frac{R_{1h}}{R_2}\right)^2\right] \tag{3.78}$$

  In this equation, the energy exchanged across the impeller Δh_{eu} obtained with Euler formulation is needed.

- *AUNGIER*: the starting point of his loss model is given by the description provided by Daily and Nece. The starting point is the definition of a disk torque coefficient: four different flow regimes were considered by Daily and Nece and four different equations (one for each flow regime) have been obtained [6]:

$$\begin{cases} C_{M1} = \dfrac{2\pi}{(\epsilon/R_2)\,\mathrm{Re}}, & \text{laminar, merged boundary layers,} \\ C_{M2} = \dfrac{3.7\,(\epsilon/R_2)^{0.1}}{\sqrt{\mathrm{Re}}}, & \text{laminar, separate boundary layers,} \\ C_{M3} = \dfrac{0.08}{(\epsilon/R_2)^{1/6}\,\mathrm{Re}^{1/4}}, & \text{turbulent, merged boundary layers,} \\ C_{M4} = \dfrac{0.102\,(\epsilon/R_2)^{0.1}}{\mathrm{Re}^{0.2}}, & \text{turbulent, separate boundary layers.} \end{cases} \tag{3.79}$$

  Re is defined in equation 3.71. To determine which flow regime exists, the four torque coefficient are calculated and the maximum is selected C_{Ms}. At high values of *Re*, the roughness effects increases the torque coefficient up to a condition in which the disk becomes 'fully rough': in this case, the torque coefficient doesn't vary any more with Reynolds number. Introducing the value of the roughness *e*, the 'fully rough' disk torque coefficient is calculated as:

$$C_{Mr} = \frac{1}{\left(3.8\,\log_{10}\left(\frac{R_2}{\mathrm{e}}\right) - 2.4\left(\frac{\epsilon}{R_2}\right)^{0.25}\right)^2} \tag{3.80}$$

  To compute the proper value of the torque coefficient, taking into account also the roughness effect, a new definition of Reynolds number has been developed:

$$\mathrm{Re}_s = \frac{1100\left(\frac{\mathrm{e}}{R_2}\right)^{-0.4}}{\sqrt{C_M}} \tag{3.81}$$

A Reynolds number is also computed for the 'fully rough' case:

$$Re_r = \frac{1100\,R_2}{e} - 6 \cdot 10^6 \tag{3.82}$$

According to Daily and Nece, the disk torque coefficient can be computed as:

$$C_M = \begin{cases} C_{Ms}, & \text{if } Re < Re_s, \\ C_{Mr}, & \text{if } Re > Re_r, \\ C_{Ms} + (C_{Mr} - C_{Ms})\,\dfrac{\ln\left(\frac{Re}{Re_s}\right)}{\ln\left(\frac{Re_r}{Re_s}\right)}, & \text{if } Re_s \le Re \le Re_r. \end{cases} \tag{3.83}$$

Aungier introduced an improvement of this approach based on empirical correlations; the torque coefficient obtained above (equation 3.83) is denoted as C_{M0}. The new value is given by:

$$C_M = C_{M0}\left(\frac{1-K}{1-K_0}\right)^2 \tag{3.84}$$

The terms K (with seal leakage) and K_0 (no seal leakage) are obtained from observations on the clearance gap leakage flows:

$$K_0 = \frac{0.46}{1 + 2\frac{\epsilon}{d}} \tag{3.85}$$

$$K_f = \frac{V_{u2}}{U_2} \quad \text{Impeller tip swirl parameter} \tag{3.86}$$

$$C_q = \frac{(\dot{m}_L\,\rho_2\,R_2\,U_2/\mu_2)^{1/5}}{2\pi\,\rho_2\,R_2^2\,U_2} \tag{3.87}$$

Where $\dot{m}_L$ is the leakage mass flow.

$$K = K_0 + C_q\,(1.75\,K_f - 0.316)\,\frac{R_2}{\epsilon} \tag{3.88}$$

The impeller disk friction torque coefficient is computed independently for the disk and the cover, respectivately called C_{MD} and C_{MC} [6]:

$$C_{MD} = 0.75 C_M \tag{3.89}$$

$$C_{MC} = \begin{cases} 0.75\, L_m C_M \left[1 - \left(\dfrac{D_{1s}}{D_2}\right)^5\right] \dfrac{1}{(R_2 - R_1)}, & \text{if shrouded impeller,} \\ 0, & \text{if ipen impeller.} \end{cases} \tag{3.90}$$

Finally, the disk friction loss is computed:

$$\Delta h_{df} = (C_{MD} + C_{MC})\, \frac{\rho_2\, R_2^2}{2\,\dot{m}}\, U_2^3 \tag{3.91}$$

3.2.14 Leakage Loss

Some of the flow exiting the impeller leaks through the clearance gaps and labyrinth seals to the lower pressure regions, causing the leakage loss. For open impellers, the loss occurs in the disk-housing gap while for the shrouded ones in the labyrinth seals.

Several correlations are presented in literature, differentiating between open and shrouded impellers. Starting from the *OPEN* impellers, the loss formulations proposed are:

- *AUNGIER*: assumed that half of the clearance gap leakage flow is re-entrained into the blade passage and re-energized by the impeller [29].
  For this reason, the leakage mass flow rate correspond to the one calculate in section 3.2.4 (equation 3.37). Also the other parameters, like the velocity in the gap U_{cl}, is taken from that section.
  The leakage loss is:

  $$\Delta h_{\text{leak}} = \frac{\dot{m}_{cl}\, U_{cl}\, U_2}{2\,\dot{m}} \tag{3.92}$$

  A different formulation, still referred to Aungier, is provided by Zhang et al. [19]:

  $$\Delta h_{lk} = \rho_2\, \epsilon\, U_2\, \frac{1.332\,(R_2 V_{u2} - R_1 V_{u1})}{2\,\bar{r}\,\bar{b}} \tag{3.93}$$

- *JANSEN*: similarly to Aungier, Jansen proposed a formulation for open impellers:

  $$\Delta h_{lk} = 0.6\, \frac{\epsilon}{b_2}\, V_2 \sqrt{\frac{4\pi}{b_2\, Z} \left(\frac{R_{1s} - R_{1h}}{R_2 - R_{1s}}\right) \left(1 + \frac{\rho_2}{\rho_1}\right) V_{u2} V_1} \tag{3.94}$$

For covered impellers, the gap in which the flow can leak is given by the seal: the leakage flow is calculated as a function of the seal geometry.
Two models are presented:

- AUNGIER: following the approach and results proposed by Egli [6], the leakage flow is computed by means of three coefficients relying on seal's geometry and empirically obtained. Aungier followed the approach and results proposed by Egli [6]. A schematization of the seal is necessary to understand which are the main parameters:

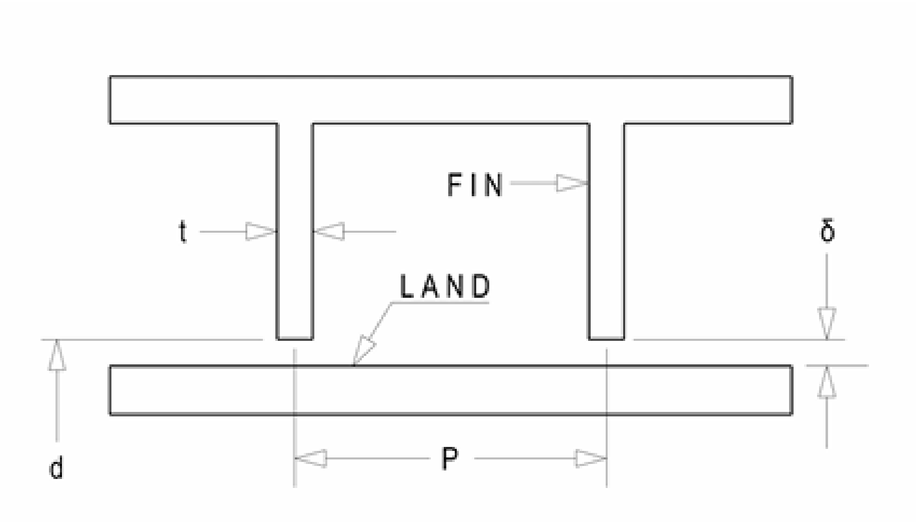

Figure 3.5: Typical geometry of a straigth-through labyrint seal [25].

δ represents the seal clearance, t the thickness of the fins, P the pitch and d the seal diameter.

The first coefficient is the contraction coefficient C_r, depending on the ratio δ/t:

$$C_r = 1 - \frac{1}{3 + \left(\frac{54.3}{1+100\,\delta/t}\right)^{3.45}} \tag{3.95}$$

Then, the seal throttling coefficient is defined: it's a function of the seal pressure ratio p_R and the number of fins in the seal N:

$$C_t = \frac{2.143\,[\ln(N) - 1.464]}{N - 4.322}\;(1 - p_R)^{0.375\,p_R} \tag{3.96}$$

Finally, the carry-over coefficient C_c is computed: it accounts for the residual kinetic energy carried through from one restriction to the next.

$$C_t = 1 + X_1 \frac{\dfrac{\delta}{P} - X_2 \ln\left(1 + \dfrac{\delta}{P}\right)}{1 - X_2} \tag{3.97}$$

X_1 and X_2 formulations depends on the number of fins:

$$X_1 = \begin{cases} 15.1 - 0.05255\,\exp[\,0.507\,(12 - N)]\,, & N \leq 12, \\ 13.15 + 0.1625\,N, & N > 12. \end{cases} \tag{3.98}$$

$$X_2 = \begin{cases} 1.058 + 0.0218\,N, & N \leq 12, \\ 1.32, & N > 12. \end{cases} \tag{3.99}$$

The ratio δ/P shows an upper limit: if the limit is exceeded, the ratio assumes the value of the limit.

$$\frac{\delta}{P} \leq X_2 - 1 \tag{3.100}$$

The leakage mass flow is defined by:

$$\dot{m}_L = \pi\, d\, \delta\, C_t\, C_c\, C_r\, \rho_2\, \sqrt{R T_2} \tag{3.101}$$

The leakage loss is:

$$\Delta h_{lk} = \frac{\dot{m}_L\, \Delta h_{eu}}{\dot{m}} \tag{3.102}$$

- *OSNAGHI*: another formulation is provided by Osnaghi to compute the leakage mass flow; the loss is then computed as Aungier proposed.
  There is again a strong dependency on the seal geometry identified by a coefficient C_D; first the leakage area is computed relying on the seal clearance δ:

$$A_{leak} = \pi\, D_{1s}\, \delta \tag{3.103}$$

$$\dot{m}_L = C_D\, A_{leak}\, \rho_1 \sqrt{\frac{2\,\Delta h_{is}}{N}} \tag{3.104}$$

The leakage loss is computed as equation 3.102.

3.3 Vaneless diffuser losses

There is always a vaneless space directly following the impeller in which the flow has the possibility to diffuse, regardless of the the presence of a vaned diffuser. The vaneless space produce losses due to friction and diffusion [19].
The main formulation are provided by:

- *STANITZ*: he developed the mass, momentum and energy conservation equation for vaneless diffuser. The enthalpy loss is calculated:

$$\Delta H_{\mathrm{vld}} = C_p T_{02} \left[\left(\frac{p_3}{p_{03}} \right)^{\frac{\gamma-1}{\gamma}} - \left(\frac{p_3}{p_{02}} \right)^{\frac{\gamma-1}{\gamma}} \right] \tag{3.105}$$

- *COPPAGE*: simplified the general equations into semi-empirical alternation. The relation between mach number and radius is sufficiently approximated [24]:

$$\Delta h_{\mathrm{vld}} = \frac{2}{3} \left(\frac{D_2}{D_3} \right)^{\frac{3}{2}} \left(\frac{C_f D_2}{8 b_2} \right) \frac{C_2^2}{\cos^2(\alpha_2)} \tag{3.106}$$

where C_f is given by:

$$C_{f,\mathrm{vld}} = k \left(\frac{1.8 \times 10^5}{\mathrm{Re}} \right)^{0.2} \tag{3.107}$$

Chapter 4

MATLAB Framework for the 1-D Performance Prediction of Centrifugal Compressors

This chapter presents the MATLAB-based computational framework developed to predict the thermodynamic performance of centrifugal compressors using a one-dimensional (1-D) modelling approach. The code is designed to analyse different compressor geometries: provided the input geometric parameters and set the loss correlations to be applied, the performances of the compressor are evaluated.
A key characteristic of the developed MATLAB framework is its high level of modularity: each physical phenomenon (incidence, friction, leakage, slip, mixing, diffuser losses) and each computational operation (geometry loading, thermodynamic updates, velocity-triangle evaluation, iterative density loops) is isolated in an independent function or script. In this way, future changes or integration can be easily applied, without interfering with other code parts.

The logical flow is described in fig. 4.1: firstly, three input files are provided to the code. The first one reports the geometric parameters of the compressor module, the second allows to set the operating conditions of the compressor and the last one document provides the tolerances and limits to be respected when running the performance codes (respectively identified as `.data, .analysis and .settings`).

The three input documents are checked by a dedicated function, `read_check_convert`, which ensures the availability and correctness of the files, prepares the the necessary structures for further calculations and converts the input values in SI units.

The performance analysis can starts: `perfcalc` Computes parameters such as efficiency, mass flow rate, pressure ratio, and losses and returns detailed thermodynamic and velocity data for the analysis. In this case, the impeller and the diffuser performance are evaluated thanks to the functions `impecalc and diffcalc`.

The results obtained from the performance analysis are compared to the experimental data and the plots are generated.

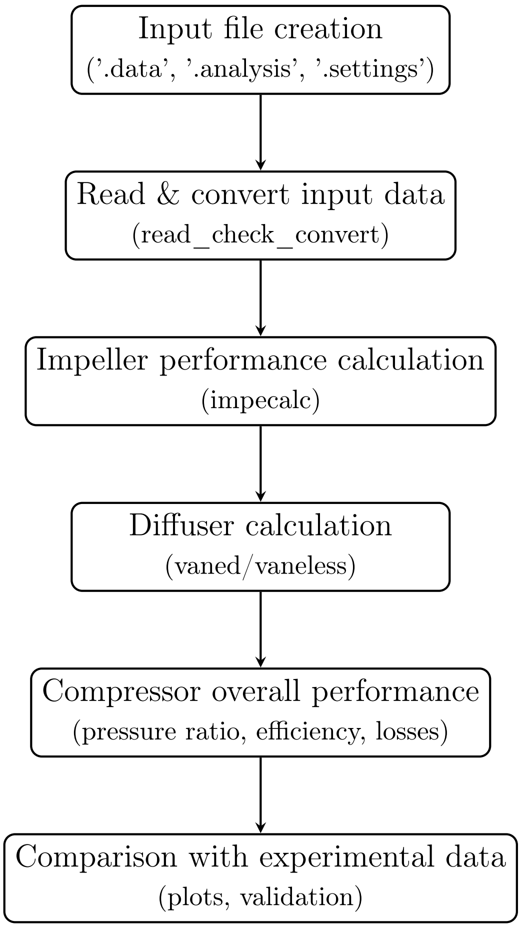

Figure 4.1: Flow chart of the MATLAB 1-D compressor performance code.

The description of the different functions is given in the following sections.

4.1 Input Files

Three input files are requested to run the codes and compute the performance of the compressor.

- `_input.data`: this input file contains different parameters: first, the mechanical and electrical efficiency are reported. Then the fluid properties and the inlet conditions should be given by the user, including the mass flow rate and the rotational speeds at which the device works. The main part of the document is dedicated to the geometric parameters: impeller, inlet duct, vaneless space, diffuser, volute and outlet duct should be described. The impeller, in particular, requires several values: number of blades, radius at the inlet section (for hub and shroud), blade specifications (inlet and outlet angles, width and thickness), the clearance and the seal geometry in case of a shrouded impeller. Similar values are required from the vaned diffuser: that module has not been developed in this thesis project.

- `_input.analysis`: the operating conditions are set in this file. The user can select the components to be consider in the performance analysis and select the type of component (for example, if the impeller is open or shrouded, if the diffuser in vaneless or vaned). Moreover, the loss correlations equations to be used can be selected alongside the methods to compute other important parameters, like the slip factor. This is the document allowing to investigate different loss models.
- `_input.settings`: in the settings code, several control parameters are specified: the majority of them are convergence tolerances used for the iterative cycle developed in the main codes.

All these files are usually called with the name of the compressor followed by the designation used in the previous lines.

4.2 `read_check_convert.m`

`read_check_convert.m` is the function that checks if the input files are present and if they are properly written: an error message is generated in case of any problem to provide a feedback to the user. The first lines of the code are dedicated in searching the input file through the different directories depending on the compressor that should be evaluated.
Then, the files are read, all the lines are stored in a matrix and the input data, extrapolated from the matrix, are collected in a data structure.

A key feature of this function is the loss setup: the user can decide which loss correlation setup use to evaluate the compressor performances. The code divides between internal and parasitic losses: since the internal losses are numerous, a vector is constructed. Each position of the vector refers to a specific loss mechanism, as shown in table 4.1. The numbers placed into the vector, instead, defines the loss correlation to be used for the corresponding loss mechanism.

Table 4.1: Structure of the `methods_vector` used to activate each loss model.

Index (i)	**Loss Mechanism**
1	Incidence loss (Incloss)
2	Blade friction loss (Bldloss)
3	Skin-friction loss (Skfloss)
4	Mixing loss (Mixloss)
5	Wake model
6	Clearance loss (Cleloss)
7	Edge/diffusion loss (Edfloss)
8	Disc friction loss (Disloss)
9	Hub–shroud slip loss (H2sloss)
10	Choking loss (Chkloss)
11	Non-swirling loss (Nswloss)
12	Small-clearance loss (Smaloss)

This approach allows to use predefined loss correlation models easily found in literature, like Oh et al., Zhang and Meroni loss correlation.
The parasitic losses follows the same approach of the internal ones.

Another important feature of the function is the conversion of the collected input data to the international system of units (SI). In particular, the thermodynamic properties of the working fluid are initialise from CoolProp library. CoolProp is an open-source and high-accuracy property database that provides equations of state and transport correlations for a large number of fluids. Using CoolProp ensures that the one-dimensional model is not limited by ideal-gas assumptions and that properties such as enthalpy, specific heats, density and viscosity are evaluated consistently over the entire operating range. The code extracts the following key properties at the inlet conditions of the compressor:

- the specific gas constant R, computed as the ratio between the universal gas constant and the molar mass provided by CoolProp;
- the specific heat at constant pressure c_p and at constant volume c_v, from which the isentropic exponent $\gamma = c_p/c_v$ is obtained;
- the reference dynamic viscosity μ_{ref}, evaluated at $T = 273.15$ K and $p = 101{,}325$ Pa;
- an `AbstractState` object (`fluid_as`) that is later used to update fluid properties at arbitrary (T, p) pairs within the solver.

This initialisation guarantees that every thermodynamic or transport property used in the performance model (e.g. density, enthalpy, viscosity, speed of sound) is retrieved directly from CoolProp, thus improving physical consistency and avoiding ideal-gas simplifications that could introduce non-negligible errors at high pressure ratios or off-design conditions.

4.2.1 Adding a New Compressor

To include a new compressor, it's requested to create a folder containing `_input.analysis`, `_input.settings`, `_input.data`. Then, `read_check_convert.m` should be controlled: if the new compressor is saved in a folder already managed by the code, no changes should be applied. Otherwise, if a new folder is created, adjustment should be applied to allow the code to find and read the input files.

4.3 `perfcalc.m`

`perfcalc.m` is the core function for performance calculation: it's composed by several subfunctions providing the performance estimation of each component of the compressor, based on the input file set up.
In order, the code runs the subfunctions related to:

- inlet duct: placed prior to the rotor inlet section;
- impeller;
- vaneless space: component connecting the rotor outlet section to the stator inlet;
- diffuser;
- volute;
- additional components based on the structure of the compressor evaluated (like the conical diffuser duct and the outlet duct).

The different modules are switched on when the component performance analysis is requested by the user; moreover, `perfcalc.m` manages the different components configuration, like if the impeller has splitters or no, if the diffuser is vaned or vaneless and more.
Several parameters are computed by the code: efficiency, mass flow rate, pressure ratio and losses, followed by detailed thermodynamic and velocity data for the analysis.

The two main subfunctions of `perfcalc.m` are related to the impeller and diffuser performance estimation: `impecalc.m` and `diffcalc.m` description is provided in the following paragraphs.

4.3.1 `impecalc.m`

As the name suggests, `impecalc.m` is the function aimed to analyse the impeller: it returns the efficiency, the pressure ratios and the losses taking place in the rotor. Structures containing the thermodynamic properties and the velocities are generated to properly analyse the evolution throughout the impeller.
The code uses three main iterative cycle to estimate the parameters at the inlet,

at the throat and the outlet cross section.

The first iterative cycle is dedicated to the computation of the impeller's inlet conditions: the density at section 1 has been assumed equal to the density at point 00 (inlet of the compressor, considering an inlet duct preceding the rotor). Having the density and purely axial inlet conditions, the velocities can be computed. Using the equations reported in chapter 2, the thermodynamic properties can be described. The density value obtained from this calculation is compared to the first guess value: if the converge criterion is satisfied, the iterative cycle ends. Otherwise, a new loop is performed starting from the value of density returned from the previous cycle.

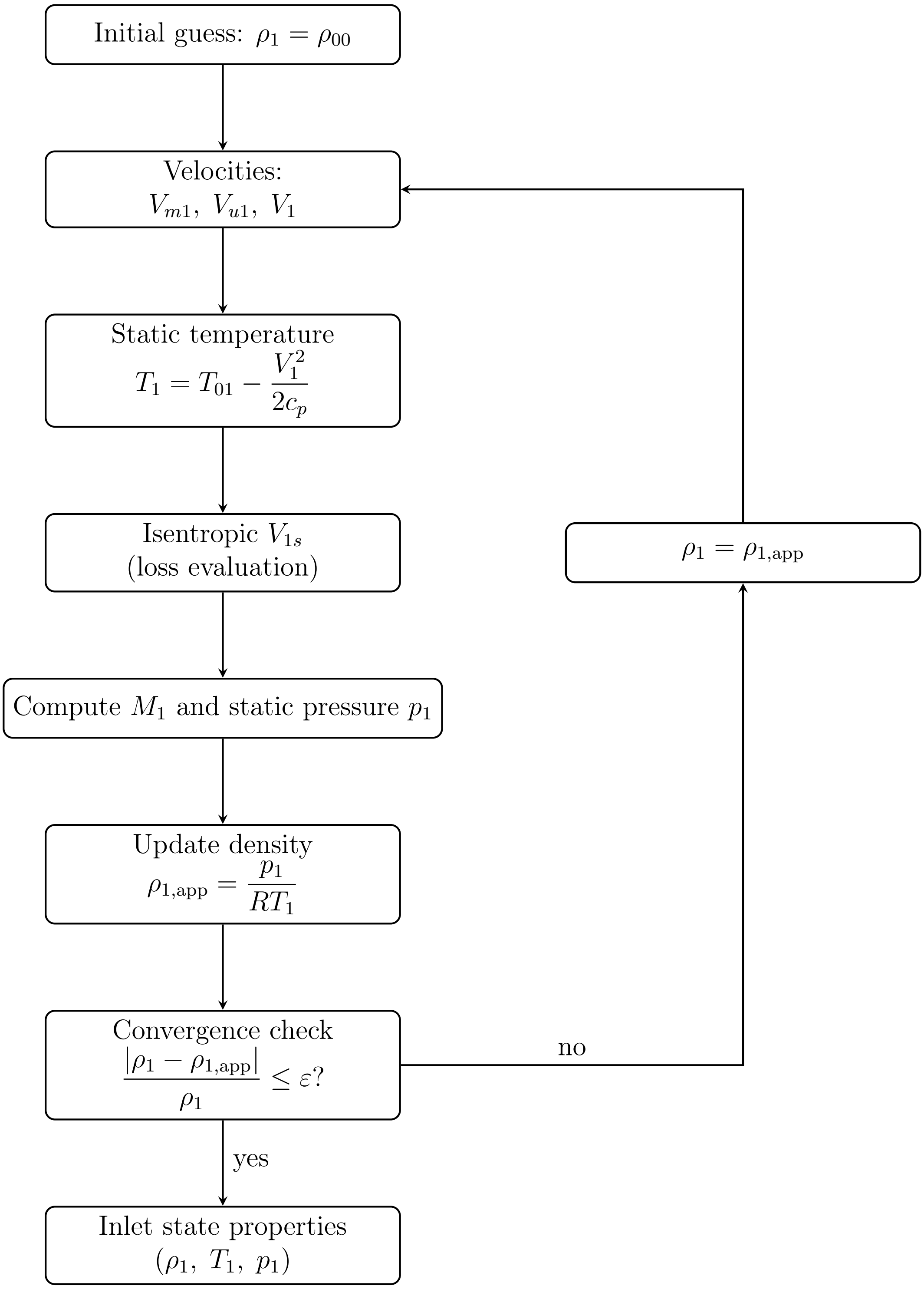

Figure 4.2: Flowchart of the iterative inlet-condition solver.

The velocity triangle are then computed for the mean stream line, the hub and the shroud.

The evaluation proceeds with the definition of the throat section: this area has huge importance in the definition of the choking conditions. The geometric parameters are computed, followed by the velocities and the first part of the compression taken into account.

The impeller's outlet condition are then computed: first of all, the outlet cross-section is calculated through the geometric parameters reported in the input file. Farther, other values needed in the losses' computation are in this phase computed, like the meridional and radial length of the compressor and the hydraulic diameter.
Another iterative cycle is used, following a similar approach of the computation of the inlet conditions. The convergence is searched between a guessed value of density ρ_2 and the value of density obtained through the calculation of the velocities and the thermodynamic properties. In this case:

$$\rho_{2,guess} = 2.5 * \rho_1 \tag{4.1}$$

The compression happening through the impeller is considered and the guess value of density is set equal to the inlet one ρ_1 multiplied for a constant term, qualifying the compression: without that factor, the convergence was reached at lower value of density, significantly decreasing the pressure ratio and the efficiency of the impeller.
The loop flowchart is shown in figure 4.3:

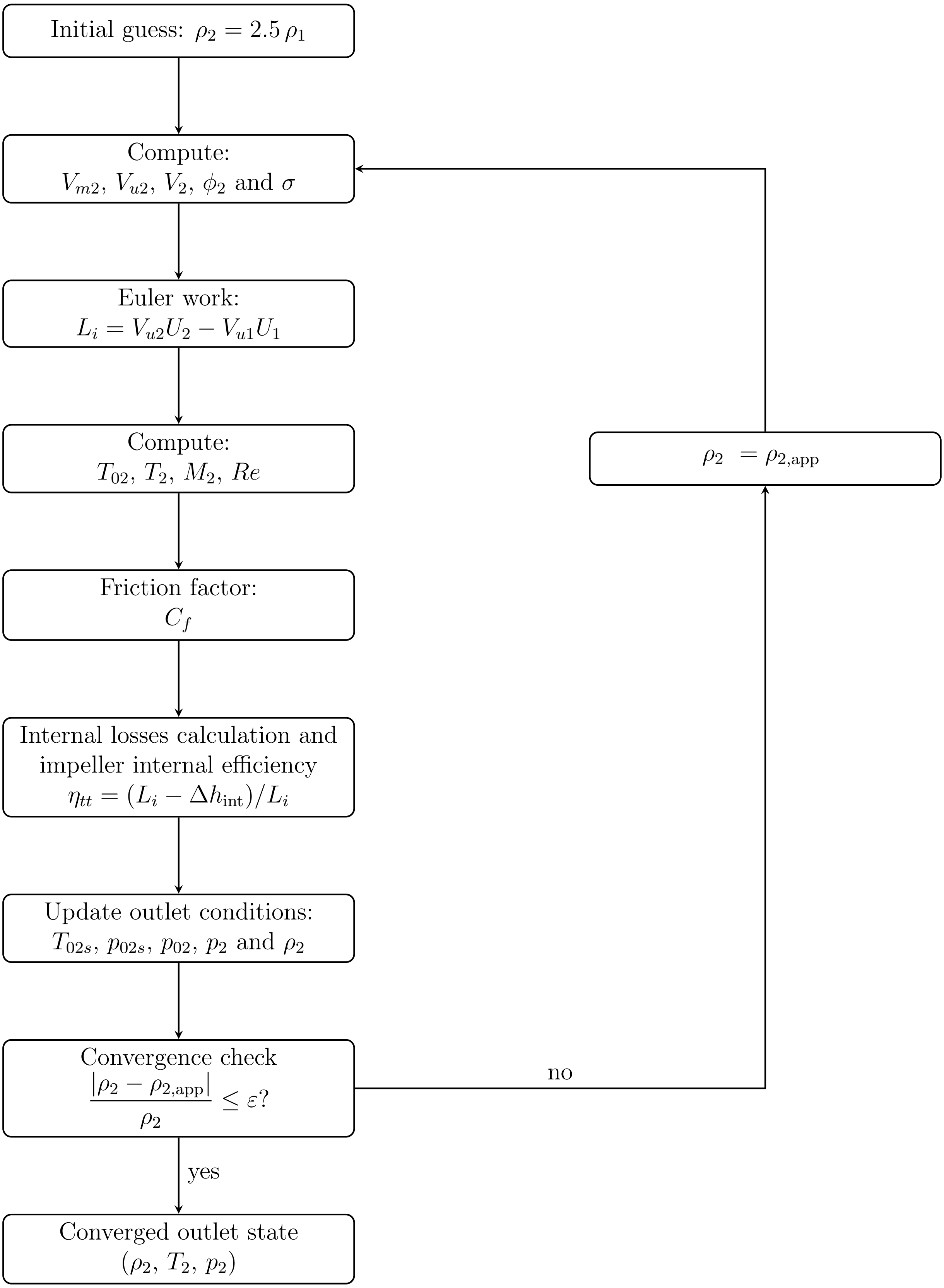

Figure 4.3: Iterative loop for impeller outlet conditions

The internal losses are calculated through a dedicated function, `'calculate_internal_losses.m'`. The parasitic losses are computed outside the iterative cycle, after getting the outlet values: the choice is justified by the fact that they don't affect the pressure ratio characterizing the impeller. They have a role in the definition of the impeller efficiency. A similar code is developed to manage the parasitic losses, called `'calculate_external_losses.m'`.

Finally, several parameters defining the impeller performance are calculated and returned to `'perfcalc.m'`. Velocities, thermodynamic properties and performance data are saved in separated structure: `'imp_perf.m'`, `'imp_terdat.m'`, `'imp_trveldat.m'` and`'imp_loss.m'`.

`'calculate_internal_losses.m'`

This code manages the internal losses taking place in the impeller: according to the loss model set by the user (defined in the input files), the proper formulation to evaluate each loss mechanism is selected. The code is composed by a main function, which compute the internal losses as a summation of the different losses, and a set of subfunction to singularly manage the loss mechanisms. The loss correlation to be used is selected according to the `method_vector.m` created in `'read_check_convert.m'`.

The formulations are provided in chapter 3; an overview is here proposed:

Table 4.2: Internal losses, available correlations, and activation IDs.

Loss	**Available correlation**	**ID**
Incidence loss (incloss)	No loss	0
	Conrad (1980)	1
	Aungier (1995)	2
	Aungier+	3
	Galvas (NASA)	4
	Meroni–Oh	5
	Gravdahl (control theory)	6
Blade loading loss (bldloss)	No loss	0
	Coppage (1956)	1
	Aungier (1995)	2
	Meroni–Oh	5
Hub-to-shroud loss (h2sloss)	No loss	0
	Aungier (1995)	1
Skin-friction loss (skfloss)	No loss	0
	Coppage (1956)	1
	Jansen (1966)	2
	Aungier (1995)	3
	Meroni–Oh	5
Clearance loss (cleloss)	No loss	0
	Rodgers (1968)	1
	Krylov–Spunde (1967)	2
	Aungier (1995)	4
	Jansen	5
	Brasz	6
Entrance diffusion loss (edfloss)	No loss	0
	Aungier (1995)	1
Distortion loss (disloss)	No loss	0
	Aungier (1995)	1
Mixing loss (mixloss)	No loss	0
	Aungier (1995)	1
	Johnston–Dean simplified	2
	Johnston–Dean (iterative)	3
	Denton (DACC)	4
	Meroni–Oh	5
Choking loss (chkloss)	No loss	0
	Aungier (1995)	1
Shock loss (nswloss)	No loss	0
	Aungier (disabled)	1
	Whitfield–Baines	2
Supercritical Mach loss (sma)	Not implemented	0

`'calculate_external_losses.m'`

`calculate_external_losses.m` is structured in the same way as the previous code. The external loss formulations have been precisely described in chapter 3; an overview of the losses is proposed:

Table 4.3: Parasitic losses: available correlations and activation IDs.

Parasitic Loss	**Available correlation**	**ID**
Recirculation loss (extrcloss)	No loss	0
	Aungier (1995)	1
	Oh–Yoon–Chung (1997)	2
	Coppage (1956)	3
	Galvas (NASA TN D-7487)	4
	Rodgers	5
	Alekseev correlation	6
Leakage loss (extlkloss)	No leakage	0
	Aungier — unshrouded impellers	1
	Aungier — shrouded impellers	2
	Aungier (by Zhang [19])	6
	Jansen	7
	Osnaghi	8
Disk friction loss (extdfloss)	No loss	0
	Daily & Nece	1
	Shepherd	2
	Aungier (1995)	3
	Coppage	4
	Daily–Nece (modified)	5
	Galvas	6
	Boyce	7

4.3.2 `diffcalc.m`

The function `diffcalc.m` computes the thermodynamic and aerodynamic performance of the vaneless diffuser located downstream of the impeller exit. It receives as input the thermodynamic and velocity data from impeller exit, the diffuser geometry, and a set of modelling options defined through the input and settings structures.
The function produces the flow properties at station 4 (diffuser outlet), together with performance indicators such as pressure coefficient, diffusion coefficient, total-pressure loss coefficient and diffuser efficiencies.
Two models are proposed to manage the diffuser system:

- Meroni's model;
- Stanitz's model.

Meroni's model

Similarly to `impecalc.m`, this function elaborate a two-level iterative procedure performed to reach the convergence between an estimate and a computed outlet density. This main loop presents two inner iterative procedure aiming to reach, respectively, the convergence of the Reynolds number and the isentropic density. This approach has been inspired by the Meroni model, described in [15]

The Reynolds number iteration starts by the computation of the diffuser friction coefficient C_f, necessary to calculate the tangential component of the absolute velocity at diffuser outlet section.

$$C_f = 0.0058 \left(\frac{1.8 \cdot 10^5}{Re_{\text{dif}}} \right)^{0.2} \tag{4.2}$$

$$V_{4m} = \frac{V_{3u}}{\dfrac{R_4}{R_3} + \dfrac{2\pi \, C_f \, \rho_3 \, V_{3u} \, (R_4^2 - R_3 R_4)}{m_d}} \tag{4.3}$$

The mass flow rate and the supposed density allows the computation of the outle meridional component of the absolute velocity V_{m4}.
Thanks to these parameters, the Reynolds number can be computed and compared to the guessed value:

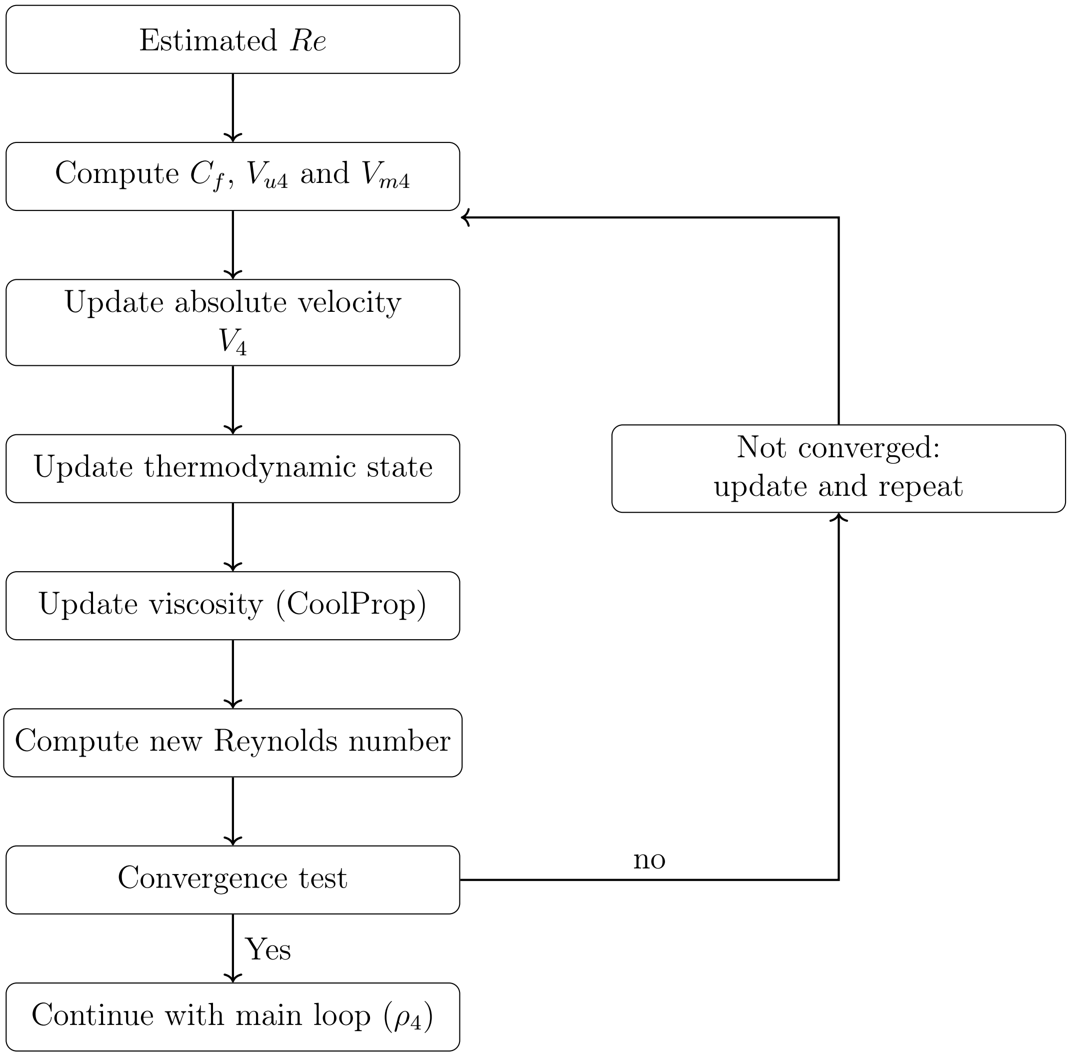

Figure 4.4: Reynolds-number convergence loop

The Reynolds number obtained is used to evaluate the skin friction loss, as defined in section 3.3. The loss value allows to define the total enthalpy, total temperature and total pressure in isentropic conditions. The isentropic density ρ_{4is} is initially assume to be equal to ρ_4 (the guessed value prior to the main cycle): for this reason the second loop is required. The thermodynamic state is computed in isentropic condition:

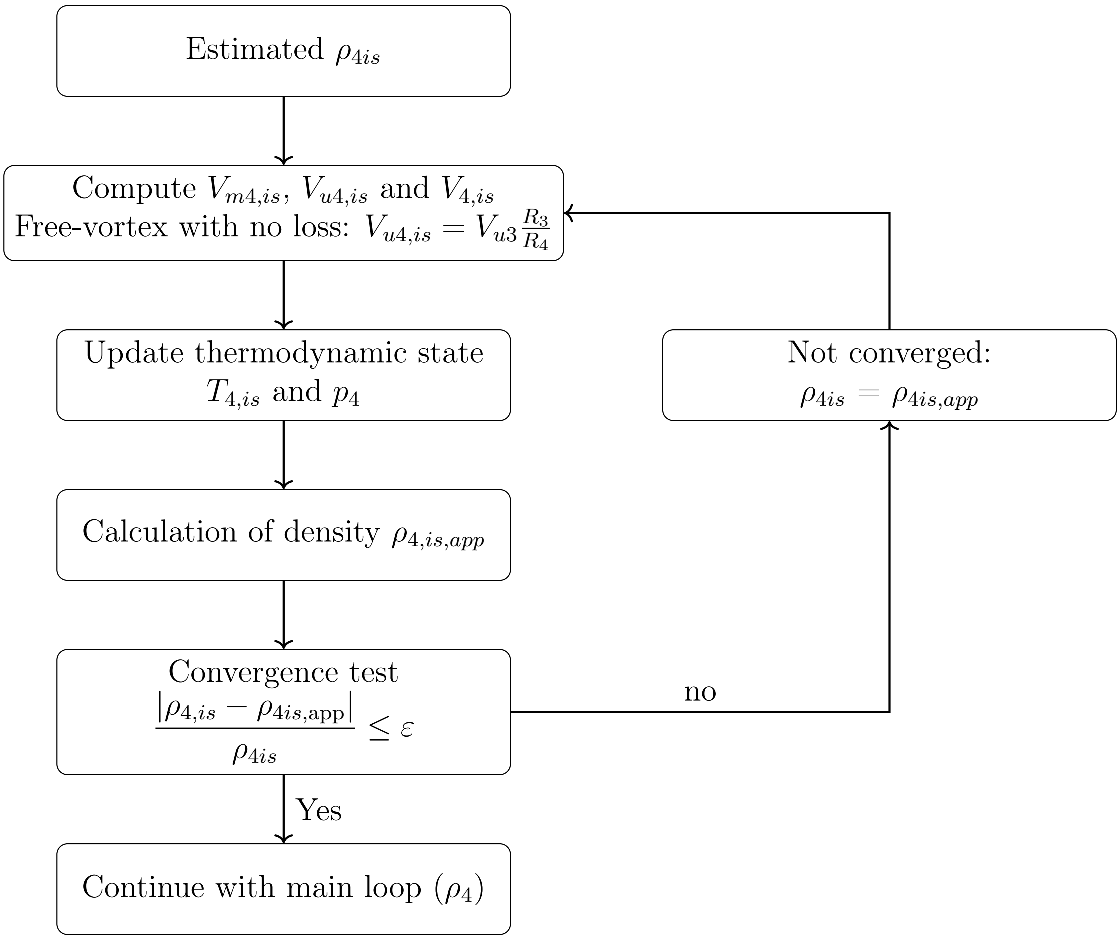

Figure 4.5: Isentropic density convergence cycle

The main loop continues from this second loop: the iterative cycle on the isentropic density provides the proper value of the outlet pressure p_4. The density $\rho_{4,app}$ can be calculated:

$$\rho_{4,app} = \frac{p_4}{RT_4} \tag{4.4}$$

The convergence between the assumed density calculated and guessed is performed:

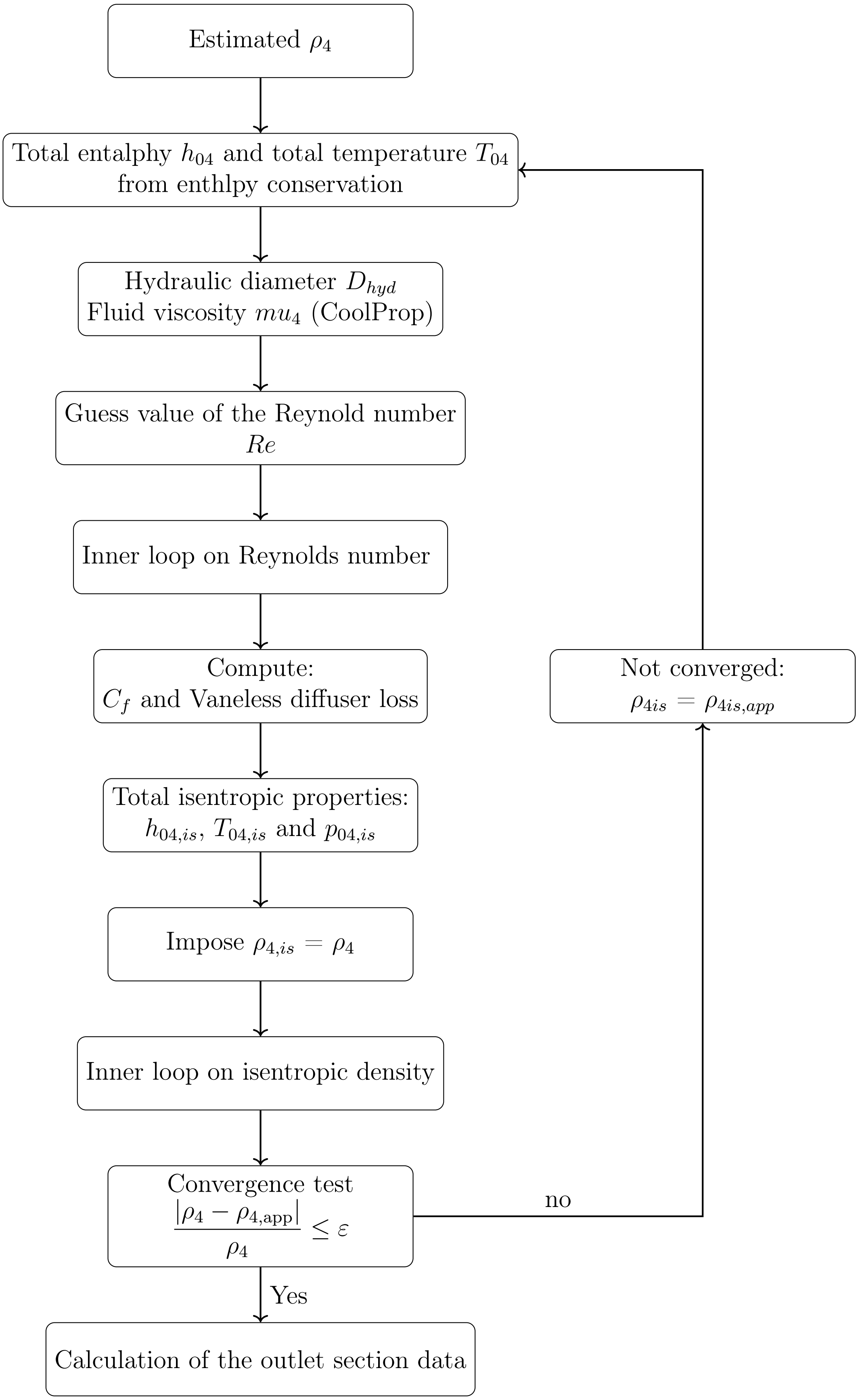
Estimated ρ_4
Total entalphy h_{04} and total temperature T_{04} from enthlpy conservation
Hydraulic diameter D_{hyd}
Fluid viscosity mu_4 (CoolProp)
Guess value of the Reynold number Re
Inner loop on Reynolds number
Compute:
C_f and Vaneless diffuser loss
Total isentropic properties:
$h_{04,is}$, $T_{04,is}$ and $p_{04,is}$
Impose $\rho_{4,is} = \rho_4$
Inner loop on isentropic density
Convergence test
$\frac{|\rho_4 - \rho_{4,\text{app}}|}{\rho_4} \leq \varepsilon$
no
Not converged:
$\rho_{4is} = \rho_{4is,app}$
Yes
Calculation of the outlet section data

Figure 4.6: .

The outlet section data are then calculated and saved in the structures `'diff_perf.m'`, `'diff_terdat.m'` and `'diff_trveldat.m'`.

Stanitz model

The diffuser can be managed in a differt way: it is not modeled through algebraic correlations (as done in Aungier or Meroni's simplified approach), but through the complete 1-D differential formulation originally introduced by Stanitz and later used and reorganized by Meroni. This method solves the evolution of the flow variables inside the vaneless diffuser by integrating a system of differential-algebraic equations (DAEs) using MATLAB's ode15i solver: contrast to correlation-based or semi-empirical approaches, this method integrates a set of differential–algebraic equations (DAEs) along the radial coordinate, providing a physically grounded description of the flow evolution inside the diffuser.

All the geometric quantities (R_3, R_4, b_3, b_4), the inlet thermodynamic state ($p_3, \rho_3, T_{03}, p_{03}$), and the meridional and tangential velocity components (V_{m3}, V_{u3}) are assembled into a structure that is passed to the solver. These inlet values remain "frozen" during the integration and define the initial conditions for the state vector:

$$y(r) = \begin{bmatrix} C_m(r) \\ C_t(r) \\ p(r) \\ \rho(r) \end{bmatrix}, \qquad r \in [R_3, R_4].$$

A friction model of the form

$$C_f = k \left(\frac{1.8 \times 10^5}{Re} \right)^{0.2}, \tag{4.5}$$

is included consistently with Meroni, while the viscosity is computed through a CoolProp `AbstractState` object to account for its dependence on temperature and density.

The diffuser model relies on the Stanitz equations, namely:

- the radial momentum equation;
- the tangential momentum equation;
- the continuity equation including geometric divergence;
- the ideal gas equation of state coupled with total enthalpy conservation.

These equations yield three differential relations and one algebraic constraint, resulting in a DAE system of index 1. The temperature at each radius is obtained from the conservation of total enthalpy:

$$T(r) = \frac{h_0 - C(r)^2/2}{c_p},$$

which introduces thermodynamic coupling between the variables.

The DAE system is integrated with `ode15i`, MATLAB's fully implicit, variable-order and variable-step solver for DAEs. Before the integration, a consistent set of derivatives $\dot{y}_0$ is computed by solving the linearised form of the governing equations at $r = R_3$. This guarantees that the initial state satisfies both the differential and algebraic constraints.

The solver advances from R_3 to R_4, computing the evolution of:

$$C_m(r), \quad C_t(r), \quad p(r), \quad \rho(r),$$

and subsequently:

- velocity magnitude $C(r) = \sqrt{C_m^2 + C_t^2}$,
- temperature $T(r)$, hydraulic diameter $D_h(r)$ and height $b(r)$,
- viscosity, Reynolds number and friction coefficient.

The output is a high-fidelity radial distribution of all the flow quantities within the vaneless diffuser.

The diffuser exit (station 4) corresponds to the last point of the numerical solution:

$$C_{m4},\ C_{t4},\ C_4,\ p_4,\ \rho_4,\ T_4.$$

The total pressure at the outlet is computed using the compressible relation:

$$p_{04} = p_4 \left(1 + \frac{\gamma - 1}{2} M_4^2\right)^{\gamma/(\gamma-1)} \tag{4.6}$$

$$M_4 = \frac{V_4}{a_4}. \tag{4.7}$$

The diffuser losses are evaluated through the Stanitz small-stage formulation depicted in section 3.3.
The outlet parameters are saved as Meroni's model.

This implementation represents the highest-fidelity model available for the vaneless diffuser within the present 1-D MATLAB framework.

Brief overview of the `ode15i` solver

`ode15i` is MATLAB's implicit solver for differential–algebraic equations of index 1. It integrates systems of the form:

$$F(t, y, \dot{y}) = 0,$$

where part of the equations may be algebraic (i.e. do not contain time derivatives).

The solver:

- uses a backward differentiation formula (BDF),
- adjusts the step size and order automatically,
- enforces both the differential and algebraic constraints at every step,
- is particularly robust for stiff or strongly coupled systems.

For these reasons, `ode15i` is the most appropriate tool for solving the Stanitz equations, which combine momentum conservation, thermodynamic constraints and the ideal gas law in an implicit manner.

4.4 `Confronto.m`

All the codes described in the previous sections are functions: they are cited in a code aiming in performing the comparison between the experimental values and the results obtained thanks to the compressor analysis. The data calculated by the MATLAB code are saved in a structure call `PERF1`. A part of the comparing code is dedicated to the extraction of the experimental values, which are saved in a specific folder as tables (files '.mat').

All the plots are managed by this code: the user can easily introduce new plots for a better comparison or to analyse specific data.

4.5 Auxiliary functions

The functions described up to now represents the main structure of the centrifugal compressor analysis. Several other function have been implemented to calculate specific parameters needed in `read_check_convert`, `impecalc` and `diffcalc`. The most important are listed below:

- `terdcalc.m`: performs the calculation of the thermodynamic properties;
- `trvcalc.m`: performs the calculation of the velocity triangles;
- `slipfact.m`: calculates the slip factor;
- `generation_table.m`: generates the files '.mat' containing the experimental values of the centrifugal compressors;
- more additional functions.

4.6 Summary

This chapter has outlined the MATLAB computational framework developed for the 1-D performance prediction of centrifugal compressors. The code architecture is modular, flexible, and suitable for the comparison of different loss models across several compressor families.

Chapter 5

Validation of Loss Models and Predicted Performance

This chapter presents and discusses the results obtained from the one-dimensional performance model developed in this thesis. The analysis focuses on the comparison between numerical predictions and experimental data for the selected centrifugal compressor stages, with particular attention to the predictive capabilities of the different loss correlations and modelling approaches introduced in the previous chapters.

5.1 Loss Models Analysed

Four main set of losses have been used to compute the performances of the centrifugal compressors tested by the code: the first loss model is provided by Meroni et Al. [15] that used the Eckardt impellers to validate their choices in defining the loss formulations. The other three sets are provided by Zhang et Al. [**Zhang**], which were tested on 8 centrifugal compressors. Zhang et al., in particular, proposed a new correlation method based on the inlet tip relative Mach number M_{w2t} and the specific speed n_s; this method allowed to divide and differ the loss correlations used to predict the performance of subsonic and transonic compressors.
Alongside this two loss models, a classical one is presented: Oh et al. proposed a set of losses that, in many cases, provides a proper match between numerical and experimental results. Zhang et al. analysed their set compared to Oh et al. model.
The loss correlations are here presented:

Table 5.1: Comparison of loss models across Meroni, Set 1, Set 2, Set 3, and Oh's Set. [15], [19]

Loss mechanism	**Meroni**	**Set 1**	**Set 2**	**Set 3**	**Oh's Set**
Internal losses					
Skin friction	Galvas / Aungier	Jansen	Jansen	Jansen	Jansen
Blade loading	Jansen	Coppage	Coppage	Aungier	Coppage
Mixing	Johnston and Dean	Aungier	Johnston and Dean	Aungier	Johnston and Dean
Clearance	Coppage / Jansen	Jansen	Jansen	Rodgers	Jansen
Incidence	Galvas	Aungier	Aungier	Aungier	Conrad
Entrance diffusion	–	Aungier	Aungier	Aungier	None
Choke	–	Aungier	Aungier	Aungier	None
Shock	–	None	Whitfield and Baines	Whitfield and Baines	None
External losses					
Disc friction	Japiske / Daily and Nece	Daiy and Nece	Daiy and Nece	Daiy and Nece	Daiy and Nece
Recirculation	Oh	Coppage	Coppage	Coppage	Oh
Leakage	–	Aungier	Aungier	Jansen	Aungier

It's necessary to specify that the mixing loss, in Meroni's model, is accounted as an **external loss**. Three main groups of compressors have been have been analysed to validate the MATLAB code and to evaluate the loss models:

- *Eckardt impellers* [19];
- *eight centrifugal compressors used by Zhang to validate the set of losses* [19].

The test-cases are analysed one by one in the following paragraphs.

5.2 Eckardt impellers

The first group of compressors analysed in this project is composed by the Eckardt impellers. Commonly used in literature to validate the loss correlations discovered since the second half of the 1900s, they represent an optimal starting point to validate the code and to analyse loss models.

Three centrifugal compressor are part of the Eckardt impellers, identified as 'Eckardt impeller O', 'Ekcardt impeller A' and 'Eckardt impeller B'. They show similar geometric parameters and are characterised by a rotor followed by a vaneless diffuser.
Their geometric parameters are reported in the table 5.2:

	Units	**Eckardt Impeller**		
		O	**A**	**B**
Fluid	–	Air	Air	Air
T_{01}	K	288.15	288.15	288.15
p_{01}	bar	1.01	1.01	1.01
N	krpm	14–16	14–16	14–16
Impeller				
r_{1s}	m	0.14	0.14	0.14
r_{1h}	m	0.045	0.06	0.0599
r_2	m	0.2	0.2	0.2
b_2	m	0.026	0.026	0.026
L_z	m	0.13	0.13	0.13
$Z_{r,\text{full}}$	–	20	20	20
$Z_{r,\text{splitter}}$	–	0	0	0
$\text{LR}_{\text{splitter}}$	–	0	0	0
β_{1bs}	°	–63	–63	–60
β_{1bh}	°	–32	–40	–45
β_{2b}	°	0	–30	–40
ϵ_a	mm	0.372	0.235	0.372
ϵ_r	mm	0.372	0.19	0.372
ϵ_b	mm	0.372	0.235	0.372
k_s	mm	0.002	0.002	0.002
b_1	mm	2.11	2.11	2.11
b_2	mm	1.08	1.08	1.08
Vaneless Diffuser				
r_3/r_2	–	1.69	2.69	3.69
b_3/b_2	–	0.51	0.51	0.51

Table 5.2: Data of experimental Eckardt compressors [15]

The only differences highlighted for the three impellers are the inlet radius at the shroud, the blades' angles (changing both at the inlet and at the outlet) and the clearances. The diffusers, instead, shows different geometry: the outlet radius R_3 becomes bigger and bigger as it move from O impeller to B.
Each impeller is analysed.

5.2.1 Eckardt Impeller O

The first impeller to be analysed is Eckardt O. The experimental values to which the compare is performed are reported in tables 5.3: the isentropic efficiency η_{tt} and the pressure ratio PR_{tt} have been calculated for four different rotational speed of the impeller. According to the results reported in the table, the higher rotational speed shows the highest values of pressure ratio; instead, in terms of efficiency, the performance shows almost constant values for all the velocities investigated, with values range between 85-90%.

Table 5.3: Performance data O: mass flow rate, pressure ratio, isentropic efficiency and rotational speed (from [15])

$\dot{m}$	PR_{tt}	η_{tt}	**rpm**
2.3043	1.46224	0.84135	10000
2.5418	1.47712	0.85035	10000
2.7543	1.48284	0.86017	10000
3.0266	1.49199	0.87162	10000
3.2769	1.49657	0.87857	10000
3.5428	1.49771	0.88264	10000
3.7838	1.49542	0.88344	10000
4.0323	1.49085	0.88219	10000
4.2733	1.48284	0.87971	10000
4.5949	1.47368	0.87641	10000
3.0806	1.70938	0.84662	12000
3.4116	1.72998	0.85806	12000
3.7094	1.75515	0.86706	12000
3.9789	1.76316	0.88015	12000
4.2541	1.76316	0.88586	12000
4.5253	1.76087	0.88584	12000
4.7726	1.75744	0.88418	12000
4.9671	1.75057	0.88171	12000
5.1448	1.74256	0.87841	12000
5.3300	1.73227	0.87512	12000
3.9469	2.04805	0.85146	14000
4.2227	2.06293	0.85882	14000
4.5346	2.08124	0.86904	14000
4.8231	2.08810	0.87557	14000
5.0322	2.09153	0.88088	14000
5.2824	2.09611	0.88537	14000
5.5739	2.09039	0.88412	14000
5.7516	2.08352	0.88041	14000
5.9636	2.07437	0.87384	14000
6.1093	2.06293	0.86809	14000
4.9387	2.49657	0.85589	16000
5.2395	2.51487	0.86119	16000
5.4566	2.52288	0.86527	16000
5.6895	2.53204	0.86935	16000
5.9334	2.53204	0.87261	16000
6.1424	2.52517	0.87382	16000
6.4246	2.51144	0.87257	16000
6.6354	2.50229	0.87050	16000
6.8206	2.48856	0.86721	16000
6.9948	2.47025	0.86351	16000

The analysis of the impeller under investigation has been performed using the loss model provided by Meroni et al. in their review [15]; they didn't include all the loss mechanism reported in chapter 3. In those cases, the loss has been set

to zero and doesn't affect the performance of the compressor.
The results obtained shows an optimal correlation between numerical data and experimental ones.

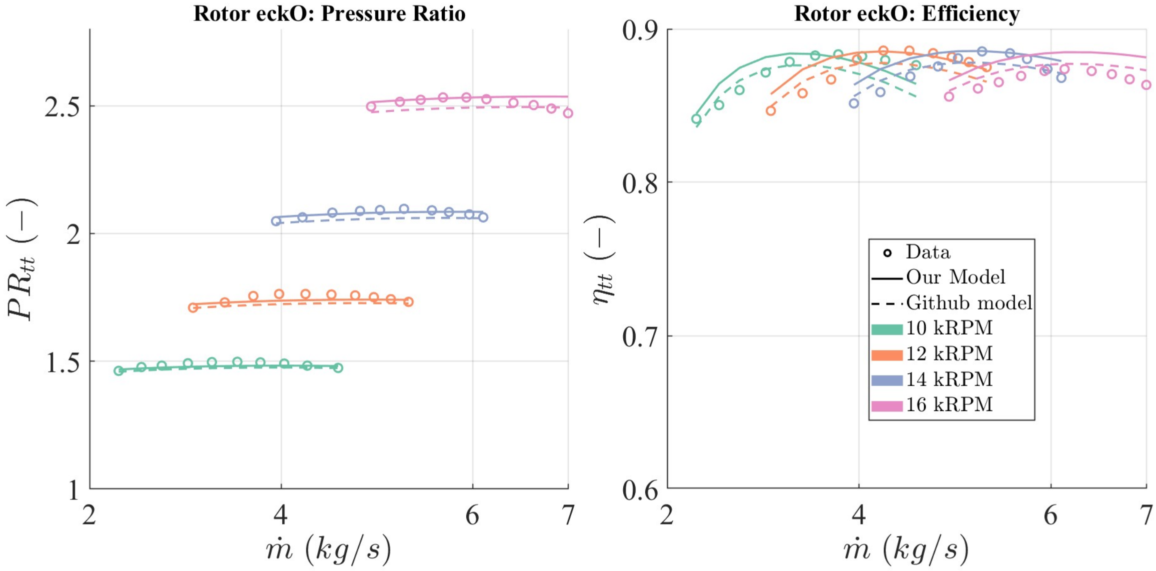

Figure 5.1: Isentropic efficiency and pressure ratio for Eckardt O

The dashed curve represent the performance estimation obtained with a code similar to the one described in the thesis. The results achieved are quite satisfactory, with an almost proper overlap of the data.
Meroni's model is compared to Set 1 and Set 3 provided by Zhang:

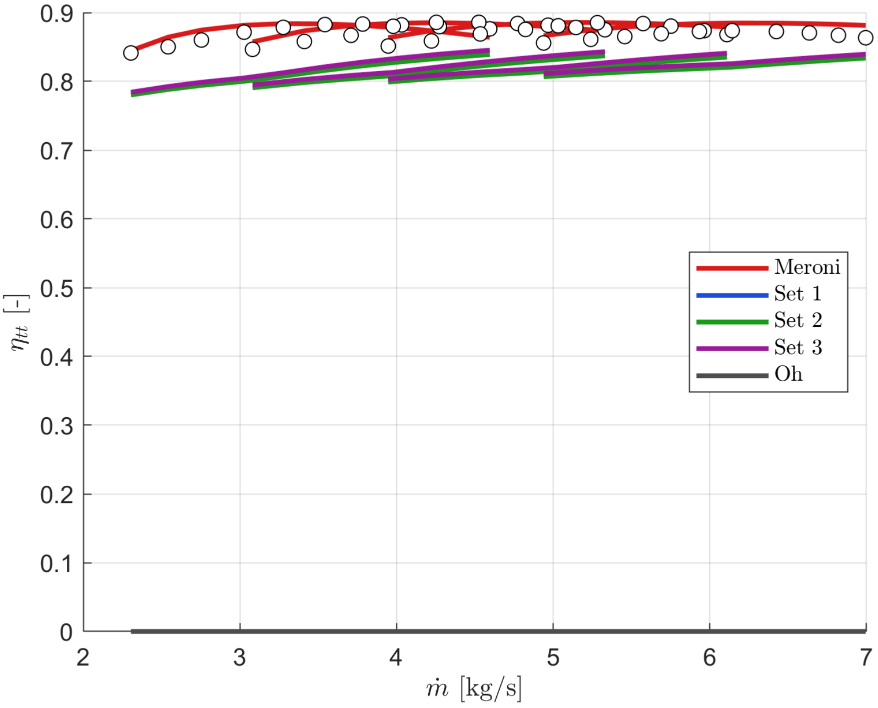

Figure 5.2: Results compared between Meroni, Set 1 and Set 3

Even if Set 1 and Set 3 of Zhang are not directly determined on Eckardt rotors, they show a good approximation of the experimental data: the maximum error observed is estimated at 6%. The pressure ratio shows even greater approximations:

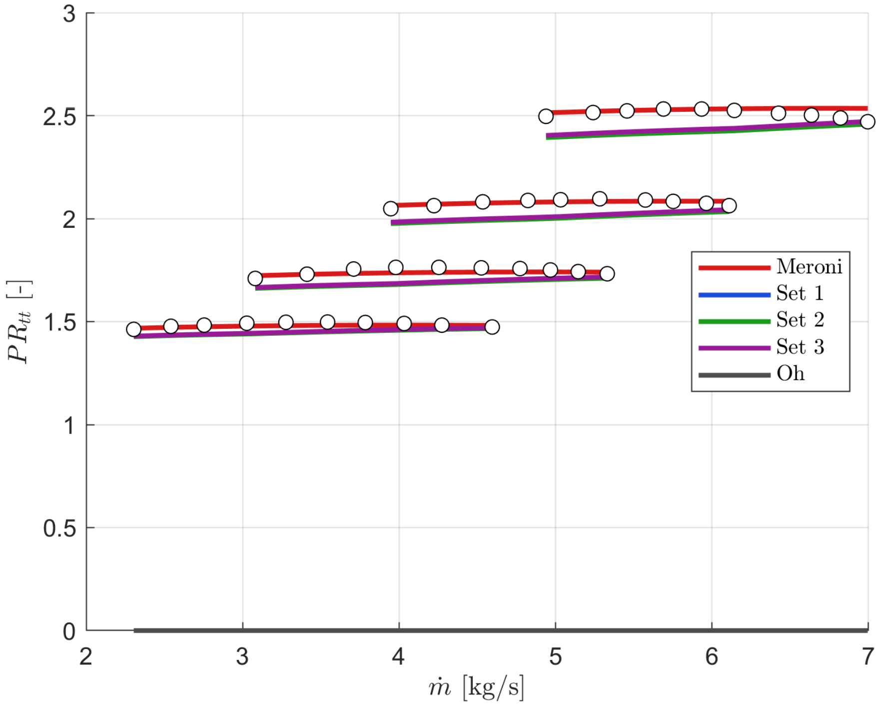

Figure 5.3: Pressure ratio: Meroni model, Set 1 and Set 3

The lower performance of Zhang's models is explained also by the higher number of internal loss mechanism considered and that directly impact the efficiency calculations.

The internal loss, for this reason, the internal losses produced with Set 1 and 3 are higher. Interesting is the weight that different loss mechanism have in defining the overall internal loss:

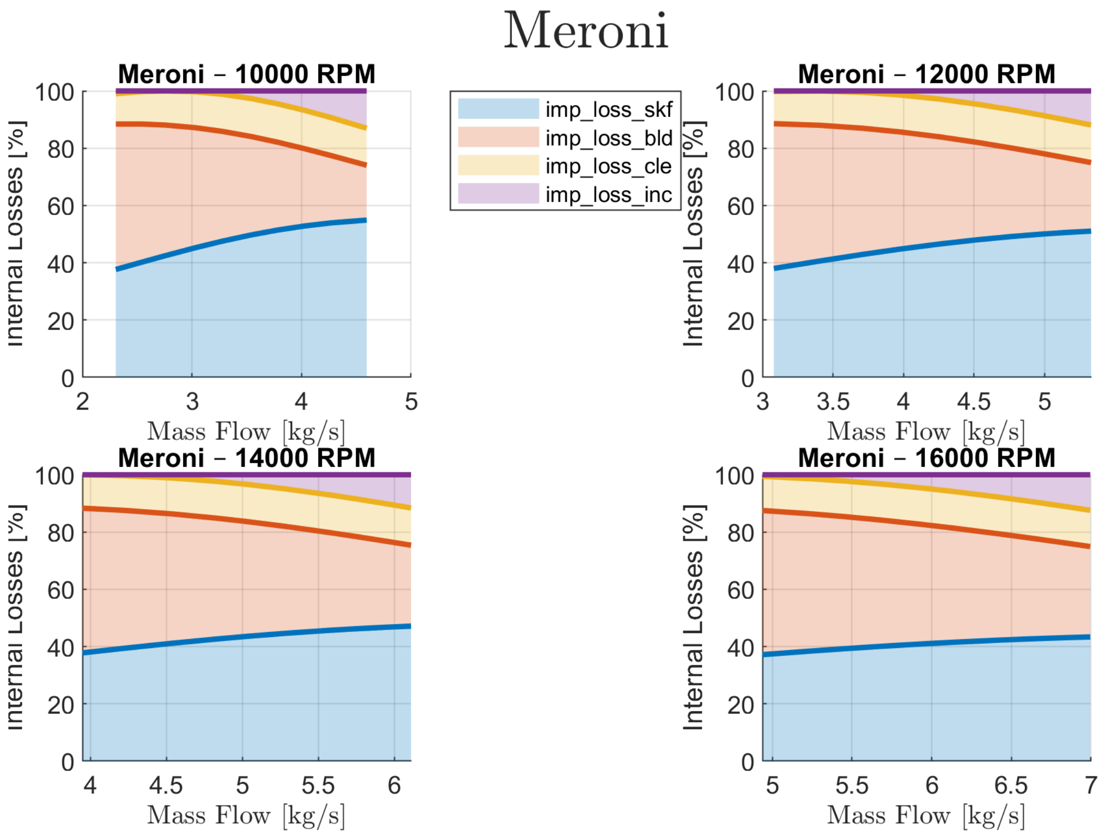

Figure 5.4: Loss mechanism weight on the overall internal loss, Meroni

According to Meroni's formulation, the loss mechanism that most impact on the performance of the compressor is the skin friction loss. Similar impact is performed by the blade loading loss. As the mass flow rate increases, the two losses behave the opposite way: the blade loading loss decreases while the skin friction effect rises up. The clearance loss is basically constant; incidence becomes a factor only at high mass flow rates.

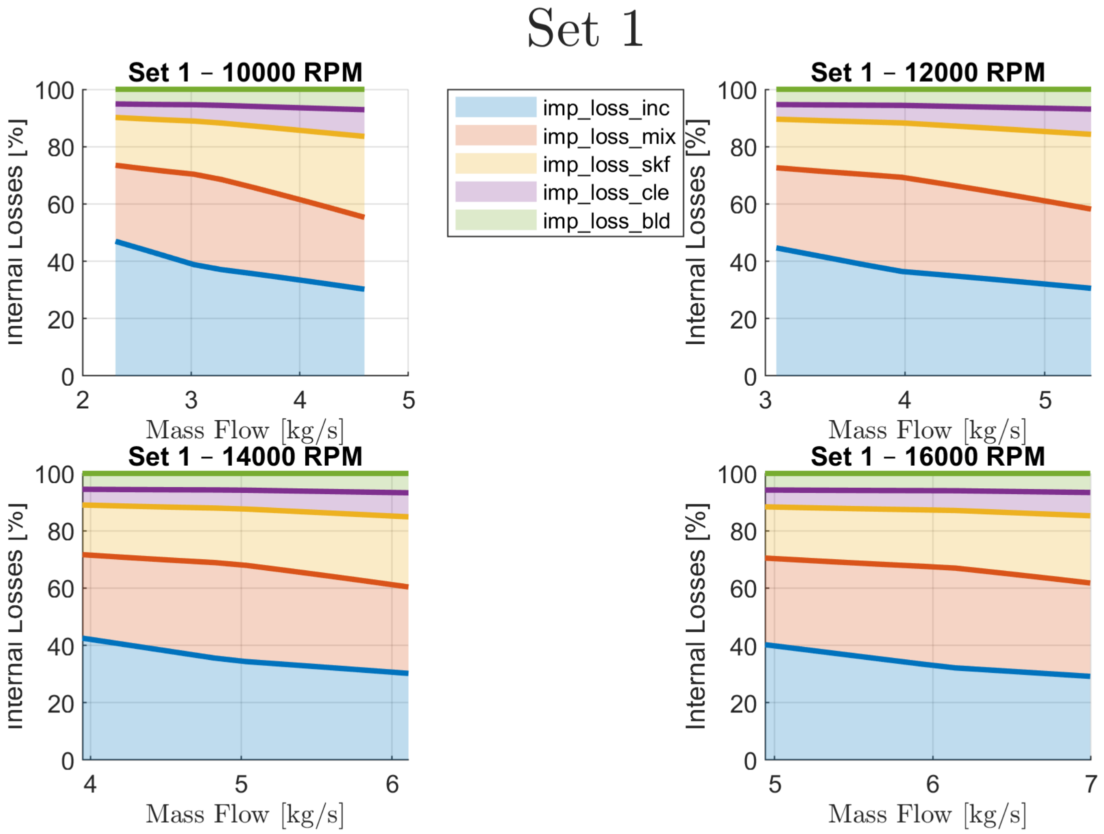

Figure 5.5: Loss mechanism distribution according to Set 1

The cumulative diagram represented for Set 1 shows a different state: incidence loss becomes the dominant mechanism of entropy gain. Mixing loss, that in Meroni is set as an external loss, provides an additional contribution in reducing the efficiency. Blade loading loss and clearance provide constantly the 15% of the loss.

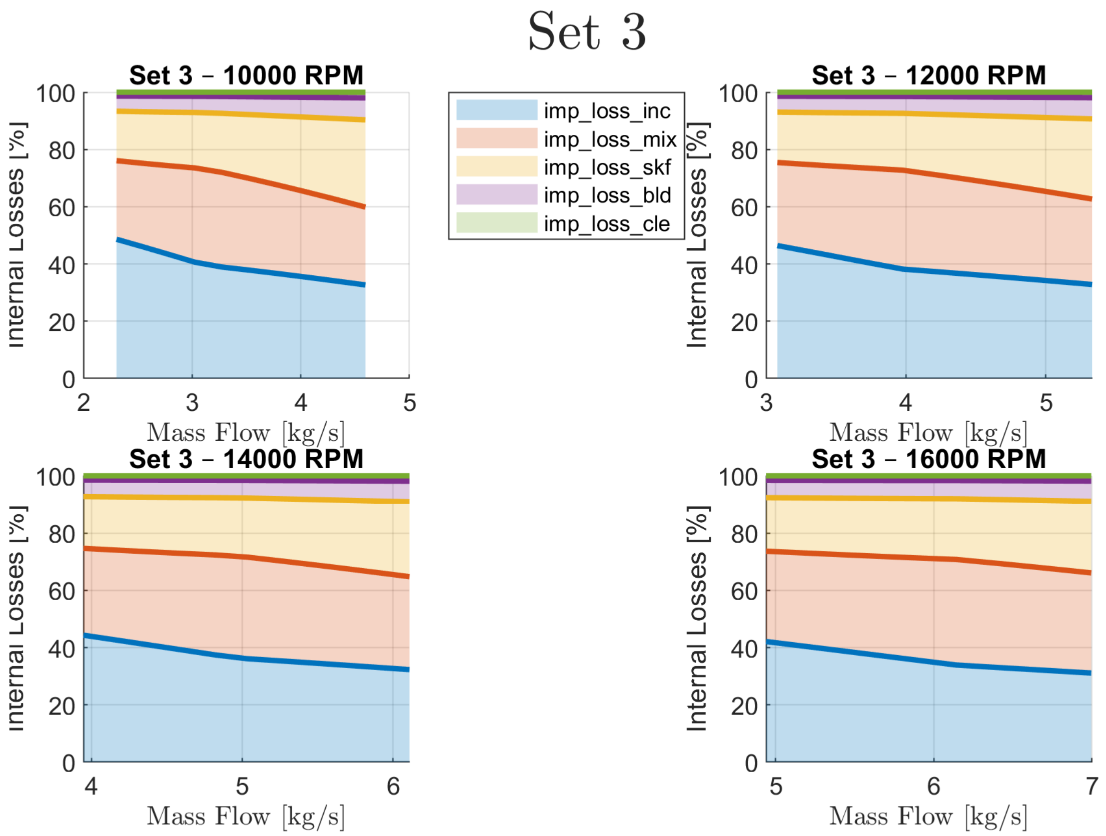

Figure 5.6: Cumulative losses in set 3

Set 3 behaves similarly to Set 1: the cumulative plots don't highlight much difference. Blade loading and clearance swap their percentages.

Finally, the diffuser performance is evaluated: no experimental data are provided. The main parameters are computed and compared to the reference code.

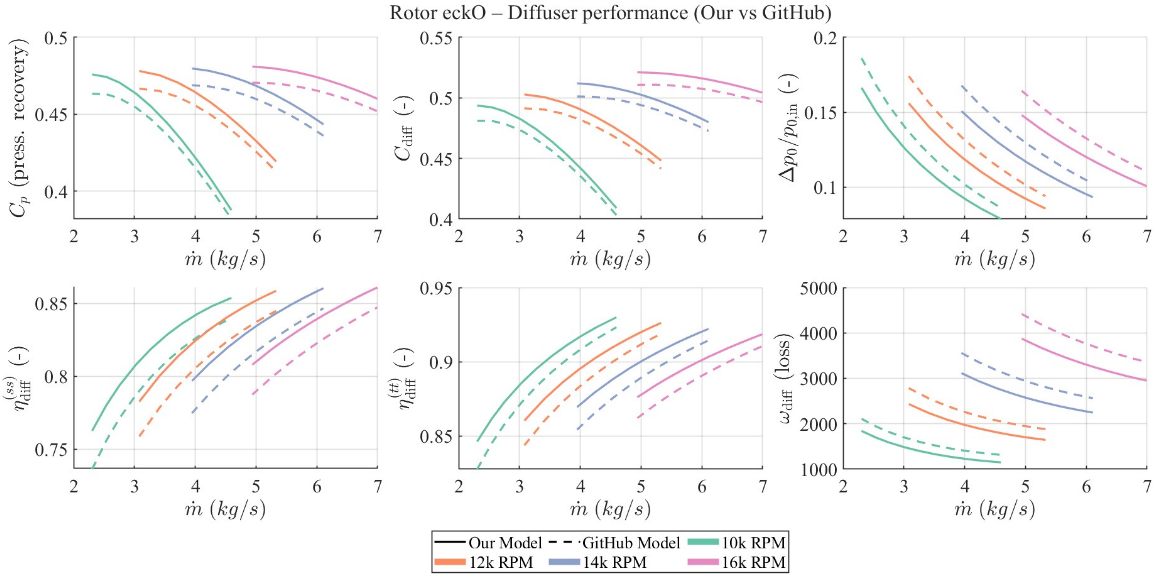

Figure 5.7: Diffuser performance parameters

All the graphs show a constant discrepancy between the GitHub model and the MATLAB code, describing a better perfomance predicted by MATLAb.

5.2.2 Eckardt Impeller A

The second impeller analysed by the Meroni et al. is the Eckardt impeller A: the experimental are:

Table 5.4: Performance data A: mass flow rate, pressure ratio, efficiency, and rotational speed (from [15])

m_dot	**pr_tt**	**eta_is_tt**	**rpm**
2.5099	1.42146	0.89138	10000
3.1043	1.40996	0.89918	10000
3.8211	1.38506	0.89220	10000
4.5962	1.34674	0.86263	10000
5.0361	1.32184	0.82854	10000
3.0198	1.64751	0.88809	12000
3.8765	1.62452	0.89671	12000
4.4971	1.59387	0.88522	12000
5.2925	1.54406	0.86140	12000
5.9860	1.47126	0.80390	12000
3.5239	1.94253	0.86797	14000
4.5553	1.91379	0.88563	14000
5.3391	1.86398	0.87536	14000
6.1026	1.78161	0.84743	14000
6.7960	1.63027	0.75421	14000
4.2261	2.30460	0.85770	16000
5.3333	2.27586	0.87536	16000
6.1229	2.20881	0.86756	16000
6.9096	2.05747	0.82074	16000
7.1923	1.92912	0.76324	16000

The impeller has geometrical parameters similar to Eckardt impeller O: the main differenced are related to the inlet shroud radius, which is increase for A impeller, the clearance gaps, a little bit reduce, and the change of the blade profile. In fact, at the outlet impeller section, impeller O is defined by a blade having outlet angle β_{2b} directed entirely in radial position: in case A, instead, the blade is deviated from the radial direction. Moreover, the inlet radius of the diffuser is scaled differently to the outlet cross section.

The impeller is evaluated by the MATLAb code following Meroni's loss correlations. The overall performance are available in fig. 5.8:

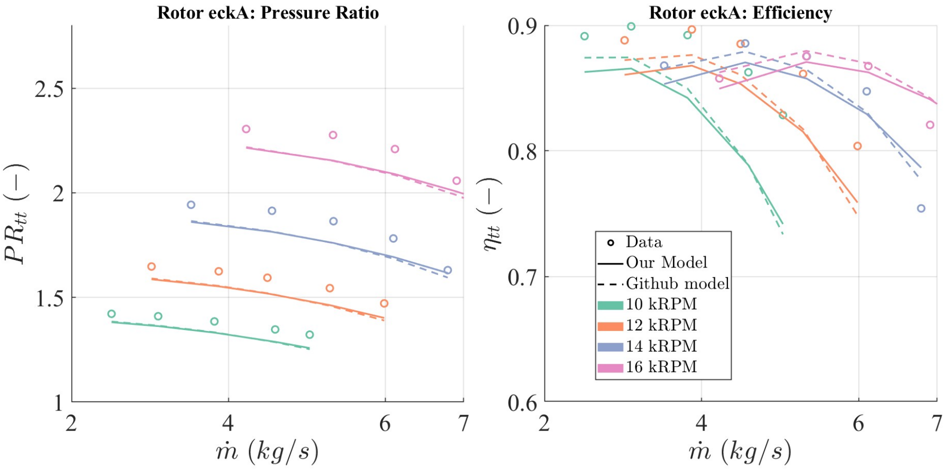

Figure 5.8: Isentropic efficiency and pressure ratio of Eckardt A compared to experimental data

The model evaluated through the Matlab code has not the same accuracy appreciated for impeller A: the efficiency and the pressure ratio overestimates the real losses occurring in the turbomachine, sketching lower values than the experimental ones. Similarly to the description done for the previous compressor, Set 1 and Set 3 are use to highlight the performance trend with different loss models.

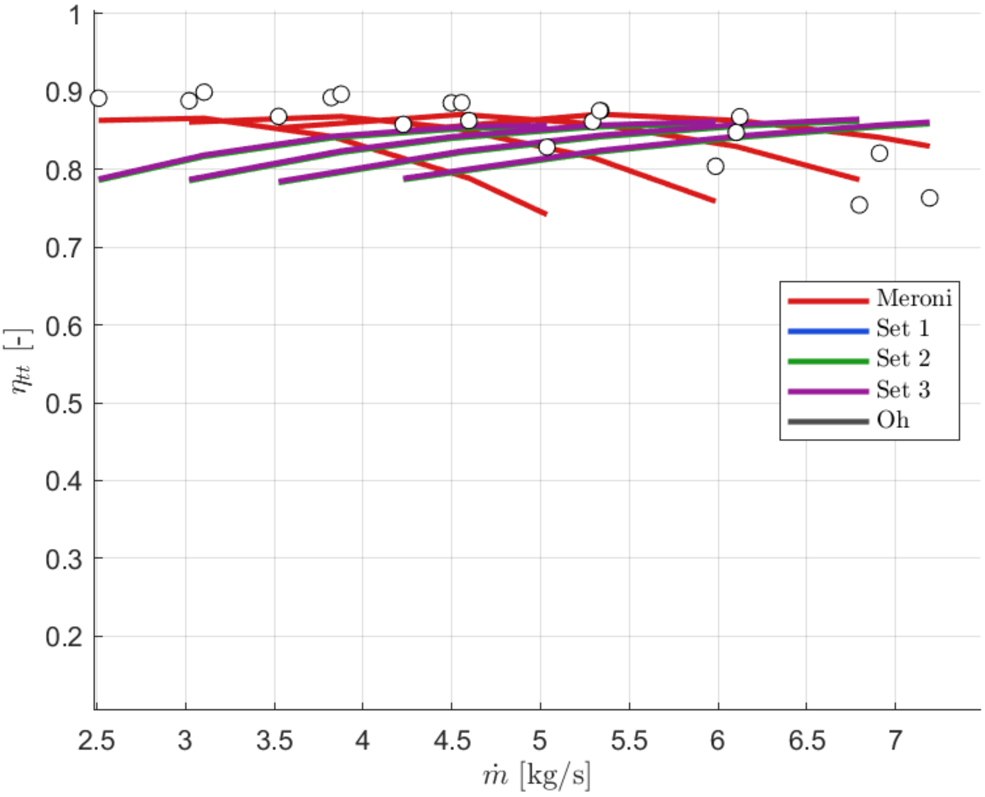

Figure 5.9: Comparison between different loss models

Like the previous case, Meroni loss model performs better: the difference in terms of efficiency is 5% but in particular cases, like for low values of mass flow rates, the discrepancy increases.

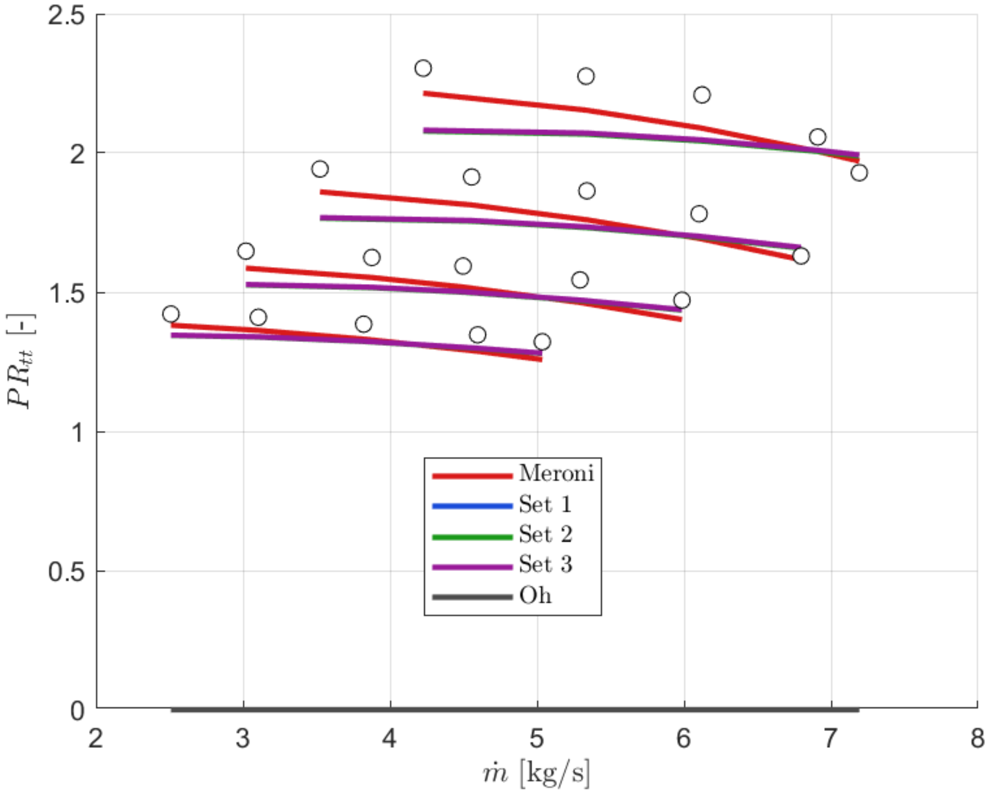

Figure 5.10: Pressure ratio: Meroni, Set 1 and Set 3

Pressure ratio in fig. 5.10 suggests that the value obtained for lower values of rpm is similar; a gao is obtained at higher rotational speed of the compressor. The differences in pressure ratio between experimental and numerical values reaches the maximum gap when $rpm = 16000$ at $\dot{m} = 0.2$.

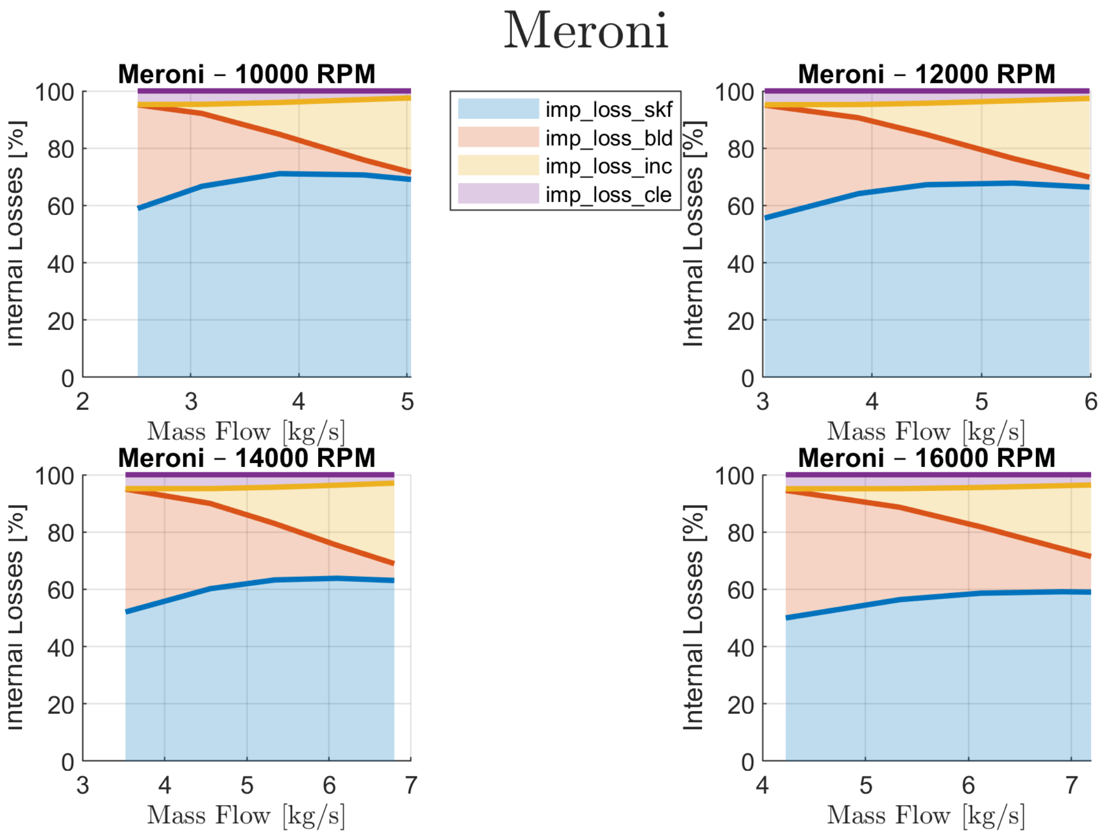

Figure 5.11: Meroni cumulative loss correlations

The blade loading loss massively reduces as the mass flot rate increases: skin friction dominates again the internal losses. Set 1 and Set 2 behaves like described in **??**.

The diffuser performance is again compared to the reference model: the discrepancies rises up, achieving two different behaviours.

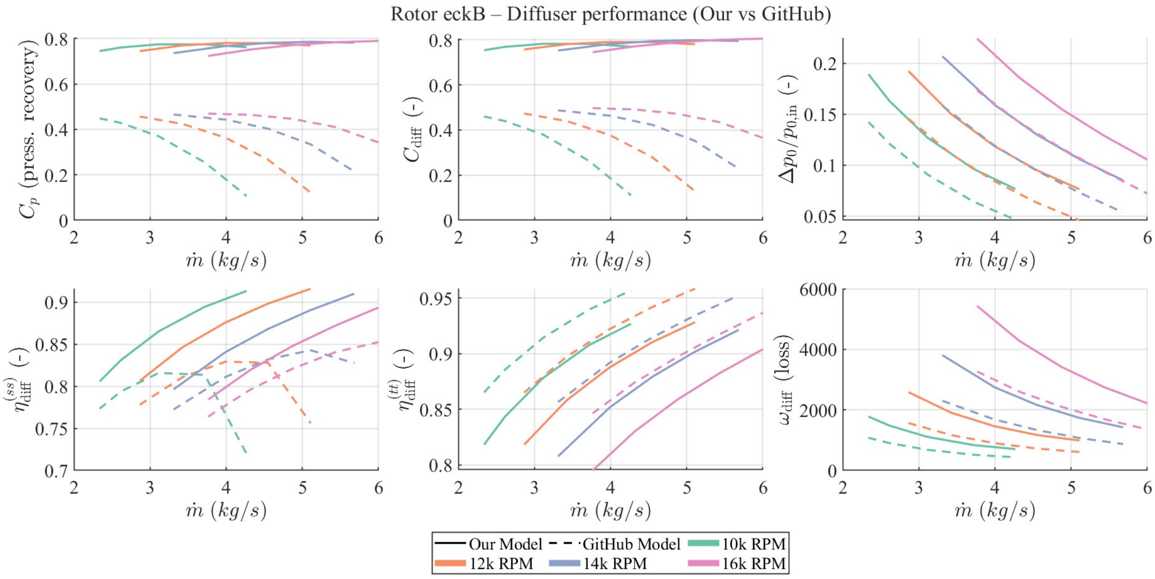

Figure 5.12: Diffuser Performance A: Matlab code vs GitHub model

The gap already seen in fig. 5.7 are even more accentuated; the major deflections are obtained for the first two parameters: the pressure recovery coefficient C_p and the diffusion coefficient C_{diff} have completely different behaviour. The code suggests almost constant terms, while the reference model shows a slowly decrease of the factors.
The external losses are for entirely generated by mixing phenomena: only at low values of mass flow rate, recirculation has a role.

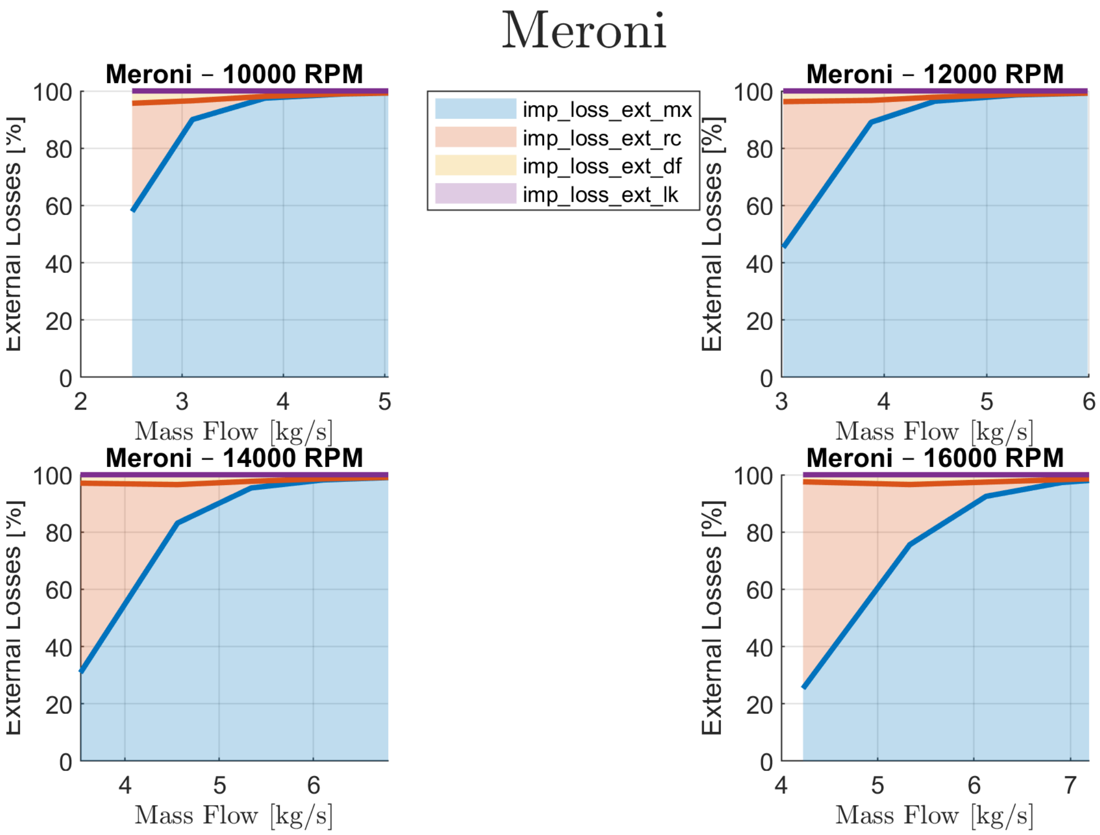

Figure 5.13: Meroni cumulative parasitic losses

The external losses in Set 1 and Set 3, instead, mainly generate by leakage phenomena.

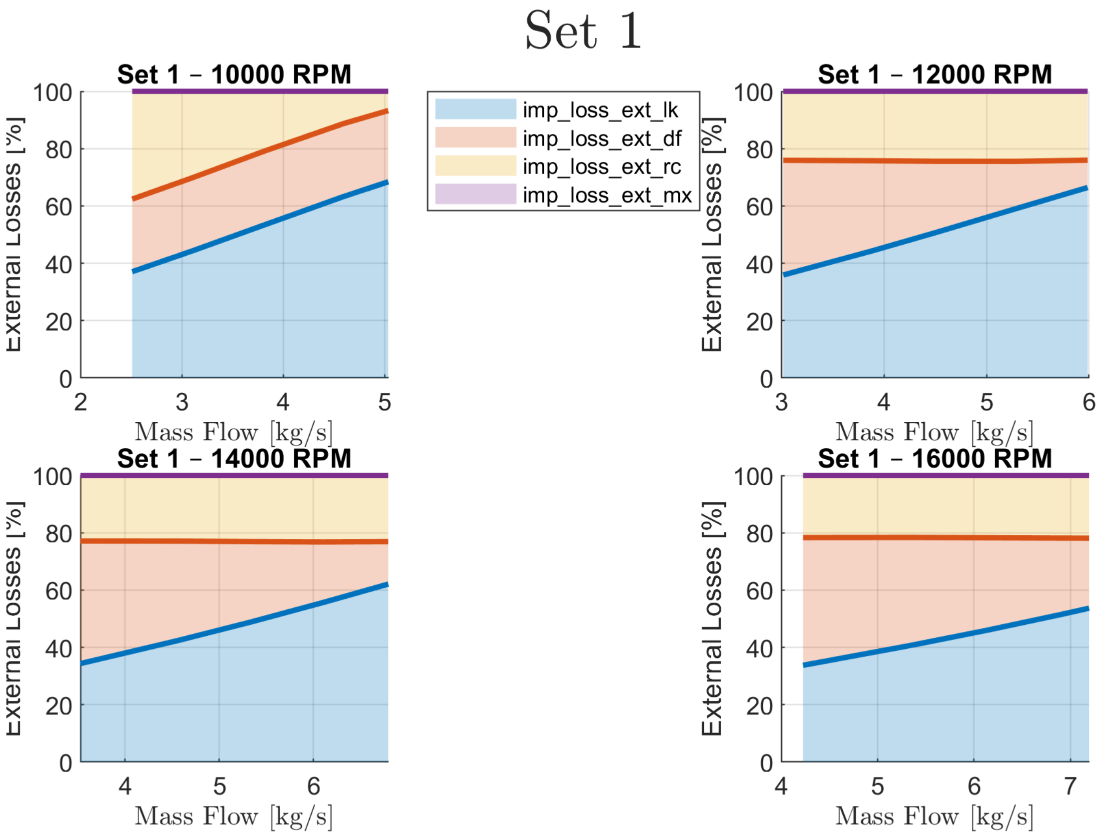

Figure 5.14: Set 1 cumulative parasitic loss correlations

5.2.3 Eckardt Impeller B

Eckardt impeller B is slightly bigger than the rotor A described in the previous section. Considering the inlet radius at the shroud, R_{1shr} is more than doubled compared to impeller O. The outlet blade angle is way deflected and the diffuser radius is way bigger (up to three times, according to 5.2.
The experimental values are [15]:

Table 5.5: Performance data: mass flow rate, pressure ratio, efficiency, and rotational speed

m_dot	**pr_tt**	**eta_is_tt**	**rpm**
2.33846	1.34243	0.84804	10000
2.61421	1.33926	0.86582	10000
3.11506	1.32058	0.88489	10000
3.71930	1.28799	0.88156	10000
4.26956	1.24152	0.83467	10000
2.86563	1.51202	0.84174	12000
3.42587	1.50413	0.87054	12000
3.98883	1.47309	0.87989	12000
4.54850	1.42971	0.87063	12000
5.11030	1.34312	0.80303	12000
3.30977	1.73565	0.83078	14000
3.99150	1.72772	0.86298	14000
4.55157	1.69668	0.87529	14000
5.11122	1.63633	0.86434	14000
5.68405	1.43245	0.74219	14000
3.76573	2.01483	0.81687	16000
4.31997	2.01157	0.84059	16000
4.87712	1.99134	0.85798	16000
5.43697	1.93715	0.86014	16000
6.00264	1.52648	0.65596	16000

The results obtained are here reported:

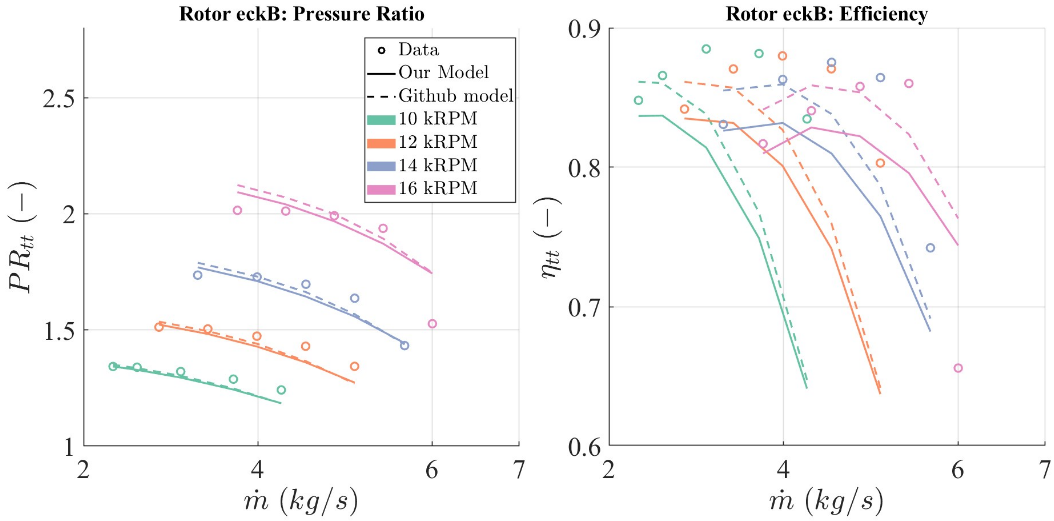

Figure 5.15: Performance estimation with Meroni's model for Eckardt impeller B

The pressure ratio is almost equal to the experimental models: only at highest speed the curvature is not properly intersect. In terms of efficiency, the numerical solution moves fare from the experimental values. The curves have an offset with

respect to the experimental values: the orange one, for example, results moved to the left by a difference of $1\frac{kg}{s}$.
The compare with Set 1 and Set 3 is here reported:

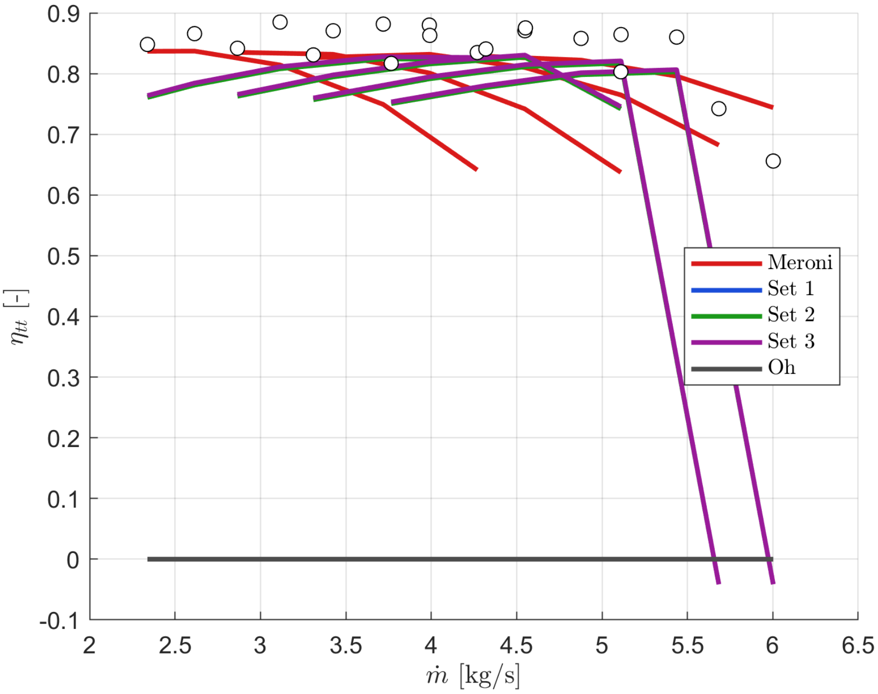

Figure 5.16: Set 1 - Set 3 - Meroni; isentropic efficiency

Set 3 reaches the choking conditions: the mass flow rate is 'freeze' and the performance drops. Overall, the efficiencies found with Set 1 and Set 3 shows a good approximation, if related to the numerical value. The gap between the experimental values and the computed ones reaches 10%. The pressure ratio doesn't seem much affected by this behaviour. Set 3, in particular, shows better results in terms of pressure ratio, achieving a better interpolation of the experimental point.

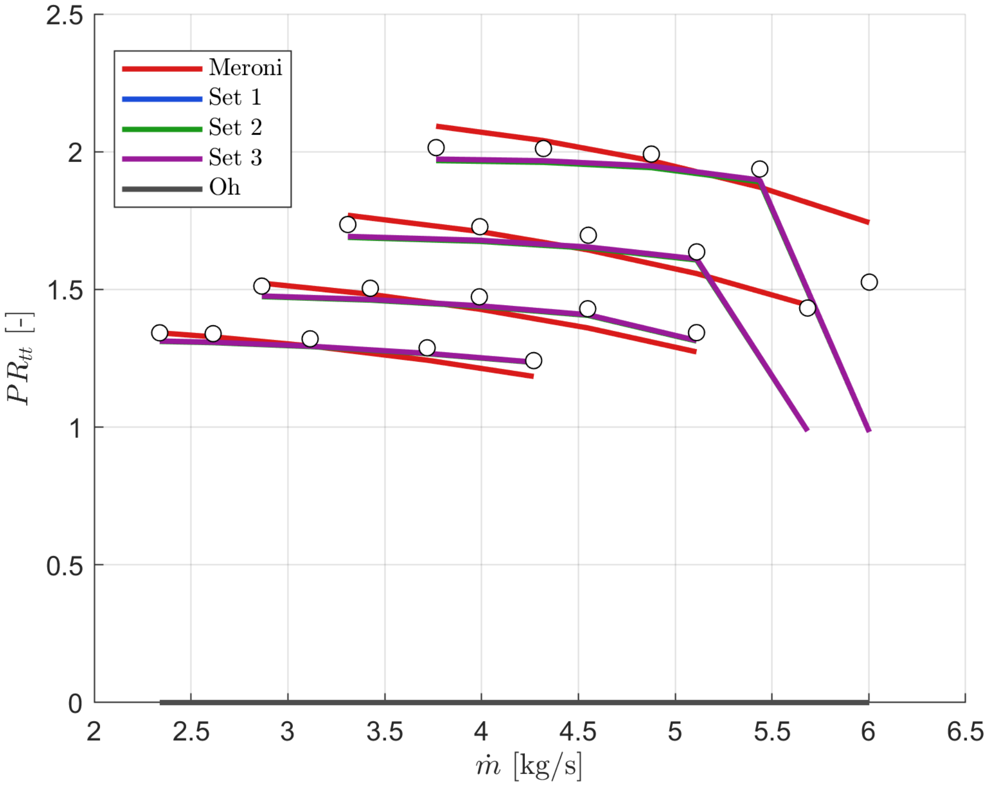

Figure 5.17: Set 1: matching with experimental pressure ratio

5.3 8 Zhang Compressors

Zhang, Dong, Liu, Sun, Wu, Gao and Tan [19] have proposed in the recent years (2019) three new set of loss correlations to compute the performance of a centrifugal compressor following a mono dimensional analysis. They defined the three new set, called $Set1$, $Set2$ and $Set3$ according to the inlet tip relative Mach number and the specific speed. Their method have been validated by experimental results on eight centrifugal compressors. They performed the comparison with Oh's set to highlight an improvement in performance computation.

5.3.1 Mixing model

The three set used to calculate the efficiency and the pressure ratio have been already reported in table 5.1. A few lines should be dedicated to describe changes or adjustments performed to develop the Zhang et al. method and to compute the performance of the compressors under test.

The researchers described in great detail all the formulation used in this paper; only the mixing loss, described by Johnston and Dean, wasn't explicitly expressed.
As already discussed in chapter 3, Johnston and Dean describes the mixing loss by means of the jet-wake flow pattern: the wake is the low momentum fluid, bringing all the losses, while jet represents the portion of the fluid moving at high

speed. The mixing between this two regions produces a loss: in many documents, the mixing is described to take place a little further the outlet cross section of the impeller. Anyway, regardless of where the mixing happens, the mixing loss is usually considered an internal loss: actually it is generated from the phenomena taking place inside the impeller passage.

Johnston and Dean rely on an iterative cycle to compute the mixing loss: starting from a two-zone model, the width of the wake is computed. The width is one of the terms composing the loss formulation. Then, an iterative cycle is performed to check the convergence between the static pressure computed with two-zone model and static pressure obtained from 1-D performance analysis.

Two-zone model has been computed following exactly the same passage reported in [27] by oh et Al. The author follows three iterative procedure to define wake zone, jet zone and mixing zone. Oh follows this path starting from a calculated outlet pressure p_2. The last loop cycle is performed on the computation of the total temperature: when the total temperature T_{02} converge criterion is satisfied, the code exits from the loop and the outlet conditions of the impeller are obtained. These ones will represent the inlet condition of the following diffuser.
Oh, to compute the total temperature T_{02}, uses the parasitic losses: since `impecalc` computes the the iterative cycle to compute the outlet conditions and the parasitic losses are then calculated, this passage performed by oh has been removed: the converge criterion is applied between the estimated static pressure p_2 obtained from 1-D and the static pressure obtained by Oh. A loop is created starting from the value of χ, the wake mass fraction, and all the equations for jet, wake and mixing zone are put together. If the converge is not reached, the value to be change is chi (by performing the 'relaxation'.

Mixing represents a key loss in the impeller: a proper definition of the loss correlation allows to improve the impeller performance and directly affect the following components.

5.3.2 Test Cases

The geometry of the ehight compressors is directly provided by Zhang et al in their paper [19]:

Depending on the values of the inlet tip relative Mach number:

$$M_{w1t} = \frac{W_{1t}}{\sqrt{\gamma R_g T_1}} \tag{5.1}$$

and of the specific speed:

$$n_s = \frac{2\pi n}{60} \frac{Q_1^{0.5}}{(\Delta h_{0s})^{0.75}} \tag{5.2}$$

the eight compressors have been divided in three classes:

Table 5.6: Design parameters of eight centrifugal compressors.

Impeller	**A**	**B**	**C**	**D**	**E**	**F**	**G**	**H**
Inlet hub diameter d_{1h}/mm	90	60	63.96	45	90	90	20	44.6
Inlet tip diameter d_{1t}/mm	225.5	156	112.5	95.3	280	280	61	97.2
Inlet hub blade angle β_{1h}/deg	31.4	53.9	62.2	34.2	32	32	31	46.6
Inlet tip blade angle β_{1t}/deg	63.3	62.3	62.2	56.3	63	63	40	61.5
Exit diameter d_2/mm	400	224	208	207.4	400	400	90	163.4
Exit blade width b_2/mm	14.71	10.2	7.57	7.5	26	26	6.5	4.90
Exit blade angle β_{2b}/deg	30	38	30.2	30	30	30	30	34
Impeller axial length L_z/mm	119.84	75.15	57.5	130	130	130	32	47.32
Exit blade number Z_2	24	13+13	18+18	12	20	20	7+7	19
Mass flow rate m/kg s^{-1}	4	2	0.3	0.9	5.32	4.54	0.35	0.98
Rotational speed/rpm	22363	50000	45337	15000	14000	14000	80000	68384
Pressure ratio	4.07	6.1	5.5	1.18	2.1	1.91	2.24	7.1
Isentropic efficiency/%	84.56	84.25	91.30	88.15	88.15	88.14	79.00	89.50
Tip clearance size/mm	0.2	0.3	0.174	0.2	0.525	0.525	0.27	0.191
Exit vaneless diffuser diameter d_3/mm	560	358.4	232	370	680	680	148	–
Inlet tip relative Mach number M_{w1t}	0.92	1.3	0.87	0.26	0.65	0.64	0.83	1.25
Specific speed n_s	0.531	0.812	0.463	0.603	0.723	0.748	0.988	0.636
Specific diameter d_s	4.397	3.266	5.011	4.561	3.104	3.236	2.787	3.945

- group 1: are the compressors that are in subsonic conditions. Take part of this class the compressors **D**, **E** and **F**;
- group 2: are the compressors in transonic conditions and with $n_s < 0.7$, like compressors **A**, **C** and **H**;
- group 3: are those with $n_s > 0.7$ and transonic conditions, as **B** and **g**.

Each group is characterised by the corresponding set of losses.

5.3.3 Performance analysis

The eight compressors have been tested with the Matlab code to evaluate their performances and to check if they intersect the experimental results.

Few considerations should be taken into account:

- Zhang et al describes their compressor followed by a vaned diffuser; since only the impeller and vaneless diffuser have been developed, the vaned diffuser has not been evaluated;

- some impellers have splitter blades. The simplest way to take them into account is to use the Aungier formula to compute a corrected number of full blades that considers also the impact (in part) of the splitters.

$$Z = Z_{FB} + Z_{SB}\frac{L_{SB}}{L_{FB}} \tag{5.3}$$

- compressors E and F correspond to the Eckardt impellers evaluated in the previous section with Meroni: for this reason, they will not be described again;
- a coefficient has been introduce to properly manage the choking of the impeller: by increasing-decreasing this parameter, the choke can be anticipated or retarded to meet with the experimental parameters. Aungier itself, in [6], suggest to use a coefficient to scale the choking conditions.

SET 1

The only device evaluated with set 1 is the the compressor D. The experimental values of efficiency were not provided:

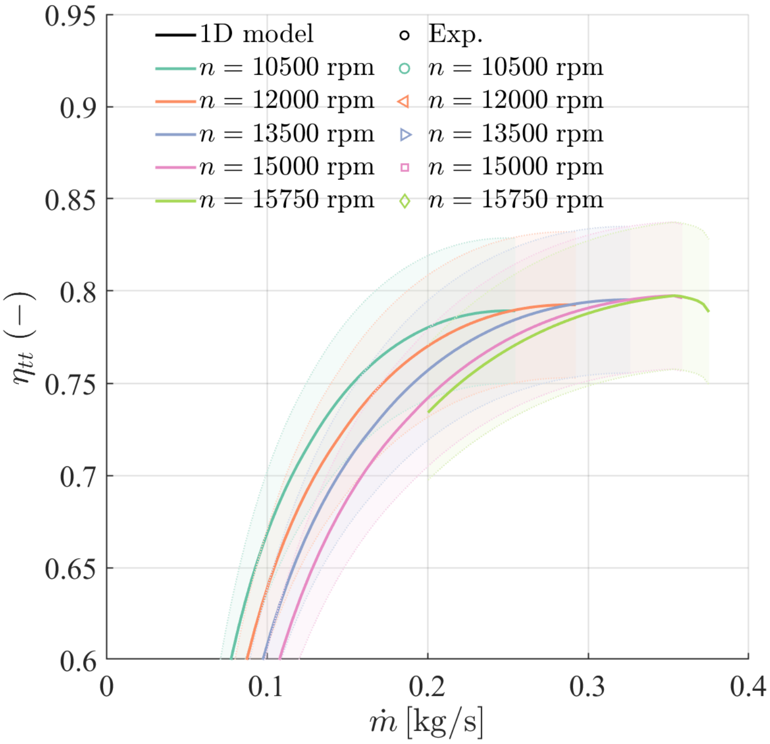

Figure 5.18: Isentropic efficiency of compressor D.

The pressure ratio curves perfectly lie on the experimental point, suggesting a good loss model:

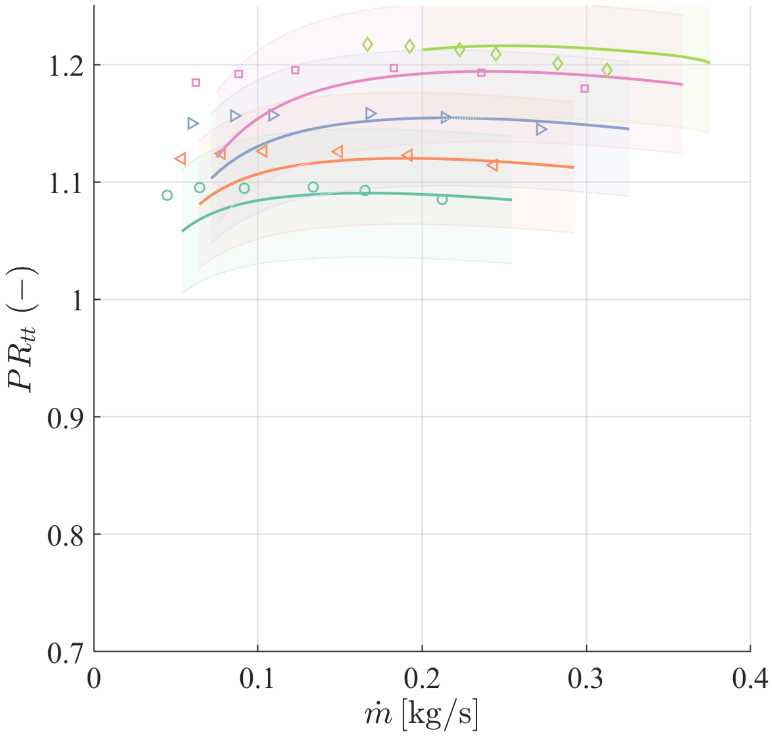

Figure 5.19: Pressure ratio estimation of compressor D

Oh's set show similar performances:

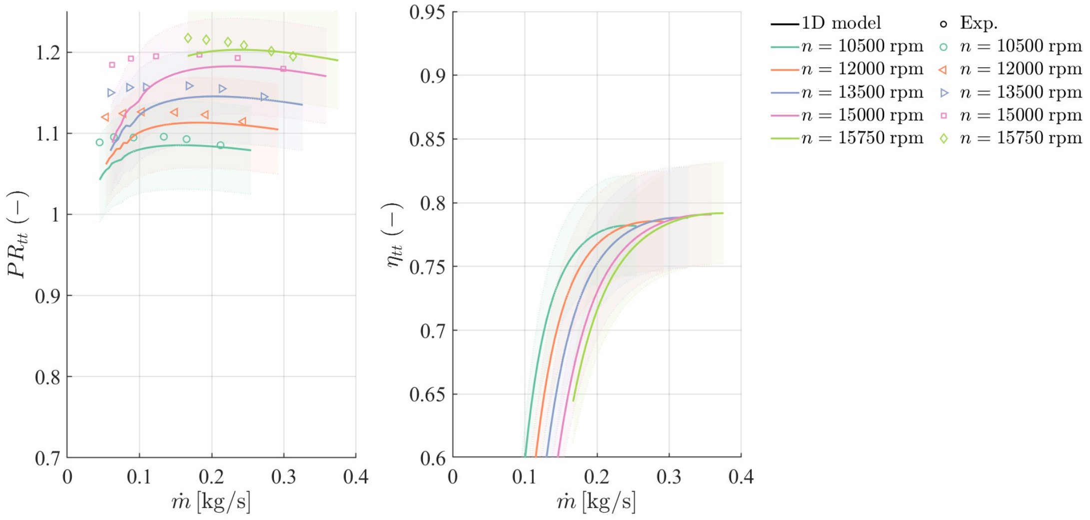

Figure 5.20: Pressure ratio and isentropic efficiency for Oh'set

SET 2

Set 2 is composed by impellers that have reached transonic conditions. Three compressors are evaluated: **A**, **C** and **H**. **C** is the device creating more problems during the computational effort. The performance obtained where far off the experimental results. For these reason, the curves are not reported.

A is the compressor that shows the better interpolation between experimental data and numerical ones. No splitter are considered, so the code is able to provide a proper estimation.

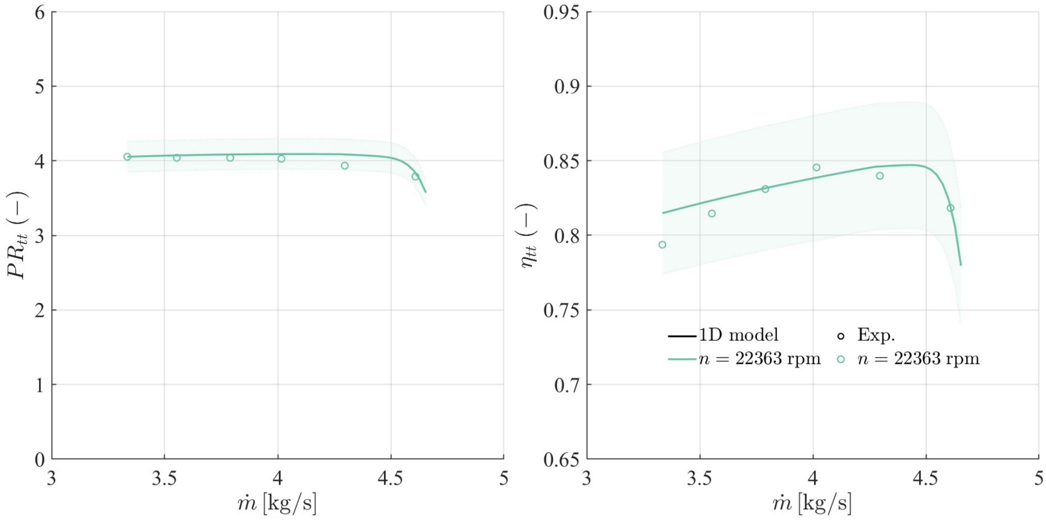

Figure 5.21: A: pressure ratio and isentropic efficiency

From the graph of the internal losses it's possible to see the moment in which the impeller reaches choking conditions: the loss value increases exponentially.

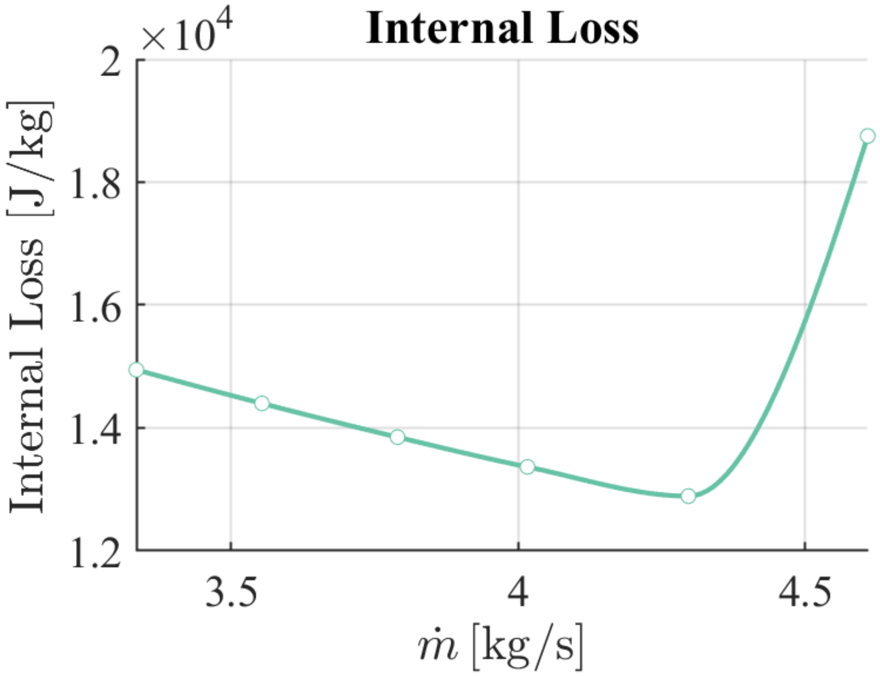

Figure 5.22: Internal losses evolution of compressor A

Oh'set performs in a worst way:

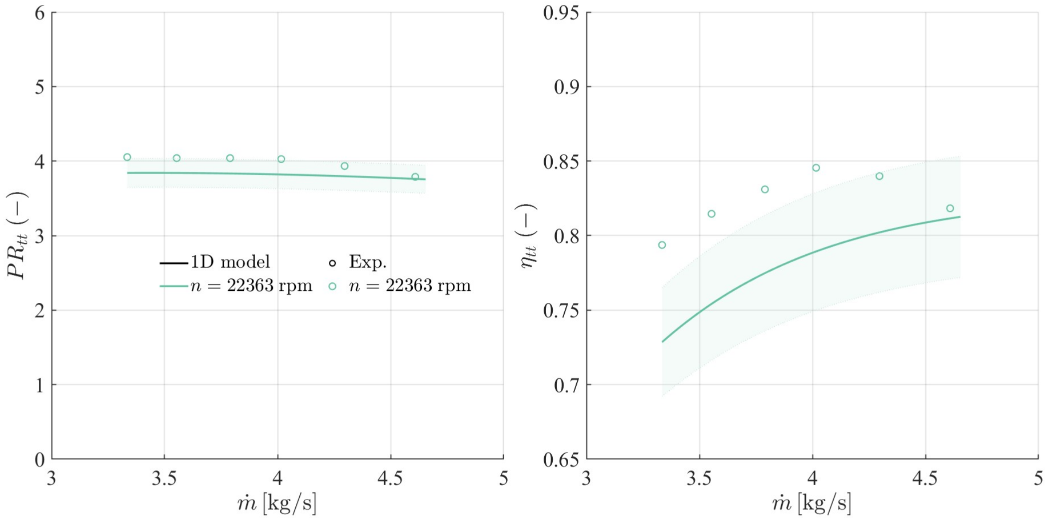

Figure 5.23: Internal losses evolution of compressor A (Oh set)

The other compressor analysed is H which has no vaneless diffuser. The performance obtained are reported below:

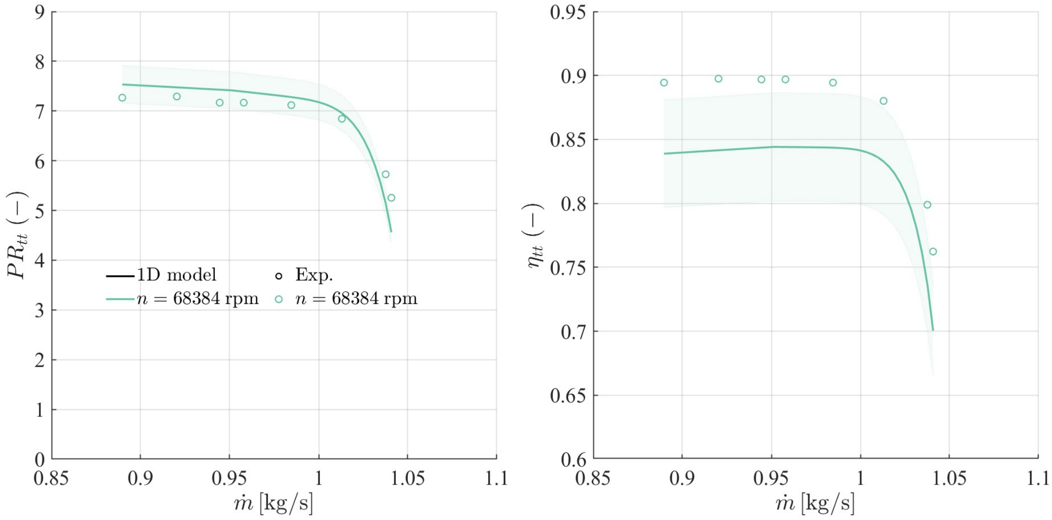

Figure 5.24: Performance estimation of H compressor (Set 2)

H compressor is closed to group 3 since the specific speed is not so distant from the limit. It has sense to evaluate the compressor with Set 3: however, the performances are well below the experimental results.

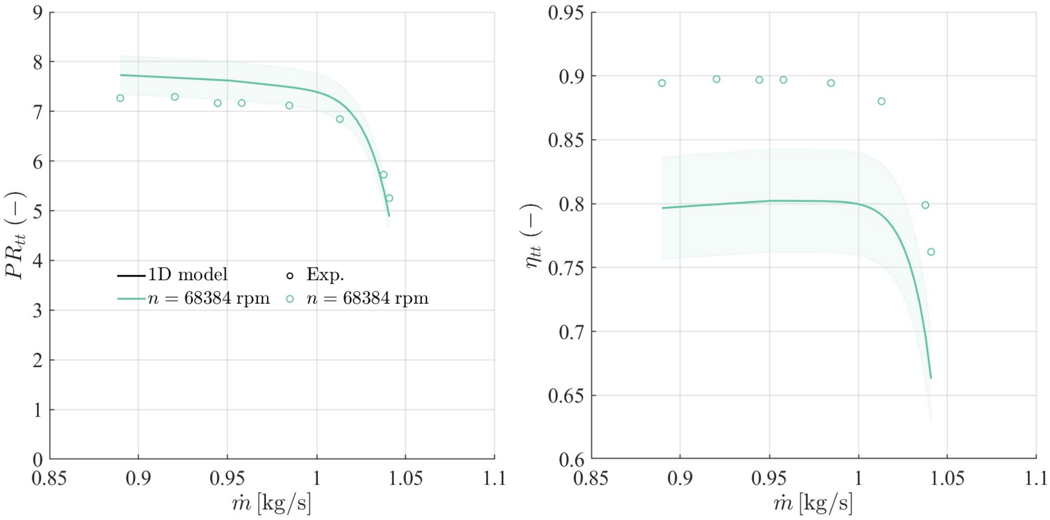

Figure 5.25: Performance estimation of H compressor (Set 3)

Oh set doesn't perform well either: the efficiency is lower by 10%.

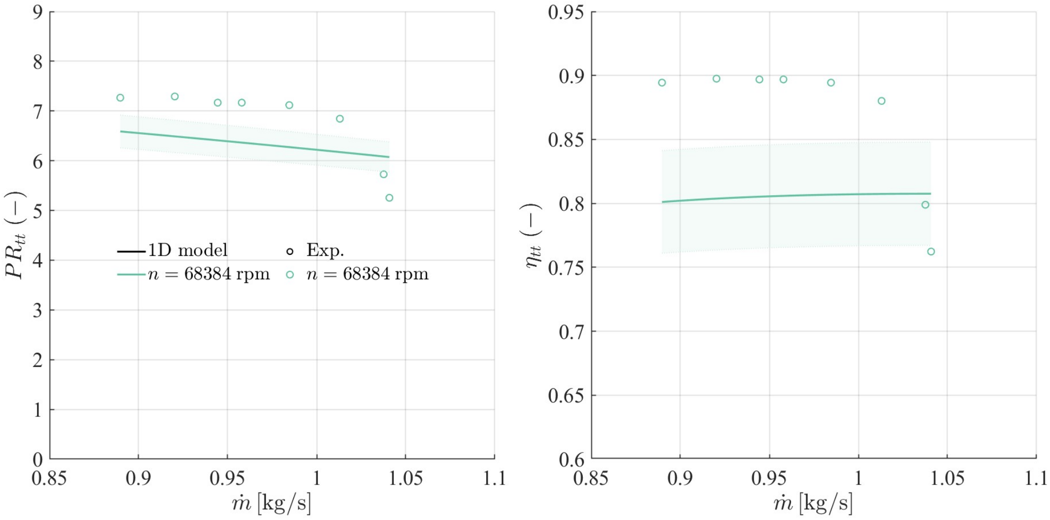

Figure 5.26: Performance estimation of H compressor (Set Oh)

5.3.4 SET 3

The last two compressors evaluated by Zhang et al. are the devices B and G, falling in group 3: B is clearly in supersonic conditions while G is very close to fall in group 1, having a relative Mach number close to 0.8.
Compressor B is evaluated both for the stage and the impeller itself. The results are here reported:

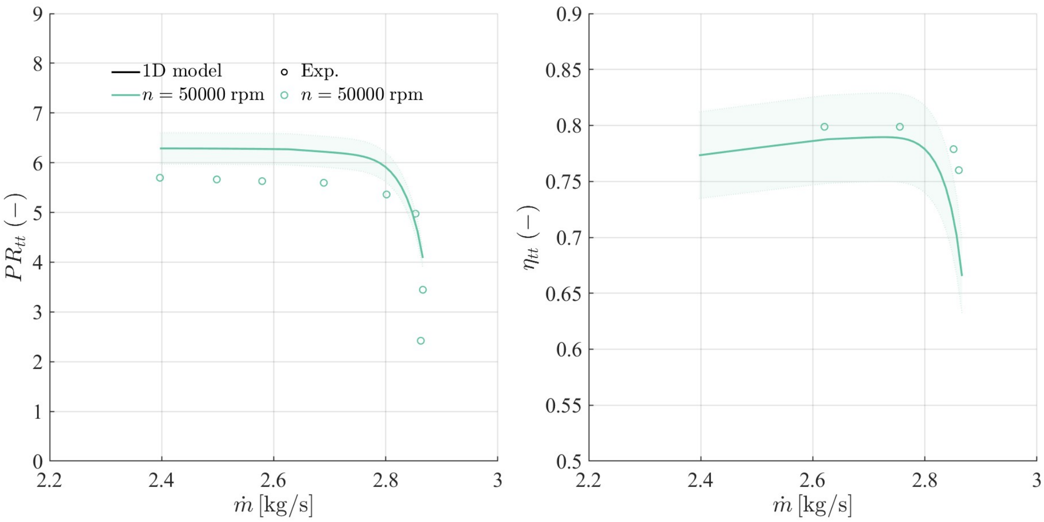

Figure 5.27: Pressure ratio and efficiency of B (Impeller)

The stage performance is:

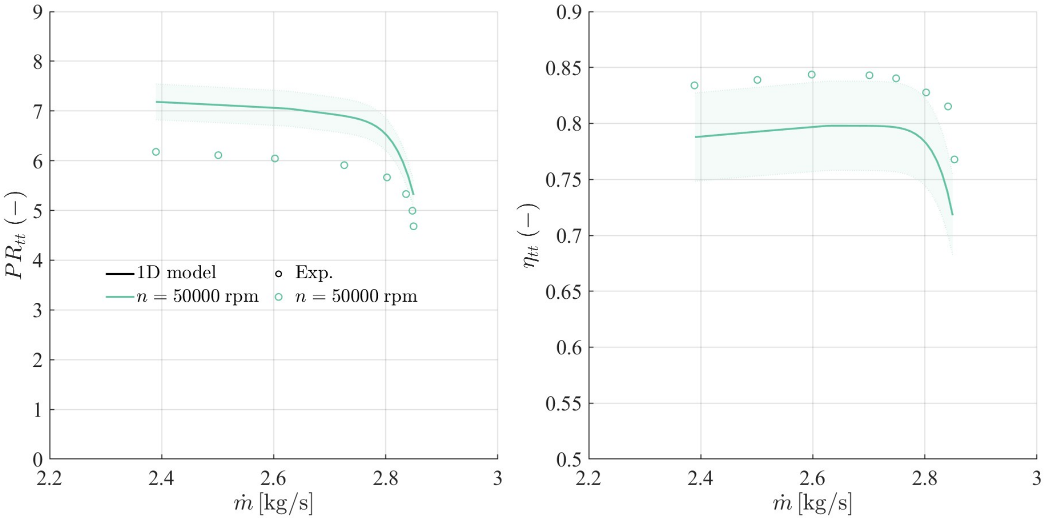

Figure 5.28: Pressure ratio and efficiency of B (Stage)

The efficiency for both stage and impeller can be improved using Aungier correlation rather than Jansen for external leakage: Jansen values are always higher than AUngier.

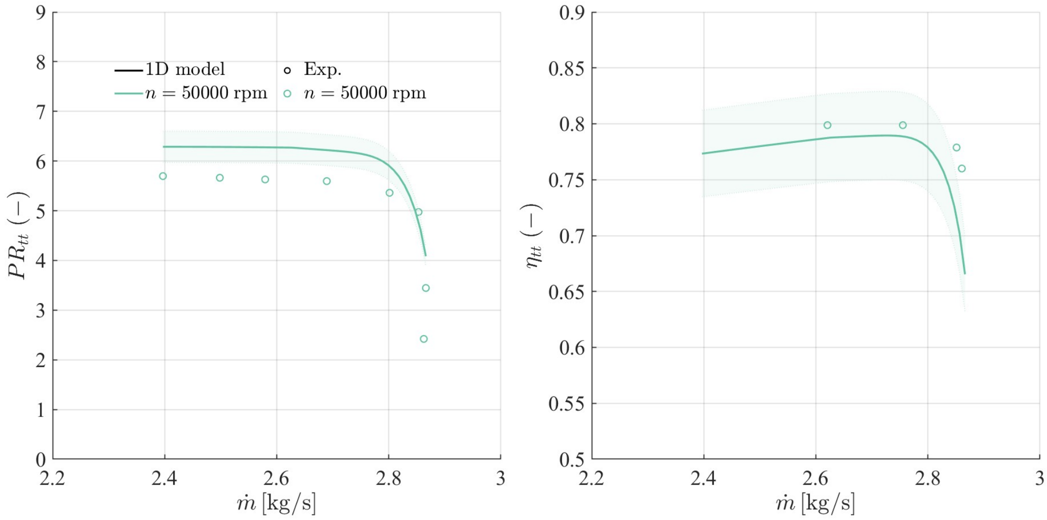

Figure 5.29: Pressure ratio and efficiency of B substituting the leakage loss by Jansen with Aungier (Impeller)

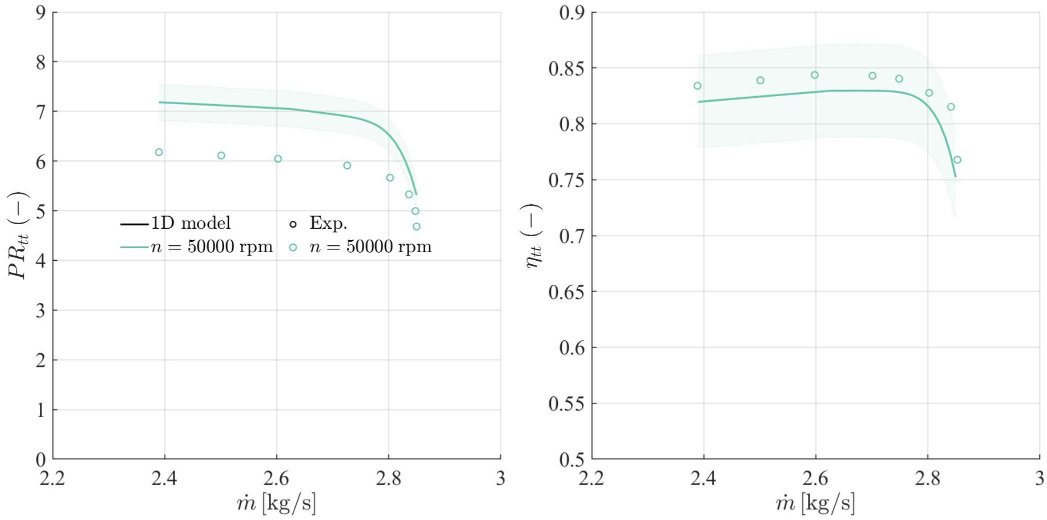

Figure 5.30: Pressure ratio and efficiency of B with Aungier as external leakage (Stage)

The last compressor evaluated is G: again, due to the close distance with respect

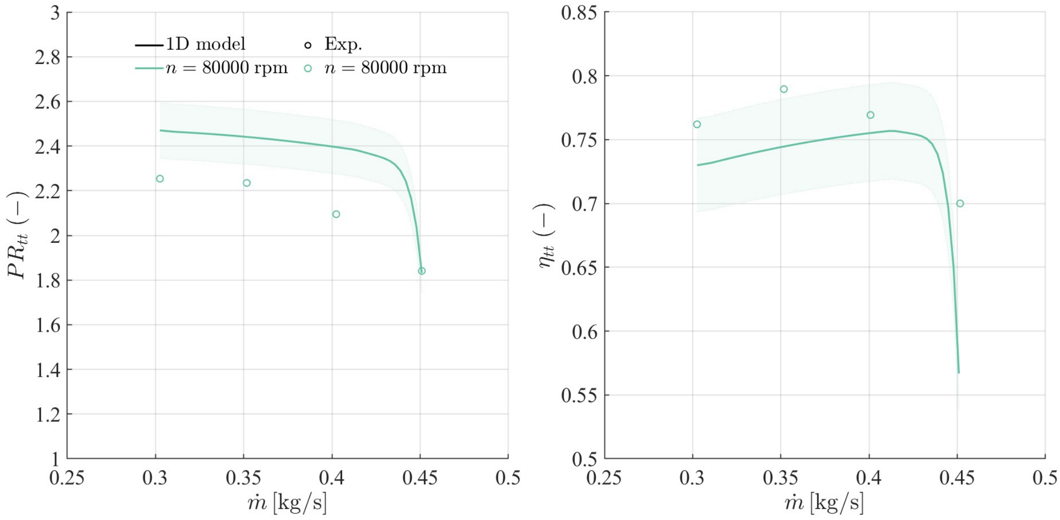

Figure 5.31: Pressure ratio and efficiency of G

The efficiency is not to far from the experimental values, but the maximum point is not reached. The pressure ratio is misestimated.
Oh set shows overall better performance estimation.

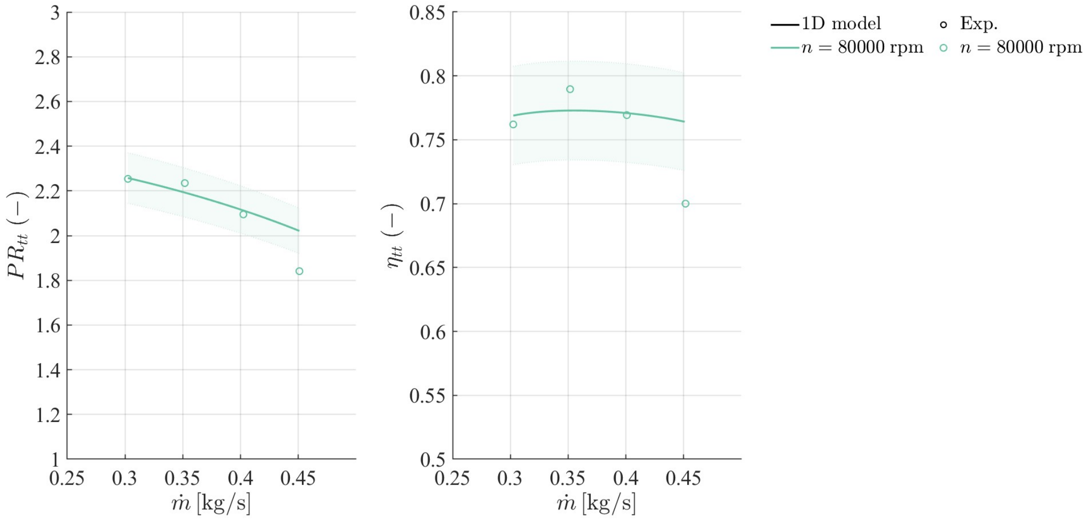

Figure 5.32: Pressure ratio and efficiency of G with Oh set

5.4 Schiffman and Favrat

The last compressor evaluated with 1-D code is a device designed for domestic heat pump applications and employed the refrigerant R134a [15]. Due to the different fluid and the restricted dimension, this compressor represent a real challenge for 1-D model and losses setup.

Parameter	**Value**	**Unit**
Thermodynamic Properties		
Fluid	R134a	–
T_{01}	265	K
p_{01}	1.65	bar
N	150–210	krpm
Geometric Dimensions		
r_{1s}	0.0056	m
r_{1h}	0.0020	m
r_2	0.007693	m
b_2	0.0012	m
$Z_{\text{r,full}}$	9	–
$Z_{\text{r,splitter}}$	0	–
LR_{splitter}	0.5	–
β_{1ts}	-56	°
β_{1bh}	-30.23	°
β_{2b}	–	°
e_a	0.15	mm
e_r	0.15	mm
e_b	0.01	m
t_{b1}	0.21	m
t_{b2}	1.00	m

Table 5.7: Thermodynamic properties and geometric dimensions of the Schiffmann & Favrat centrifugal compressor.

To evaluate the performances of this compressor, the inlet reference condition have been corrected and the fluid has been changed: the fluid can be rapidly managed in *read_check_convert* by switching off *'air'* and imposing *'R134a'*. The compressor has been evaluated with two loss models:

- Meroni, according to the paper in which the compressor has been developed;
- Set 2

The result obtain are here presented:

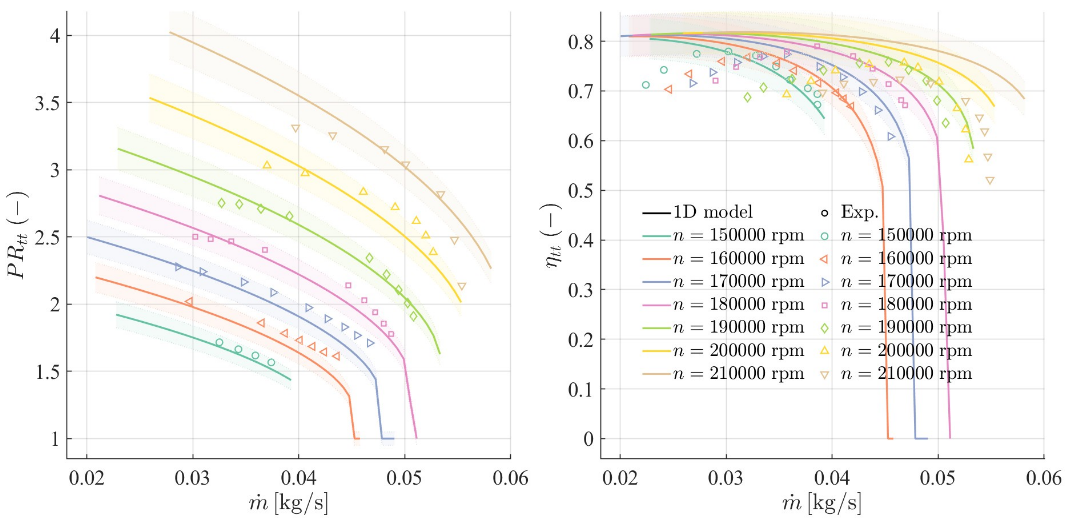

Figure 5.33: Schiffman and Favrat compressor: Meroni loss correlation

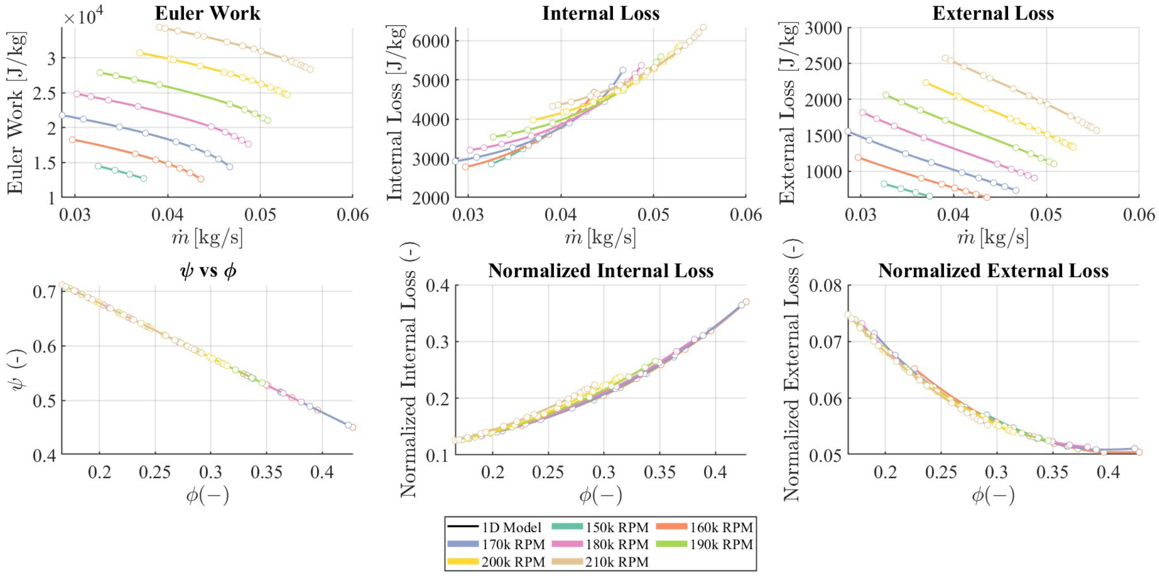

Figure 5.34: Schiffman and Favrat compressor: Meroni loss correlation

The losses have been set according to Meroni: mixing is set as external loss. The leakage loss is set to 0 since Meroni doesn't suggest any loss correlation. Meroni uses the johnston and Dean method to compute the mixing loss: since, the two-zone model has been developed (as explained before), the mixing loss follows that computational procedure. The results obtained at first attempt are quite satisfactory: more improvements can be done to better interpole the experimental values. Pressure ratio shows optimal results; the vaneless diffuser module is activated. The compressor present also an inducer and a volute, not consider in the code. Efficiencies show same shape after the peak: for lower mass flow rate, the behaviour is not as expected, but further improvemenets can be done.

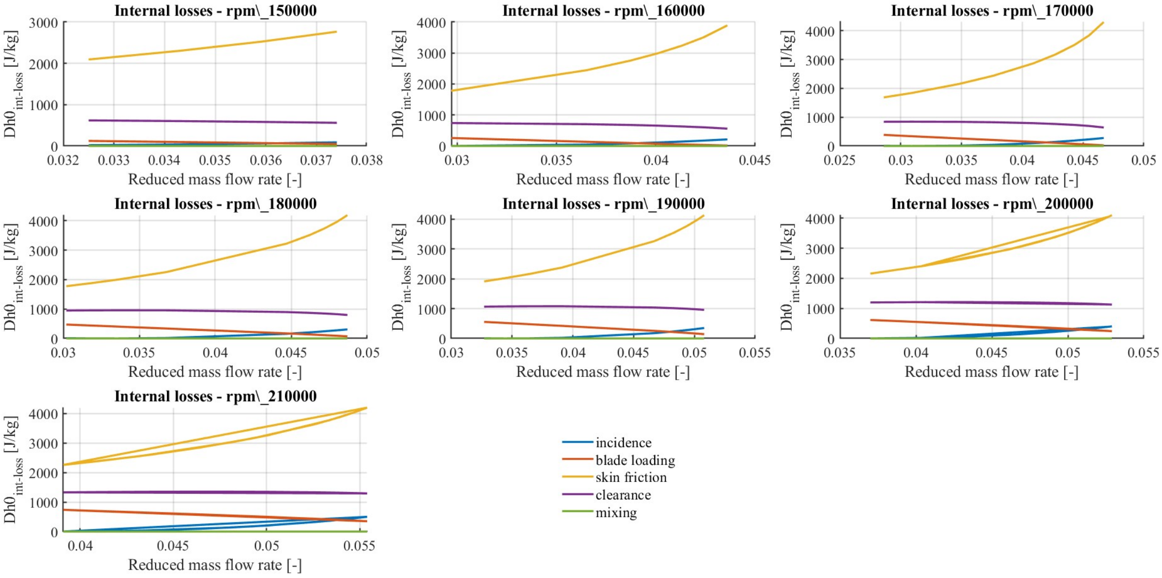

Figure 5.35: Schiffman and Favrat compressor: Internal losses evolution

The skin friction loss, as already contemplated in the Eckardt description, is the main source of entropy gain in the compressors (by following this approach).

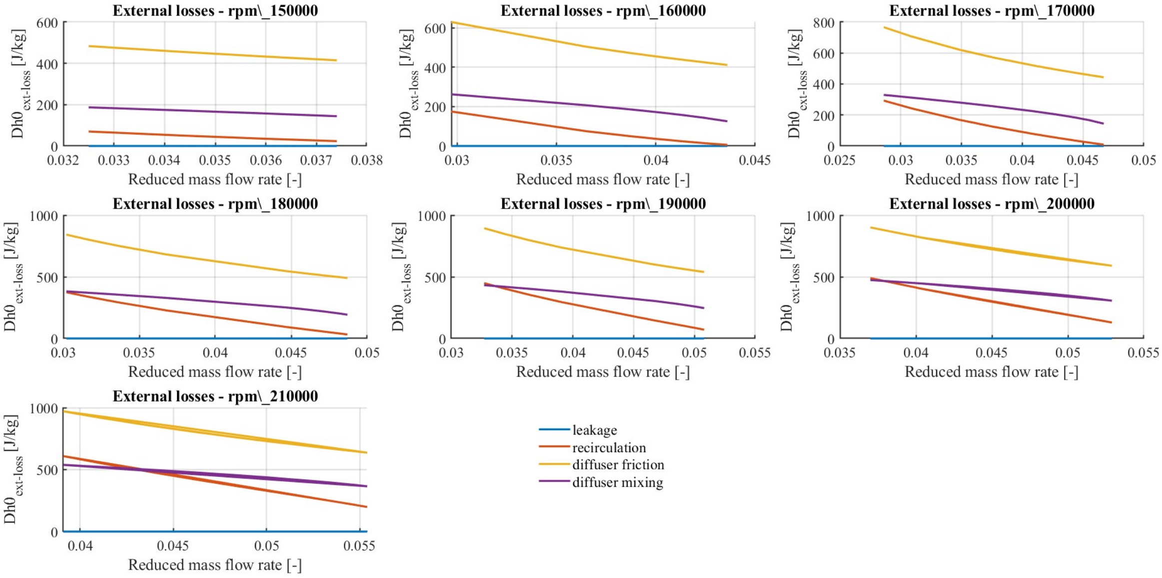

Figure 5.36: Schiffman and Favrat compressor: external losses evolution

The external losses are more balanced, compared to the internal one. The diffuser friction is the main source of loss.
The second set, SET 2 of Zhang ([19]), shows different results: the efficiencies are well above the experimental results. This behaviour has been achieve by impoaing the leakage loss equal to zero, following the concept followed by Meroni. If the leakage loss is activate, the efficiency is halve: this result describes how much leakage can affect the performances of small turbo-machines that works at huge velocities.

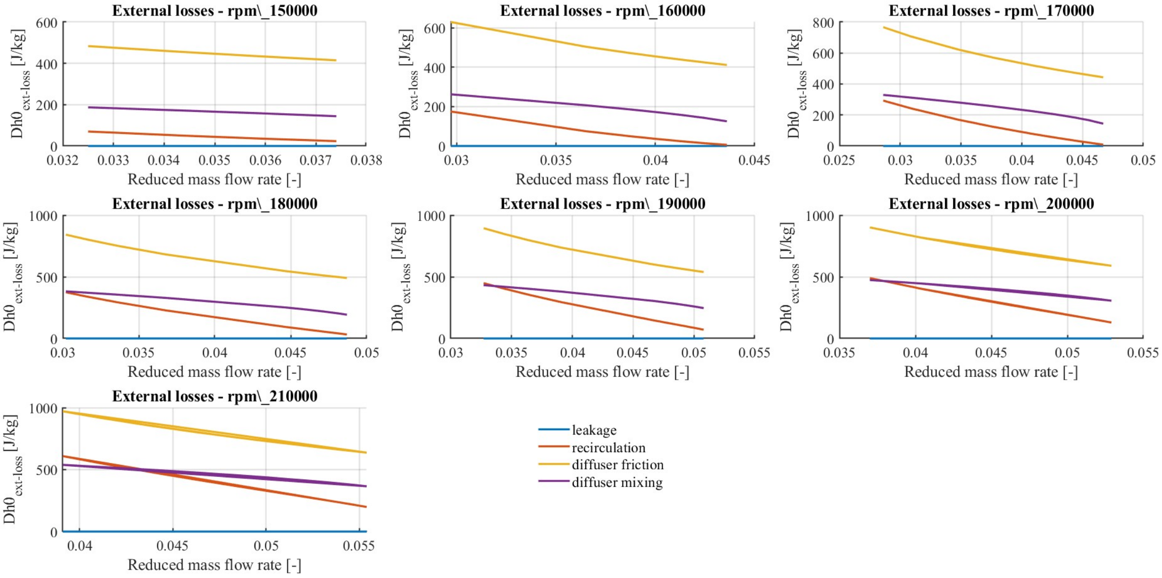

Figure 5.37: Schiffman and Favrat compressor: external losses evolution

Chapter 6

Conclusions

In this Master's thesis, a one-dimensional (1-D) computational framework for predicting the performance of centrifugal compressors has been developed, implemented, and validated. The main objective of the work was to evaluate the accuracy of several loss models available in the literature and to analyse their impact on the overall compressor behaviour. The MATLAB framework created is highly modular, allowing each physical phenomenon—incidence, friction, clearance losses, slip, mixing, and vaneless or vaned diffuser losses—to be treated as an independent component within the computational chain.

The implementation required a significant integration effort between theoretical formulations, empirical correlations, and heterogeneous geometric datasets taken from multiple sources, including Eckardt rotors, Zhang's compressors, and the R8 family of impellers. This process enabled the construction of a flexible and scalable platform, capable of handling different geometries, operating conditions, and loss correlations without interfering with the rest of the code.

The validation phase highlighted the strong influence that the choice of loss correlations exerts on performance predictions. Some models exhibited better agreement for specific geometric configurations, while others proved to be more robust across a wide range of operating conditions. The systematic comparison against experimental data made it possible to identify the strengths and limitations of each model, suggesting which correlations are more suitable for general applications and which may require further refinement.

Moreover, the modular structure of the framework proved essential for assessing the individual contribution of each loss mechanism to the overall compressor performance. This architecture also facilitates the introduction of new formulations, geometries, and advanced flow models, making the tool suitable for both academic studies and industrial applications, particularly in the context of Compressed Air Energy Storage (CAES), where accurate compressor modelling is critical for system efficiency and reliability.

In conclusion, this thesis has demonstrated that a properly structured and calibrated 1-D model can represent an effective compromise between computational cost and predictive accuracy. Despite the simplifications inherent in one-dimensional modelling, the proposed framework provides reliable insights into the behaviour of centrifugal compressors and constitutes a solid foundation for future developments, including integration with 2-D/3-D models, automated parameter calibration, extension to transient operating conditions, and application to innovative turbomachinery for energy storage technologies.

References

[1] Ayah Marwan Rabi, Jovana Radulovic, and James M. Buick. "Comprehensive Review of Compressed Air Energy Storage (CAES) Technologies". In: *Thermo* 3 (2023), pp. 104–126. DOI: `10.3390/thermo3010008`. URL: `https://doi.org/10.3390/thermo3010008`.

[2] Shabbir Ahmed, Daniel L. Flowers, and Patrick J. Balducci. *Technology Strategy Assessment: Compressed Air Energy Storage*. Tech. rep. DOE/OE-0037. Storage Innovations 2030 Strategic Initiative, Long-Duration Storage Shot. Washington, D.C.: U.S. Department of Energy, Office of Electricity, July 2023. URL: `https://www.energy.gov/oe/storage-innovations-2030`.

[3] Heidar Jafarizadeh, M. Soltani, and Jatin Nathwani. "Assessment of the Huntorf compressed air energy storage plant performance under enhanced modifications". In: *Energy Conversion and Management* 209 (2020), p. 112662. DOI: `10.1016/j.enconman.2020.112662`. URL: `https://doi.org/10.1016/j.enconman.2020.112662`.

[4] Michael Budt et al. "A review on compressed air energy storage: Basic principles, past milestones and recent developments". In: *Energy Conversion and Management* 135 (2016), pp. 318–338. DOI: `10.1016/j.enconman.2016.03.071`. URL: `https://doi.org/10.1016/j.enconman.2016.03.071`.

[5] Hao Chen et al. "Experimental and analytical investigation of near-isothermal pumped hydro-compressed air energy storage system". In: *Energy* 249 (2022), p. 123607. DOI: `10.1016/j.energy.2022.123607`. URL: `https://doi.org/10.1016/j.energy.2022.123607`.

[6] R. H. Aungier. *Centrifugal Compressors: A Strategy for Aerodynamic Design and Analysis*. New York, USA: ASME Press, 2000. ISBN: 9780791800935. DOI: `10.1115/1.801093`. URL: `https://doi.org/10.1115/1.801093`.

[7] ACE Compressor Services. *IGV Valves – Inlet Guide Vanes for Centrifugal Compressors*. Accessed: 2025-01-27. 2024. URL: `https://acecompressorservices.com/igv-valves/`.

[8] CNC Tvar. *Compressor Impellers*. Accessed: November 2025. 2025. URL: `https://www.cnctvar.cz/products/compressor_impellers/`.

[9] Boyuan Casting. *Fluid Machinery Components – Compressor Aluminum Closed Impeller.* Accessed: November 2025. 2024. URL: `https://www.boyuancasting.com/Fluid-machinery-components-compressor-aluminum-closed-impeller-for-lower-pressure-casting-pd94804136.html`.

[10] Qian Zhang et al. "Effect of Vaneless Diffuser Shape on Performance of Centrifugal Compressor". In: *Applied Sciences* 10.6 (2020), p. 1936. DOI: `10.3390/app10061936`. URL: `https://doi.org/10.3390/app10061936`.

[11] Teemu Turunen-Saaresti. "Computational and Experimental Analysis of Flow Field in the Diffusers of Centrifugal Compressor". PhD Thesis. Lappeenranta, Finland: Lappeenranta University of Technology, 2004, p. 103. ISBN: 951-764-969-X. URL: `/mnt/data/Diffusers%20geometry.pdf`.

[12] S. Larry Dixon and Cesare A. Hall. *Fluid Mechanics and Thermodynamics of Turbomachinery.* 7th. Oxford, UK: Butterworth-Heinemann, Elsevier, 2014. ISBN: 978-0-12-415954-9.

[13] M. Heinrich and R. Schwarze. "Genetic Optimization of the Volute of a Centrifugal Compressor". In: *Proceedings of the 12th European Conference on Turbomachinery Fluid Dynamics and Thermodynamics (ETC12).* Paper ID: ETC2017-072. Stockholm, Sweden: ETC, Apr. 2017.

[14] A. Laveau et al. "Design, Analysis and Fabrication of a Meso-Scale Centrifugal Compressor". In: *Proceedings of the International Mechanical Engineering Congress & Exposition (IMECE).* Orlando, Florida: ASME, Nov. 2000.

[15] Andrea Meroni et al. "Design of centrifugal compressors for heat pump systems". In: *Applied Energy* 232 (2018), pp. 139–156. DOI: `10.1016/j.apenergy.2018.09.210`. URL: `https://doi.org/10.1016/j.apenergy.2018.09.210`.

[16] Hugo Essinger and László Vimlati. "Assessment of a One-Dimensional Loss Model for the Compressor of a Turbocharger". INOM Examensarbete Teknik, Grundnivå, 15 HP. MA thesis. Stockholm, Sweden: KTH Royal Institute of Technology, June 2020. URL: `https://kth.diva-portal.org/smash/get/diva2:1453815/FULLTEXT01.pdf`.

[17] D. Japikse. "Assessment of Single- and Two-Zone Modeling of Centrifugal Compressors". In: *Proceedings of the ASME Gas Turbine Conference and Exhibit.* Studies in Component Performance: Part 3. ASME Paper 85-GT-23. Houston, Texas, USA: American Society of Mechanical Engineers (ASME), Mar. 1985, GT1985–023. DOI: `10.1115/85-GT-023`. URL: `https://asmedigitalcollection.asme.org/GT/proceedings/GT1985/79382/V001T03A023/4456650`.

[18] Barend W. Botha and Adriaan Moolman. "Determining the Impact of the Different Losses on Centrifugal Compressor Design". In: *R&D Journal* 21 (2005). Online ISSN 2309-8988; Print ISSN 0257-9669, pp. 1–15. ISSN: 2309-8988. URL: `https://journals.co.za/doi/10.10520/EJC174435`.

[19] Chaowei Zhang et al. “A method to select loss correlations for centrifugal compressor performance prediction”. In: *Aerospace Science and Technology* 93 (2019), p. 105335. DOI: `10.1016/j.ast.2019.105335`. URL: `https://doi.org/10.1016/j.ast.2019.105335`.

[20] Dario Valsesia. “Design and Off-Design Analysis of a Multistage Centrifugal Compressor for an Advanced Compressed Air Energy Storage (A-CAES) Plant”. Master’s Thesis. Milan, Italy: Politecnico di Milano, July 2020. URL: `https://hdl.handle.net/10589/163400`.

[21] M. Coppinger and E. Swain. “Performance Prediction of an Industrial Centrifugal Compressor Inlet Guide Vane System”. In: *Proceedings of the Institution of Mechanical Engineers, Part A: Journal of Mechanical Engineering Science* 213.1 (1999), pp. 65–75. DOI: `10.1243/0954406991522105`. URL: `https://doi.org/10.1243/0954406991522105`.

[22] R. H. Aungier. “Mean Streamline Aerodynamic Performance Analysis of Centrifugal Compressors”. In: *ASME Journal of Turbomachinery* 117.3 (1995), pp. 360–366. DOI: `10.1115/1.2835634`. URL: `https://doi.org/10.1115/1.2835634`.

[23] Jan Tommy Gravdahl and Olav Egeland. “Centrifugal Compressor Surge and Speed Control”. In: *IEEE Transactions on Control Systems Technology* 7.5 (1999), pp. 567–579. DOI: `10.1109/87.784420`. URL: `https://doi.org/10.1109/87.784420`.

[24] Patrik Kovář et al. “Searching for the Most Suitable Loss Model Set for Subsonic Centrifugal Compressors Using an Improved Method for Off-Design Performance Prediction”. In: *Energies* 14.24 (2021), p. 8545. DOI: `10.3390/en14248545`. URL: `https://doi.org/10.3390/en14248545`.

[25] Lorenzo Cappelletti. “One-Dimensional Modelling of a Centrifugal Compressor for a Compressed Air Energy Storage System”. Master’s Thesis. Milan, Italy: Politecnico di Milano, Dec. 2017. URL: `https://hdl.handle.net/10589/140792`.

[26] Chengshuo Wu et al. “A Review of Fluid-Induced Excitations in Centrifugal Pumps”. In: *Mathematics* 11.4 (2023), p. 1026. DOI: `10.3390/math11041026`. URL: `https://doi.org/10.3390/math11041026`.

[27] H. W. Oh, E. S. Yoon, and M. K. Chung. “Systematic two-zone modelling for performance prediction of centrifugal compressors”. In: *Proceedings of the Institution of Mechanical Engineers, Part A: Journal of Power and Energy* 216.A1 (2002), pp. 75–87. DOI: `10.1243/095765002760024854`.

[28] Nima Khoshkalam, Mohammad Mojaddam, and Keith R. Pullen. “Characterization of the Performance of a Turbocharger Centrifugal Compressor by Component Loss Contributions”. In: *Energies* 12.14 (2019), p. 2711. DOI: `10.3390/en12142711`. URL: `https://doi.org/10.3390/en12142711`.

[29] Francesco Monge. “Design of Centrifugal Compressors for Supercritical CO_2 Power Cycles”. PhD Thesis. Seville, Spain: University of Seville, 2020. URL: `/mnt/data/PhD_Monge_DesignofSCO2compressors.pdf`.